

# **Metabolism of oligodendrocytes and its involvement in axo-glia interaction**

Dissertation

for the award of the degree

“Doctor of Philosophy”

Division of Mathematics and Natural Sciences

of the Georg-August-Universität Göttingen

within the doctoral program Molecular Physiology of the Brain

of the Georg-August University School of Science (GAUSS)

submitted by

*Andrea Trevisiol*

Born in Treviso, Italy

Göttingen, December 2017

## **Thesis Committee**

Prof. Dr. Klaus-Armin Nave

Department of Neurogenetics

Max-Planck-Institute of Experimental Medicine Göttingen

Prof. Dr. Silvio Rizzoli

Department of Neuro- and Sensory Physiology

University Medical Center Göttingen

Prof. Dr. Swen Hülsmann

Experimental Neuroanesthesiology

University Medical Center Göttingen

## **Members of the Examination Board**

1. Prof. Dr. Alexander Flügel

Department of Neuroimmunology

Institute for Multiple Sclerosis Research - University Medical Center Göttingen

2. Prof. Dr. Susann Boretius

Functional Imaging Laboratory

German Primate Center

3. Dr. Katrin Willig

Optical Nanoscopy in Neuroscience

Max-Planck-Institute of Experimental Medicine Göttingen

Date of oral examination: 26.02.2018

**Declaration**

I hereby declare that the PhD thesis entitled "Metabolism of oligodendrocytes and its involvement in axo-glia interaction", was written independently and with no other sources and aids than quoted.

Göttingen, 31.12.2018

Andrea Trevisiol



## **Acknowledgments**

I would like to express my sincere and deepest gratitude to Prof. Johannes Hirrlinger and Prof. Klaus Nave for mentoring me through my Ph.D. with their incredible dedication to Science and their amazing knowledge that inspired me to pursue my studies in Neuroscience and pushed me to seek excellence.

I'm extremely grateful to Aiman Saab for guiding me at the beginning of my Ph.D, discussing projects and ideas, supporting and helping me in developing a critical and rational thinking. A special thank to Julia Edgar for being such an inspiring scientist and for teaching me during the first phase of my work at the Neurogenetics department.

I'm really grateful to all collaborators, in particular to Aiman Saab, Kathrin Kusch, Ulrike Winkler, Grit Marx and Ludovico Cantuti for their contribution to my project. Many thanks also to Prof. Frank Kirchhoff for the opportunity of taking part in the YoungGlia framework and all the Japanese scientists I had the chance to meet. In particular a big thank to Hidetoshi S. for teaching me special techniques. I'm very grateful to Prof. Felipe Barros, Prof. Fritjof Helmchen and Prof. Bruno Weber for giving me the chance to visit their labs during my Ph.D., teaching me state of the art microscopy and inspiring me through their work.

I'd like to thank Prof. Silvio Rizzoli and Prof. Swen Hülsmann for their suggestions and scientific input during the annual committee meeting, and the Göttingen Graduate School for Neurosciences, Biophysics, and Molecular Biosciences (GGNB) for their support. I further thank the members of the extended committee, Prof. Flügel, Prof. Boretius and Dr. Willig for taking the time to evaluate my work.

I'm very grateful to all people at the MPI-EM who supported my work: Tanja H., Connie C., Ursula F. and Anke S. at the animal facility; Miso M. at the LMF; Lotha D., Hajo H., Rolf M. and Harry S. for their technical assistance. Christos N. for introducing and assisting me with programming. I'm particularly grateful to Markus Krohn and his team at the feinmechanik dept. for their incredible engineering skills, the custom-tech contribution to my project and for their outstanding ability of satisfying every request.

Many thanks to Gudrun and Ulli for their technical (and moral) support throughout these years.

Thanks to all the people at the Neurogenetics department who contributed in creating the perfect atmosphere for scientific discussion and a nice working environment. Special thanks to present and former member of the department Alejandro, Clara, Constanze, Ebrahim, Georg, Hugo, Iva, Jan, Katja, Maria, Martin, Michelle, Sarah, Sharlen, Sina, Stefan, Tamer, Theresa, Tilman, Tim, Torben, Ulrike and Wilko. Thanks to all the group leaders in the lab for setting the bar for scientific excellence and being a role model for every student.

I am very thankful to Michaela and Gabriele for their help with administration stuff and for brightening up my days with jokes.

I'm very grateful to my lifetime friends Stefano, Arianna and Alberto, and to my family for keep supporting me from abroad, and super special thanks to Tiziana for her invaluable support, for teaching me illustration, proofreading this thesis and all my essays, for her determination in Science and for being such a wonderful mother. Finally, thank you Leo for making my life harder, yes, but also brighter and full of laughs.

*To my family and friends*





# Content

<b>List of figures .....</b>	<b>I</b>
<b>List of abbreviations.....</b>	<b>V</b>
<b>Abstract .....</b>	<b>XI</b>
<b>1 Introduction .....</b>	<b>1</b>
1.1 Cellular metabolism and ATP production .....	1
1.2 Metabolic support in gray matter – ANLSH .....	5
1.3 Metabolic support in white matter .....	7
1.4 Genetically encoded FRET sensors for metabolites.....	11
1.5 FLIM – FRET detection.....	14
<b>2 Objectives.....</b>	<b>17</b>
<b>3 Results.....</b>	<b>19</b>
3.1 Ateam1.03 <sup>YEMK</sup> and ThyAT transgenic mouse line.....	19
3.2 Models of energy deprivation.....	25
3.2.1 Glucose deprivation.....	26
3.2.2 Mitochondrial inhibition by azide or hypoxia .....	27
3.2.3 Simultaneous glucose depletion and mitochondrial inhibition.....	28
3.2.3.1 Comparison between energy-deprivation conditions in the optic nerve.....	29
3.3 Electrical stimulation at high frequency .....	31
3.4 CAG-GO-ATeam optic nerves: ATP and CAP responses to energy deprivation and comparison with ThyAT .....	38
3.5 Ketogenic diet impact on B-Hydroxybutyrate metabolism in the optic nerve.....	40
3.6 Lactate metabolism in white matter .....	42
3.7 ATP and CAP monitoring in <i>Slc16A1<sup>het</sup></i> optic nerves .....	44
3.8 ATP and CAP monitoring in PLP1 <sup>KO</sup> optic nerves.....	46
3.9 Spinal cord in-vivo imaging.....	53

---

<b>4</b>	<b>Discussion</b> .....	<b>55</b>
4.1	Experimental limitations .....	56
4.2	Calibration of ATeam1.03 <sup>YEMK</sup> .....	59
4.3	Axonal ATP homeostasis and nerve conduction .....	61
4.4	Myelin role in controlling ATP homeostasis: PLP mutants .....	66
4.5	Conclusions .....	69
<b>5</b>	<b>Outlook</b> .....	<b>71</b>
<b>6</b>	<b>Material and Methods</b> .....	<b>73</b>
6.1	Solutions .....	73
6.1.1	aCSF .....	73
6.1.2	AP buffer .....	74
6.1.3	AT imaging medium .....	74
6.2	Transgenic mice .....	75
6.2.1	Determination of copy number .....	76
6.2.2	Analysis of the sensor expression pattern .....	76
6.2.3	Preparation of mouse genomic DNA .....	77
6.2.4	Genomic DNA analysis by PCR DNA-amplification .....	78
6.2.5	Primers .....	79
6.2.6	PCR programs for genotyping .....	80
6.3	Ketogenic diet .....	80
6.4	Blood measurement of glucose and $\beta$ -hydroxybutyrate .....	81
6.5	Mixed myelinating co-cultures .....	81
6.6	HeLa cell line culture .....	82
6.7	Optic nerve preparation and electrophysiological recordings .....	82
6.8	Optic nerve imaging .....	83
6.9	aCSF based solutions for optic nerve CAP/ ATP recording .....	84
6.10	Coverslip preparation .....	85

---

6.11	Solutions for ThyAT neuronal ATP imaging .....	85
6.12	Solutions for FLIM calibration .....	86
6.13	FLIM imaging .....	86
6.14	In vivo imaging.....	87
6.14.1	Anesthesia and pain management during the postoperative phase.....	87
6.14.2	Surgery.....	90
6.14.3	Imaging.....	90
6.15	Data analysis .....	91
6.15.1	CAP .....	91
6.15.2	ATP .....	92
6.15.3	ATP & CAP parameters .....	92
6.15.4	FLIM .....	93
6.16	Western blot and quantification .....	93
6.16.1	Immunoblotting .....	94
6.17	Electron microscopy.....	95
6.18	Presentation of data.....	95
6.19	Analysis scripts .....	96
<b>7</b>	<b>Reference list.....</b>	<b>97</b>
	<b>Appendices .....</b>	<b>111</b>
7.1	Appendix §1 – MATLAB script for CAP processing and analysis.....	111
7.2	Appendix §2 – ImageJ Macro for FRET ATP analysis on ROI basis.....	113
7.3	Appendix §3 – ImageJ macro for initial processing of FLIM data.....	117
7.4	Appendix §4 – MATLAB script for FLIM analysis on ROI basis .....	118
	<b>Curriculum Vitae .....</b>	<b>125</b>



## List of figures

<b>Figure 1.</b>	Main metabolic pathways in a living cell.....	4
<b>Figure 2.</b>	Proposed axo-glia metabolic coupling in white matter.....	10
<b>Figure 3.</b>	A <sub>Team1.03</sub> <sup>YEMK</sup> is a genetically encoded FRET sensor for ATP .....	19
<b>Figure 4.</b>	Characterization of the expression pattern of the newly generated B6-Tg(Thy1.2-A <sub>Team1.03</sub> <sup>YEMK</sup> )A <sub>Jhi</sub> (ThyAT)-mouse line.....	20
<b>Figure 5.</b>	The ATP sensor A <sub>team1.03</sub> <sup>YEMK</sup> in cultured neurons detects ATP fluctuations during different treatments.....	22
<b>Figure 6.</b>	Imaging of ATP combined with electrophysiology in acutely isolated optic nerves of ThyAT-mice.....	23
<b>Figure 7.</b>	ATP and CAP Area recordings during simultaneous mitochondrial blockade and glucose deprivation. ....	24
<b>Figure 8.</b>	Impairment of axonal ATP and CAP by glucose removal from the aCSF (glucose deprivation, GD, 45 min).....	26
<b>Figure 9.</b>	Effects of mitochondrial blockade by azide (MB) and hypoxia (N <sub>2</sub> ) on axonal ATP and nerve CAP.....	27
<b>Figure 10.</b>	Impairment of axonal ATP and CAP during glucose deprivation and simultaneous inhibition of mitochondrial activity by azide (MB + GD) or hypoxia (OGD). ....	28
<b>Figure 11.</b>	Quantification and comparison of CAP and ATP signals during all energy-failure paradigms. ....	31
<b>Figure 12.</b>	Comparison of axonal ATP and nerve CAP dynamics during high frequency stimulation. ....	32
<b>Figure 13.</b>	Example of progression of CAP waveform changes during high frequency stimulation (HFS). ....	33
<b>Figure 14.</b>	Quantification and correlation of CAP and ATP signals of optic nerve's axons stimulated at 16, 50 and 100 Hz (HFS) while supplied with different glucose concentrations (2, 3.3 and 10 mM). ....	34

<b>Figure 15.</b> Example of CAP waveforms' and ATP sensor fluorescence intensities' changes during high frequency stimulation (HFS) of optic nerves incubated with aCSF containing different glucose concentrations. ....	35
<b>Figure 16.</b> Correlation of the rates and amplitudes of CAP and ATP changes during HFS in different glucose concentrations. ....	36
<b>Figure 17.</b> Comparison between glucose, lactate and pyruvate as exogenous energy substrates shows energy metabolism of axons is better maintained in the presence of glucose at higher frequencies. ....	37
<b>Figure 18.</b> CAG-GO-ATeam responses to energy deprivation paradigms .....	39
<b>Figure 19.</b> Ketone bodies as energy substrate in optic nerves. ....	41
<b>Figure 20.</b> Quantification of CAP and ATP signals during the different phases of $\beta$ -hydroxybutyrate exposure in KD treated mice. ....	42
<b>Figure 21.</b> Endogenous production of lactate from glucose the optic nerve is essential to maintain ATP during HFS. ....	43
<b>Figure 22.</b> Example of CAP traces before and after high frequency stimulation (HFS) of optic nerves in the presence of inhibitors of lactate metabolism. ....	44
<b>Figure 23.</b> Analysis of ATP and CAP during HFS in optic nerves from MCT1 <sup>+/-</sup> mice. ....	45
<b>Figure 24.</b> Analysis of ATP and CAP during HFS in optic nerves from 10 weeks old MCT1 <sup>+/-</sup> mice. ....	46
<b>Figure 25.</b> Optic nerves prepared from PLP <sup>KO</sup> mice, model of spastic paraplegia type-2, show axonal impairment at 10 weeks of age. ....	47
<b>Figure 26.</b> ATP and CAP responses in PLP <sup>KO</sup> optic nerves subjected to high frequency stimulation (HFS) with glucose or lactate as main substrate. ....	48
<b>Figure 27.</b> Quantification of ATP and CAP signals in PLP <sup>KO</sup> optic nerves subjected to increasing frequency stimulation (RAMP, 1-100 Hz). ....	49
<b>Figure 28.</b> Quantification of ATP and CAP signals in PLP <sup>KO</sup> optic nerves subjected to glucose deprivation (GD). ....	50
<b>Figure 29.</b> Further analysis of ATP in PLP <sup>KO</sup> optic nerves subjected to RAMP/GD, using a FIJI-macro to separate ATeam1.03 <sup>YEMK</sup> fluorescence in large and small fibers. ....	52

---

<b>Figure 30.</b> Laminectomy and chronic window implant in the spinal cord of a transgenic mouse. ....	53
<b>Figure 31.</b> In vivo imaging of ThyAT spinal cord axons of the fasciculus gracilis (T12) using a chronic window.....	54
<b>Figure 32.</b> Concept of ATP steady state .....	57
<b>Figure 33.</b> FLIM –TCSPC analysis of ATeam1.03 <sup>YEMK</sup> in cultured cells and calibration. ....	60
<b>Figure 34.</b> Custom perfusion chamber for cell imaging. ....	86





## List of abbreviations

ACAT	Acyl-CoA:cholesterol acyltransferase
aCSF	Artificial cerebro-spinal fluid
ADP	Adenosine diphosphate
AF	Atipamezole – Flumazenil
ALS	Amyotrophic lateral sclerosis
AMP	Adenosine monophosphate
ANLSH	Astrocyte-neuron lactate shuttle hypothesis
AP	Action potential
API	Active pharmaceutical ingredient
ATP	Adenosine triphosphate
AUW	Area under the waveform
bp	Base pairs
BP	Band-pass
BTS	Brain/Tissue Slice
BW	Body weight
°C	Degrees Celsius (centigrades)
CAP	Compound action potential
CFP	Cyan fluorescent protein
CNS	Central nervous system
cp	Circularly permuted
cpFP	Circularly permuted fluorescent protein
ddH <sub>2</sub> O	Double distilled (or miliQ) water
DG	Deoxyglucose
DIC	Differential interference contrast
DIV	Days in vitro
DMEM	Dulbecco's Modified Eagle's medium
DMSO	Dimethylsulfoxide
DNA	Deoxyribonucleic acid
dNTP	Deoxynucleotide triphosphate
e.g.	<i>Exempli gratia</i>
EDTA	Ethylenediaminetetraacetic acid
EGFP	Enhanced green fluorescent protein
Et al.	<i>Et alia</i>
ETC	Electron transport chain
F/C	FRET/CFP (channels)
F/G	FRET/GFP (channels)

## Abbreviations

---

FLIM	Fluorescence-lifetime imaging microscopy
FP	Fluorescent protein
FRET	Förster Resonance Energy Transfer
FWD	Free working distance
G	Gravitational constant
GaAsP	Gallium arsenide phosphide
GD	Glucose deprivation
GFP	Green fluorescent protein
GLUT1	Glucose transporter-1
GM	Gray matter
GTP	Guanosine Triphosphate
h	Hour
HFS	High frequency stimulation
HSP	Hereditary spastic paraplegia
Hz	Herz
i.e.	<i>Id est</i>
IP	Intraperitoneal
IP	Intraperitoneal
IRF	Instrument response function
kcal	Kilocalorie
KD	Ketogenic diet
L	Liter
LDH	Lactate dehydrogenase
LSM	Light scanning microscopy
LT	Lifetime
M	Molar
m	Meter
mA	Milliampere
MB	Mitochondrial blockade
MCT	Monocarboxylate transporter
mEGFP	Monomeric enhanced green fluorescent protein
MEM	Minimum Essential Medium
MHz	Megahertz
min	Minute
mKO $\kappa$	Monomeric Kusabira orange- $\kappa$
ml	Milliliter
mM	Millimolar
mm	Millimeter

---

MMF	Midazolam – Medetomidine – Fentanyl
MMF	Medetomidine Midazolam Fentanyl
ms	Milliseconds
mseCFP	Monomeric super enhanced cyan-fluorescent protein
mVenus	Monomeric venus (flurescent protein)
MW	Molecular weight
NADH	Nicotinamide adenine dinucleotide
ND	Normal diet
nM	Nanomolar
nm	Nanometer
NMDA	N-Methyl-D-aspartic acid
NMDAR	N-methyl-D-aspartate receptor
ns	Nanosecond
NT	Neurotransmitter
∅	Diameter
OFP	Orange fluorescent protein
OGD	Oxygen-glucose deprivation
OX-PHOS	Oxidative phosphorylation
p	P-value
PCR	Polymerase chain reaction
PFA	Paraformaldehyde
pg	Picogram
PLP	Proteolipid protein
pM	Picomolar
PMT	Photon multiplier tube
ps	Picosecond
qPCR	Quantitative polymerase chain reaction
RGC	Retinal ganglion cells
ROI	Region of interest
rpm	Revolutions per minute
s	Second
SC	Spinal cord
SCOT	Succinyl-CoA-3-oxaloacid CoA transferase
SEM	Standard error of the mean
SHG	Second-harmonic generation
SPG2	Spastic gait gene 2
TCA	tricarboxylic acid (or citric acid) cycle
TCSPC	Time-correlated single photon counting

## Abbreviations

---

U	Unit (for enzyme activities)
v/v	Volume per volume percentage concentration
w/v	Weight per volume percentage concentration
WM	White matter
wt	Wildtype
YFP	Yellow fluorescent protein
$\beta$ -HB	$\beta$ -Hydroxybutyrate
$\lambda$	Lambda, wavelength
$\mu$ g	Microgram
$\mu$ l	Microliter
$\mu$ M	Micromolar
$\mu$ m	Micrometer
$\mu$ mol	Micromolar
Ms	Microsecond
$\mu$ V	Microvolt
$\tau$	Tau, exponential time constant for lifetime

International System of Units (SI) was used throughout this thesis



## **Abstract**

In white matter, axonal energy homeostasis critically depends on glial support. Failure in glial-mediated delivery of metabolic substrates into the axonal compartment results in axonal energy deficit and may anticipate axonal degeneration observed in myelin disorders and several neurodegenerative diseases. In mice, transgenic expression of an ATP-sensor in neurons allowed us to visualize axonal energy content in acutely isolated optic nerves while simultaneously performing electrophysiological compound action potentials (CAP) recordings. The real-time monitoring of activity-dependent axonal ATP revealed a strong correlation between axonal energy fluctuations and nerve conduction. Importantly, upon pharmacological inhibition of endogenous lactate metabolism while under continuous glucose supply, ATP-CAP correlation was disrupted, suggesting that the axonal glycolysis products alone were insufficient to maintain axonal mitochondrial energy metabolism during spiking activity. To determine possible metabolic consequences of myelin defects we monitored ATP and CAP in *Pmp1*-null optic nerves. Genetic ablation of *Pmp1*, encoding a myelin membrane protein, serves as a model of spastic paraplegia type-2, where functional but structurally destabilized myelin sheaths lead to secondary axonal loss. We found that the energy metabolism of myelinated axons of *Pmp1*-null optic nerves is perturbed long before the onset of clinical symptoms and major pathological changes. These observations motivated us to assess the metabolic properties of spinal cord fibres in vivo to allow long-term studies involving demyelination and remyelination models. The parallel monitoring of axonal ATP and CAP is a powerful tool to study white matter metabolism and metabolic support mechanisms under physiological conditions and in models of neurodegenerative disorders.

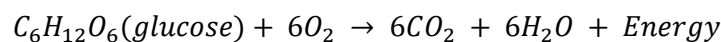




# 1 Introduction

## 1.1 Cellular metabolism and ATP production

Metabolism is the series of biochemical reactions used by living beings for maintaining their structure and molecular organization in a quasi-stable state which is maintained by a steady state flux through metabolic pathways. Metabolism can theoretically be divided into two processes: anabolism and catabolism. Anabolism is the process of arranging smaller molecules into macromolecules essential to maintain cellular activity, by consuming or, less often, storing energy. Catabolism is the process that disintegrates organic molecules and macromolecules such as proteins, lipids and carbohydrates to release energy in its biochemical form, ATP. The main catabolic process happening in the brain is the oxidation of glucose, one of the simplest carbohydrate, into six molecules of CO<sub>2</sub>. The conversion of glucose into energy can be summarized as:



The energy released by catabolic reactions can be stored in phosphoric acid anhydride bonds using adenosine nucleotide molecules as substrates, thus generating ADP and ATP. The opposite process, the hydrolysis of phosphoric acid anhydride bonds from ATP, yields ADP and phosphates, or AMP and pyrophosphate, as a result of an exergonic reaction releasing 7.3 kcal/mol or 10.9 kcal/mol, respectively (Stryer, 1995). For its role in energy exchange between metabolic pathways, ATP is often referred to as the cell energy currency. ATP is generated by brain cells from glucose mainly via two metabolic pathways: glycolysis in the cytosol and the oxidative phosphorylation (OX-PHOS) in the mitochondrion, the latter mostly in combination with the production of NADH from the citric acid cycle (TCA).

In order to generate ATP in the brain, glucose is initially uptaken by glial cells from the blood stream through the blood-brain barrier using GLUT-1 (McAllister et al., 2001). Within glial cells glucose is partially phosphorylated to glucose-6-phosphate by hexokinase, using one molecule of ATP. This is the first of the 10 reactions of glycolysis and during this preparatory phase, an additional ATP is consumed by phosphofructokinase to phosphorylate fructose 6-phosphate to fructose 1,6-phosphate. The subsequent phase of glycolysis is the payoff phase that starts with the production of NADH by glyceraldehyde 3-phosphate dehydrogenase (GAPDH) and yields a total of four ATP, two NADH and two pyruvate molecules.

The fate of pyruvate is essential to understand whether a cell can metabolically support neighboring cells or whether its metabolism doesn't allow for that. Pyruvate can be either reduced to lactate and released, or further oxidized in the mitochondrial TCA (Figure 1). Both lactate and pyruvate, can be endogenously produced or obtained exogenously from the extracellular space, and both can feed mitochondrial TCA/oxidative-phosphorylation, bypassing glycolysis. Consequently, pyruvate and lactate are intermediate metabolites, linking anaerobic and aerobic ATP production either within single cells or between cells, as a consequence of metabolic support. Lactate released by a glycolytic cell can be caught by a neighboring cell and converted into pyruvate, which can then be co-transported with a proton into the mitochondrial matrix and generate ATP.

In the mitochondrial matrix, pyruvate undergoes decarboxylation to acetyl-CoA, along with reduction of  $\text{NAD}^+$  to NADH, by action of pyruvate dehydrogenase which uses coenzyme-A (CoA) as cofactor. Acetyl-CoA can also be provided by other metabolic pathways involving e.g., the catabolism of fatty acids ( $\beta$ -oxidation). Acetyl-CoA can enter the TCA cycle and be converted to citrate, a six-carbon molecule, by citrate synthase which uses the four-carbon molecule oxaloacetate as substrate for the reaction. As a net gain for the cell, TCA cycle produces three molecules of NADH, one ATP and one  $\text{QH}_2$  (or one  $\text{FADH}_2$ ) along with two molecules of  $\text{CO}_2$  (waste) and regenerates oxaloacetate for the next cycle. All NADH molecules produced, either by glycolysis (which enter the mitochondrial matrix through the malate-aspartate shuttle) or by TCA, are used in the electron transport chain (ETC) as electron-donors. The process of oxidation of NADH to  $\text{NAD}^+$  and  $\text{H}^+$  is coupled, by mitochondrial complexes I-IV, to the transfer of protons across the inner mitochondrial membrane. The establishment of an electrochemical proton gradient drives the production of ATP, starting from ADP and inorganic phosphate, by the ATP synthase (Cooper & Hausman, 2007).

Although total concentration of ATP has been estimated in brain tissue (i.e.  $2.3 \mu\text{mol/g}$  of frozen murine brain tissue; Beis & Newsholme 1975), little is known about its steady state and its kinetics in single brain cell types under physiological conditions. It is predicted that for each molecule of glucose which gets fully oxidized in the cell, 29-30 molecules of ATP are produced by the combined activity of glycolysis and mitochondria respiration (Rich, 2003). In the brain, the maintenance of proper ATP homeostasis seems to be essential for neurons. Alterations in ATP management have been described in a mouse model for Rett syndrome, suggesting a link between impaired ATP homeostasis and increased susceptibility to epileptic seizures (Toloe, Mollajew, Kügler,

& Mironov, 2014). The process of glucose oxidation is not always complete, yielding around 30 ATP molecules: pyruvate can in fact be transformed by lactate dehydrogenase (LDH) into lactate. Despite its inefficiency in ATP generation, this process of lactate formation can be used to quickly regenerate  $\text{NAD}^+$  (Keith Chenault & Whitesides, 1989) and to maintain high rates of anaerobic consumption of glucose via glycolysis, process relevant in cancer and known as Warburg effect (Liberti & Locasale, 2016; Warburg, 1925).

Lactate can consecutively be released and used to fuel ATP production by nearby cells: the process can be seen as metabolic support and is facilitated by transporters termed monocarboxylate transporters (MCTs). Four different types of MCTs, encoded by the *SLC16A* family of genes, are responsible for the proton-coupled transport of several monocarboxylates such as pyruvate, lactate or ketone bodies (acetoacetate and  $\beta$ -hydroxybutyrate): MCT1, MCT2, MCT3 and MCT4 (Morris & Felmler, 2008). Different cell types express different MCTs: neurons express mainly MCT2 while glial cells, astrocytes and oligodendrocytes, express mainly MCT1-4 (Pérez-Escuredo et al., 2016; Pierre & Pellerin, 2005). The transporters differ mainly for their affinities to the substrates, having different  $K_m$  values. For lactate MCT1 has a calculated  $K_m$  of 3.5 – 10 mM, while MCT2  $K_m$  is between 0.5 – 0.75 mM (Halestrap, 2012). This implies that, assuming a null cytosolic concentration for lactate, a cell that expresses MCT1 will uptake lactate in an extracellular sub-millimolar concentration very slowly, while a cell that expresses MCT2 will be more reactive in its uptake. Along with the knowledge of different glycolytic states, the expression of different MCTs poses the basis for the concept of metabolic support that uses lactate as a supporting metabolite both in gray and white matter (J. Hirrlinger & Nave, 2014; Pérez-Escuredo et al., 2016).

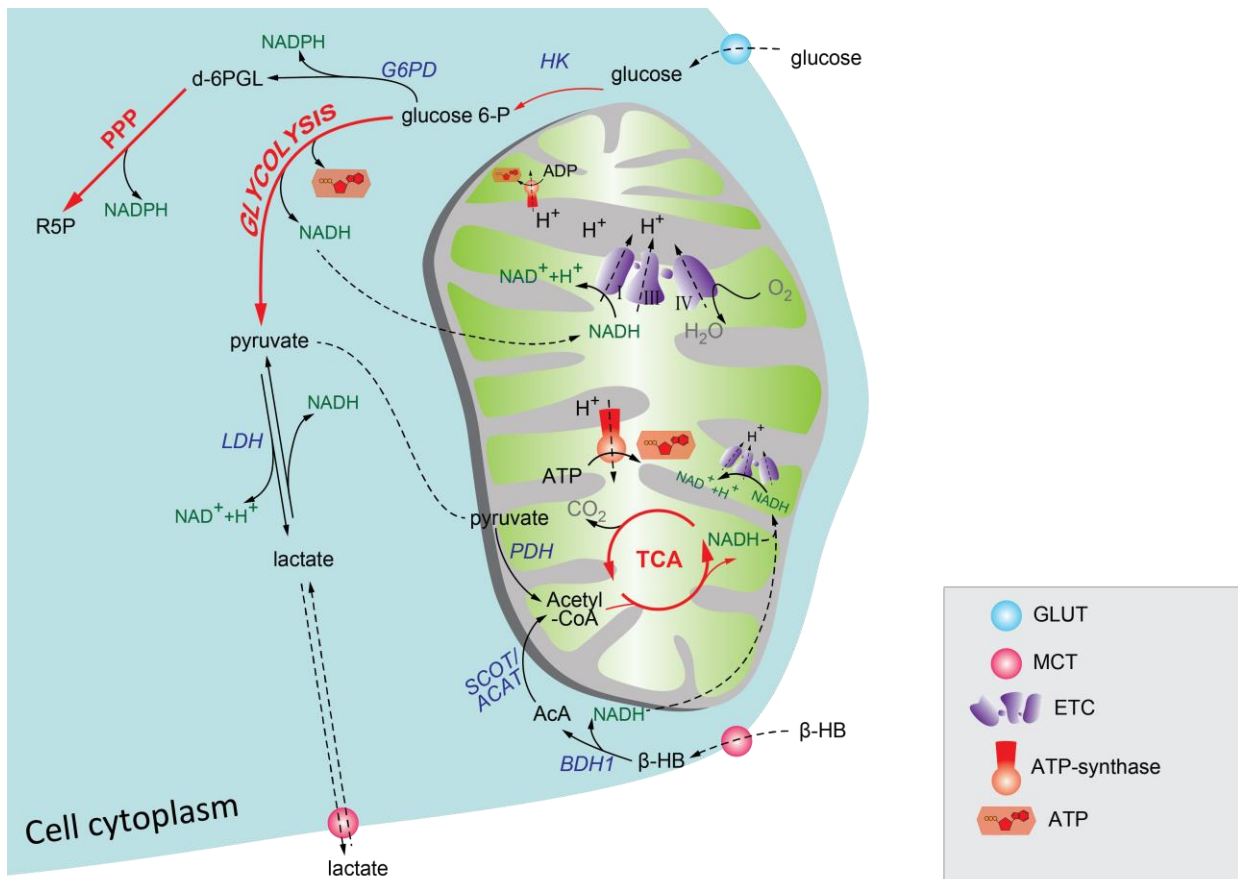


**Figure 1. Main metabolic pathways in a living cell.**

Metabolic pathways contribute to generate ATP and maintain the structural and molecular organization of the cell (entire pathways are highlighted in red). Transporters allow substrates for the metabolic pathways to enter, and be released by, the cell. Glycolytic enzymes provide anaerobic production of ATP and are located in the cytoplasm. The glycolytic process is coupled to mitochondrial tricarboxylic acid cycle (TCA) and oxidative phosphorylation (OX-PHOS) mainly by pyruvate and the reducing equivalent NADH. Mitochondrial activity requires oxygen as electron acceptor in the electron transport chain (ETC) and relies on the electrochemical gradient of protons (H<sup>+</sup>) to generate ATP through the ATP synthase. Estimates calculate a production of 29 to 30 molecules of ATP per each molecule of glucose fully oxidized.

Key enzyme are indicated in blue italics, HK: hexokinase; G6PD: glucose 6-phosphate dehydrogenase; LDH: lactate dehydrogenase; PDH: pyruvate dehydrogenase; SCOT: succinyl-CoA-3-oxaloacid CoA transferase; ACAT: Acyl-CoA cholesterol acyl transferase; BDH: beta hydroxybutyrate dehydrogenase. Entire metabolic pathways are indicated in red, PPP: pentose phosphate pathway; TCA: tricarboxylic acid cycle; ETC: electron transport chain. Reducing equivalent are labeled in green: NAD(P): Nicotinamide adenine dinucleotide (phosphate). Substrates: ATP: adenosine triphosphate; β-HB: beta hydroxybutyrate; AcA: Acetoacetate; d-6GPL: 6-phosphoglucono-delta-lactone; R5P: Ribulose 5-phosphate. Transporters: GLUT: glucose transporter; MCT: monocarboxylate transporter.

## 1.2 Metabolic support in gray matter – ANLSH

The great metabolic demand of neurons is matched by a precise local regulation of blood flow and pressure (Magistretti, 2006). In the late 70s, it was possible to identify a coupling between neuronal activity and glucose consumption using 18-fluoro-DG imaging of glucose consumption by positron emission tomography (PET) (Sokoloff et al., 1977). Providing that neurons are never in contact with the vasculature, and a selective barrier is controlling the delivery of glucose and other metabolites, it is evident that glial cells are working as mediators for metabolism. More recently it has been shown that astrocytes can control the blood supply, possibly as the initial step for the metabolic support of neurons (Mulligan & MacVicar, 2004). In order to maximize this support, astrocytes are capable of perceiving and responding to synaptic activity by shuttling the metabolites uptaken from the blood stream. The detailed mechanisms through which astrocytes support neurons have been described by Pellerin & Magistretti in 1994 in a model that defines this neurometabolic coupling as the astrocyte-neuron lactate shuttle hypothesis (ANLSH).

Starting from the classic 'bipartite' communication between the pre- and postsynaptic neurons, the intimate association of astrocytes with synapses has introduced the concept of the 'tripartite synapse', i.e. the functional integration of pre and post synapse with the neighboring astrocyte. According to the ANLSH astrocytes are capable of sensing the neuronal activity and, by increasing their own anaerobic metabolism, release lactate to support the perceived higher demand for substrates. This neurometabolic coupling mediated by astrocytes starts with the release of glutamate neurotransmitters from the pre-synapse, following with the arrival of an action potential. The astrocytes processes that are surrounding the synapse remove the glutamate by taking it up via sodium co-transport. The cytosolic increase in sodium concentration activates the Na/K ATPase which pumps out three Na<sup>+</sup> by hydrolyzing one molecule of ATP. The sudden increase in ATP consumption triggers the astrocytes to enhance the local uptake of glucose from the vascular lumen. The fate of glucose taken up in a glutamate-dependent way, is mainly lactate production, indicating an activation of aerobic glycolysis in astrocytes (Pellerin & Magistretti, 1994). A modulator-signal from astrocytes seems to be responsible for the metabolic adaptation of neurons: ascorbic acid. Ascorbic acid is the reduced form of vitamin-C and it is highly concentrated in the human brain (14 mg/100 g of wet tissue; Hornig, 1975). Besides its well-known function as antioxidant, ascorbic acid has been reported to regulate metabolism in cultured neurons (Beltrán et al., 2011; Castro et al.,

2007; Castro, Beltrán, Brauchi, & Concha, 2009). After its release by astrocytes, triggered by glutamate stimulation, ascorbic acid is taken up by the neurons in a sodium dependent co-transport. The rise in intracellular sodium in neurons stimulates lactate and inhibits glucose uptake (Castro et al., 2007, 2009). Gray matter astrocytes are thus fulfilling several tasks with the common aim of keeping neuronal transmission efficient at the synaptic level: I) cleaving neurotransmitters from the synaptic cleft (Stobart & Anderson, 2013; Swanson, 2004; Y. Zhang & Barres, 2010), II) control local blood supply (Mulligan & MacVicar, 2004) and lactate delivery (Magistretti, 2006; L Pellerin & Magistretti, 1994) and III) signaling neighboring neurons to metabolically switch towards more aerobic ATP production derived from mitochondrial oxidation of lactate (Castro et al., 2007, 2009).

The ANLSH implies that neurons, especially under conditions of synaptic activation, are producing ATP mainly by oxidative phosphorylation, while astrocytes are mainly glycolytic and provide lactate as energy substrate to neurons (Magistretti, 2006; L Pellerin & Magistretti, 1994; Luc Pellerin, 2003). Although this hypothesis originally based on in vitro studies fits many in vivo observations using PET, fMRI, and MRS (Figley & Stroman, 2011; Lin, Gao, Duong, & Fox, 2010) it still remains a matter of debate. For example, evidence suggests that cultured glutamatergic cerebellar neurons seem to preferentially use glucose and not lactate during synaptic activation via NMDA (Bak et al., 2009) and that lactate, compared to glucose, has an inferior influence on maintaining ATP homeostasis (Lange et al., 2015). Furthermore, the overall glucose, lactate and oxygen balance in the brain is not favoring the ANLSH (Dienel, 2012). Along this line and in opposition to the ANLSH, the evidence of an increased neuronal NADH:NAD<sup>+</sup> ratio in the stimulated brain of awake mice, seems to corroborate the idea of a preferential anaerobic metabolism in neurons in response to increased energy demand by neuronal activation, independent from lactate support by neighboring glial cells (Díaz-García et al., 2017). A recent study however showed the existence of a lactate gradient between astrocytes and neurons in awake mice (Mächler et al., 2016). Therefore, lactate metabolism and neuro-glia metabolic adaptations in the brain seem to be rather intricate, with results varying based on the system studied, experimental condition, etc. leading to poor scientific consensus (Dienel, 2012).

### 1.3 Metabolic support in white matter

Although white matter consumes on average less glucose than gray matter does (3.80 mg/100 g per min, white matter, 8.05 mg/100 g per min, gray matter; Reivich et al., 1979), white matter neuronal axonal projections require considerable metabolic support from neighboring glial cells. The main energy consuming tasks for established projecting fibers are the maintenance of membrane potential, the AP propagation, and other housekeeping activities, such as the axonal transport of proteins, vesicles and organelles to the pre-synaptic terminals. Together with other housekeeping processes, axonal transport accounts for about 25% of energy consumed (calculated in  $6.88 \cdot 10^{22}$  ATP molecules/m<sup>3</sup>/s; Harris & Attwell, 2012) and requires continuous microtubule polymerization (GTP-dependent process) which offers a solid track along which molecules can move through the ATP-powered activity of motor proteins (e.g. kinesin and dynein; Stryer, 1995). Any perturbation of this process contributes to pathological events that lead to neurodegeneration, as observed in multiple diseases such as amyotrophic lateral sclerosis (ALS) and hereditary spastic paraplegia (HSP; Millecamps & Julien, 2013). The propagation of action potentials along axons is also an ATP-dependent process: in order to maintain the ability of conducting action potentials (APs) axons need to maintain a negative membrane potential (around -70 mV) by establishing and keeping ion gradients across the membrane by action of Na/K-ATPase. The maintenance of the membrane resting potential and the constant transfer of APs, combined account for most of the remaining axonal energy needs (Harris & Attwell, 2012). At each AP propagation, voltage dependent ion channels let the ions follow their respective gradient generating current (i.e. flux of electric charges): initially, sodium ions flow into the axonal compartment and at the AP peak (depolarization) the potassium ions exit the axon, thereby inverting the current and repolarizing the membrane. By the end of the AP, the gradients of both ions have to be restored by Na/K-ATPase to allow propagation of a second AP.

In myelinated axons, less energy is needed compared to unmyelinated fibers (Stiefel, Torben-Nielsen, & Coggan, 2013). The lower energy requirement for AP propagation introduced by myelin, comes from the electrical insulation which allows saltatory AP conduction instead of wave-propagation, i.e. AP are localized events at the Nodes of Ranvier (Harris & Attwell, 2012; Hartline & Colman, 2007; Waxman, 1977). However, a disadvantage of the insulation provided by myelin is the physical barrier it represents for the axon, limiting its free-access to extracellular substrates and

energy supply. In white matter, most of the surface of the axon is in fact ensheathed by several layers of lipid membranes, leaving only a few percent of 'naked axon' in correspondence of the Node of Ranvier (Nave, 2010). Therefore, while myelin provides both, the benefit of an enhanced velocity of AP propagation and energy-saving saltatory conduction, it restricts the transfer of substrates from the extracellular reservoir of metabolites into the axon (J. Hirrlinger & Nave, 2014). However, this restriction might be overcome by the supply of energy substrates directly from oligodendrocytes and their myelin to the axon.

In a series of pivotal experiments addressing energy metabolism in acute optic nerve preparations as a model system for white matter tracts, it has been reported that axonal AP propagation, measured as compound action potentials (CAP; the integrated activity of all axons within the nerve), can be fueled by several different substrates including glucose, fructose, lactate and pyruvate (Brown, Wender, & Ransom, 2001). Furthermore, when the nerves were challenged by high frequency stimulation or by ischemic conditions mimicked via oxygen-glucose-deprivation (OGD) the functional conduction could be maintained for a short time window thanks to glycogen, stored in astrocytes and mobilized as lactate, which could be conveyed to axons for energy production (Brown, Baltan Tekkök, & Ransom, 2004; Brown, Tekkök, & Ransom, 2003; Tekkök, Brown, Westenbroek, Pellerin, & Ransom, 2005). When provided in replacement of glucose, lactate was able to sustain optic nerve's CAP indicating that this metabolite can supply mitochondrial TCA and ATP production in axons bypassing glycolysis (Brown et al., 2003, 2001). Remarkably, several other substrates that could be used by cells to produce energy (e.g. octanoate, sorbitol, alanine, aspartate, and glutamate) failed to support axonal function. Among these substrates also  $\beta$ -hydroxybutyrate, normally produced by the liver under ketogenic conditions, unexpectedly failed to maintain CAP in isolated optic nerves (Brown et al., 2001).

Besides astrocytes, it was recently discovered that also oligodendrocytes metabolically support axons by providing lactate to the axons they ensheath (Fünfschilling et al., 2012) and the failure of this support mechanism leads to a progressive loss in small caliber axons, as displayed by the MCT1<sup>+/-</sup> mutant mice, a model for amyotrophic lateral sclerosis (ALS; Lee et al., 2012). This opens to two possible scenarios where oligodendrocytes are leading the metabolic support using their myelin as a functional bridge for the delivery of substrates: 1) lactate in particular, provided by glycolytic astrocytes, might reach oligodendrocytes via gap junctions and be shuttled to the axon,



thereby avoiding the bottle neck of the transport at the nodes of Ranvier (J. Hirrlinger & Nave, 2014); II) lactate is produced by glycolytic oligodendrocytes themselves to fuel axons (Fünfschilling et al., 2012). The importance of oligodendroglial support to axons is emphasized by the axonal loss described in PLP1 knock out mice. In PLP1<sup>KO</sup> mice the genetic ablation of PLP/DM20, thought to influence myelin sheath stability (Duncan, Hammang, Goda, & Quarles, 1989) affects primarily oligodendrocytes but leads to axonal pathology with described impairment of fast axonal transport (Edgar et al., 2004) and morphological defects. The axonopathy parallel between PLP1<sup>KO</sup> and MCT1<sup>het</sup> (Lee et al., 2012), is reminiscent of that shown by mouse models of mitochondrial diseases (Ferreirinha et al., 2004; Tarrade et al., 2006), suggesting that energy failure in the axons is a crucial aspect of disease progression *in vivo*.

A metabolic support from oligodendrocytes also implies a regulation mechanism to maximize energy production and communication between axons and oligodendrocytes, and vice versa, seems to be required (Micu, Plemel, Caprariello, Nave, & Stys, 2018). Although authors often refer to it as “axo-glia” or “axo-myelinic” synapse (Stys, 2011), the mechanisms through which axons communicate to oligodendrocytes and astrocytes, substantially differ from those observed in gray matter and theoretical models are still at their infancy. Neurons can release neurotransmitters (NTs) via vesicles fusion along the axonal membrane, without a specialized synaptic apparatus (Fields, 2011). The released NTs activate specific ionotropic and metabotropic receptors on the adaxonal side of myelin. The vesicular release of NTs exhibit low rates of spontaneous release (Bergles, Roberts, Somogyi, & Jahr, 2000) and can happen in activity-dependent manner (Stevens & Fields, 2000), as demonstrated by the astrocytes depolarization in response to retinal stimulation (Orkand, Nicholls, & Kuffler, 1966). Interestingly the axonal vesicular release of NTs seems to play a role in development, during white matter myelination-initiation by oligodendrocytes precursors cells (De Biase, Nishiyama, & Bergles, 2010). The evidence of neuronal vesicular NT release, in activity-dependent manner, influencing myelination was provided by interfering with synaptic vesicle release of neurotransmitters: Tetanus toxin, by inhibiting axonal vesicular fusion and NT release, directly impairs myelination (Mensch et al., 2015). Vice versa, artificial stimulation of neuronal activity increases myelin sheath formation (Mensch et al., 2015). Besides the role in controlling and establishing myelination, the axonal NT release controls the trophic support of axons by modulating glial metabolic support (Nave, 2010; Stys, 2011).

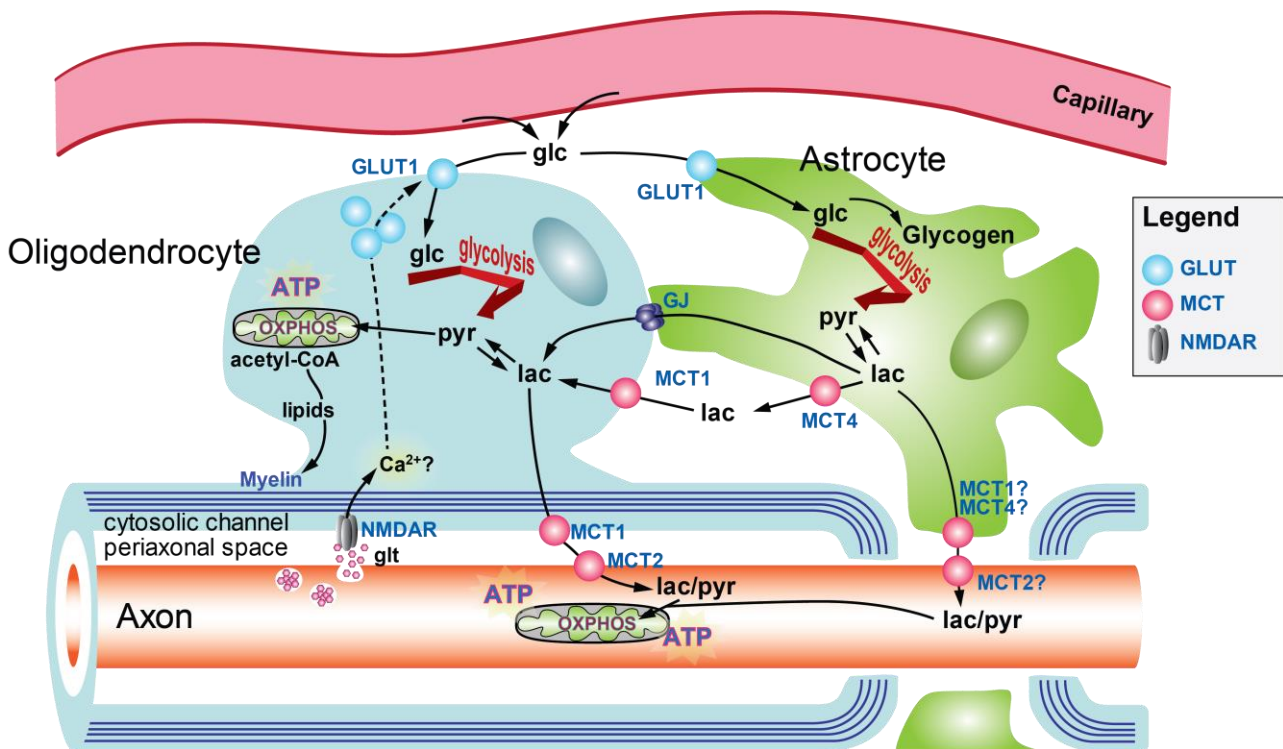


**Figure 2. Proposed axo-glia metabolic coupling in white matter.**

Following myelination, oligodendrocytes contribute to support axonal energy homeostasis by shuttling metabolites (mainly lactate) into the axonal compartment, following functional activation of oligodendrocytic NMDAR facing the periaxonal space. The signaling cascade triggered by NMDAR likely involves  $Ca^{2+}$  and drives the insertion of GLUT1 into oligodendrocytes' plasma membrane. The inserted GLUT1 increase glucose flow into the oligodendrocyte and support the anaerobic production of lactate via glycolysis, which can be shuttled into the active axon. Astrocytes are connected via gap junctions to oligodendrocytes and take part to this metabolic interplay by supporting the axons at the nodal regions. Glc: glucose; pyr: pyruvate; lac: lactate; glt: glutamate; MCT: monocarboxylate transporter; GLUT: glucose transporter; GJ: gap junction; OX-PHOS: oxidative phosphorylation; NMDAR: N-Methyl-D-aspartate receptor. ATP: adenosine triphosphate. Adapted with permission from Hirrlinger & Nave, 2014.

A step towards the understanding the link between the contribution of oligodendrocytes to axonal metabolic support (Fünfschilling et al., 2012) and the role of axonal NT release in modulating was represented by the findings that: I) oligodendrocytes mobilize their GLUT1 glucose transporter upon NMDAR stimulation; II) myelinated optic nerves from  $cNR1^{KO}$  (oligodendrocyte-conditional NMDA receptor knock-out), challenged with oxygen-glucose deprivation (OGD), fail to recover when returned to oxygen-glucose but are indistinguishable from wild-type when provided

with oxygen-lactate; III) NMDA preincubation of isolated optic nerves enhances their functional integrity (Saab et al. 2016).

In most of these studies, axonal energy status has been estimated indirectly by analyzing CAP-maintenance or morphological damage as functional readout, linked to energy maintenance and failure. Although it is logical to think to a correlation between conduction and energy state in white matter, the latter is better defined by the cellular redox state and ATP content. Other factors in fact, can influence the functional readout represented by nerve conduction and direct conclusions on the ATP content or redox state of axons might not be as trivial. To provide a better in depth understanding of white matter energetics, we imaged axonal ATP directly, by taking advantage of the genetically encoded fluorescent sensor for ATP "ATeam1.03<sup>YEMK</sup>" (Imamura et al., 2009). Transgenic mice with neuronally-targeted expression of this sensor were generated and used to simultaneously monitored CAPs and ATP in excised optic nerves *ex vivo*.

#### 1.4 Genetically encoded FRET sensors for metabolites

Fluorescence resonance energy transfer (FRET) is a non-radiative mode of energy transfer via dipole-dipole interaction between two different fluorophores termed FRET pairs. The FRET pairs consist in the donor and the acceptor fluorophores and these have to be closely associated in space, usually within few nanometers (Pawley, 2006). The donor fluorophore, upon excitation, releases energy while the acceptor absorbs part of this energy. The emission spectrum of the donor typically overlaps with the excitation of the acceptor fluorophore. The amount of non-radiative energy transmission is described by the quantum yield  $\Phi$ , which can be defined via transfer rate constants of the different decay channels  $k$ :

$$\Phi_{donor} = \frac{k_{donor,radiative}}{k_{donor,radiative} + k_{donor,non-radiative}}$$

The acceptor thus, acts as a quencher and the closer the acceptor comes to the donor, the more energy can be transferred non-radiatively, altering the donor quantum yield:

$$\Phi_{donor,acceptor} = \frac{k_{donor,radiative}}{k_{donor,radiative} + k_{donor,non-radiative} + k_{donor,dipole-dipole}}$$

This defines the efficiency of FRET ( $E_{FRET}$ ) as a dimensionless value that measures what fraction of the transferred energy is conveyed via non-radiative dipole-dipole interaction:

$$E_{FRET} = 1 - \frac{\Phi_{donor,acceptor}}{\Phi_{donor}}$$

FRET efficiency is maximal when the dipole moments are in the same plane and aligned. What ultimately drives the energy transfer is thus the electromagnetic interaction between the emission and absorption dipole moments of donor and acceptor, respectively (Pawley, 2006).

Genetically encoded metabolite sensors are chimeric proteins that take advantage of FRET between a donor and an acceptor fluorophores. The strategy to genetically assemble these fusion peptides, is to genetically modify a protein that normally binds the metabolite of interest (e.g. for ATP, the bacterial  $\epsilon$  subunit of the  $F_0F_1$ -ATP synthase from *Bacillus subtilis*, Imamura et al., 2009) and link it to FRET-pairs at N- and C- termini. In order to correlate changes in concentration of the metabolite of interest the construct has to satisfy the following requirements: I) the binding to the metabolite of interest has to happen within the biologically-relevant concentration range of the target metabolite (i.e. the binding affinity of the sensor has to be as close as possible to the physiological concentration of the target metabolite); II) upon binding of the metabolites to its core, the sensor has to undergo a conformational change which results in a spatial repositioning of the FRET pairs; III) the dipole moments of the FRET pairs have to be oriented in parallel and correctly spaced in order to maximize FRET and the conformational change of the sensor has to determine a change in the orientation of the dipoles (the larger the change in dipoles orientation, the better the signal-to-noise of the sensor). Most FRET pairs used so far for genetically encoded metabolite sensors are CFP-YFP variants, but recently also red-shifted combination (e.g. mClover3/ mRuby3 provide wide FRET dynamic range; Bajar, Wang, Zhang, Lin, & Chu, 2016) have been described. Different FRET pairs carry different advantages/ disadvantages. A special combination of FRET pairs occurs when the acceptor is a dark fluorophore (e.g. YFP mutants, REACh (resonance energy-accepting chromoprotein, originally engineered as acceptors for EGFP; Ganesan, Ameer-Beg, Ng, Vojnovic, & Wouters, 2006), i.e. a fluorophore with very low quantum yield that are employed in FRET-FLIM. Dark acceptors offer, in this imaging technique, the considerable advantages of I) diminishing the bleed-through from the acceptor into the donor emission channel; II) improving FRET dynamic range; III) reducing phototoxicity as result of less excitation needed; IV) introducing

the possibility of using more fluorophores of different colors simultaneously as consequence of a narrower spectrum required by the FRET pairs (Bajar et al., 2016).

The first genetically encoded sensor for a molecule involved in energy metabolism was a glucose sensor based on a modified bacterial periplasmic glucose/galactose-binding protein: several sensors with different binding affinities for glucose were described (FLIP series; Fehr, Lalonde, Lager, Wolff, & Frommer, 2003). The glucose sensor was quickly followed by genetically encoded sensors for glutamate (FLIPE, iGluSnFR; Marvin et al., 2013; Okumoto et al., 2005), ATP (ATeam, GO-ATeam, PercevalHR; Imamura et al., 2009; Nakano et al., 2011; Tantama et al., 2013), NADH/NAD<sup>+</sup> (Peredox; Hung, Albeck, Tantama, & Yellen, 2011), lactate (Laconic; San Martín et al., 2013) and pyruvate (Pyronic; San Martín et al., 2014).

The ATeam series were the first FRET sensors described for ATP: ATeam1.03 ( $K_d = 3.3$  mM), ATeam3.10 ( $K_d = 7.4$   $\mu$ M), ATeam1.03<sup>YEMK</sup> ( $K_d = 1.2$  mM) and AT3.10<sup>MGK</sup> ( $K_d = 14$   $\mu$ M). The ATeam sensors with higher affinity (low  $K_d$ ) derived from a construct which employed a different  $\epsilon$  subunit (PS3; about 70% homology from the  $\epsilon$  subunit used in the ATeam1.03 series) of the F<sub>0</sub>F<sub>1</sub>-ATP synthase from *Bacillus subtilis*. The YEMK and MGK amino acid substitution around residues 60<sup>th</sup> and 132<sup>nd</sup> respectively of the N-terminal  $\beta$ -sandwich domain and C-terminal  $\alpha$ -helical domain of the  $\epsilon$  subunit, helped to tune the affinity for ATP (Imamura et al., 2009). GO-ATeam is a red-shifted ATP variant of the ATeam series, in which green fluorescent protein (GFP, mEGFP) and orange fluorescent protein (OFP, mKO $\kappa$ ) substituted the mseCFP and mVenus FPs. GO-ATeam is reported to have less affinity for ATP than all ATeam sensors, with a  $K_d = 7.2$  mM and showed improved pH tolerance in more acidic environments, in addition, the red-shifted FRET pairs allowed less phototoxic wavelengths (Nakano et al., 2011). Finally, PercevalHR (Tantama et al., 2013) is an improved (in terms of sensitivity range and fluorescence response) version of the original Perceval (Berg, Hung, & Yellen, 2009). Perceval are single cpFP sensors for ADP:ATP ratio and have fixed isosbestic point for absorbance at 455 nm. By exciting Perceval above (550 nm) and below (420 nm) it is possible to determine the ADP:ATP ratio in a ratiometric manner (Tantama et al., 2013).

## 1.5 FLIM – FRET detection

Fluorophores are excitable biomolecules that emit light particles (photons) upon de-excitation from an excited state caused by photon absorption. The emitted photon has less energy than the absorbed one and this produces a wavelength shift (Stokes shift). Intensity-based measurements of FRET ratio in living tissues carry one pitfall which is represented by the nature of FRET itself, i.e. the donor and acceptor fluorophores' different emission wavelengths  $\lambda$ . Photons with higher frequencies (shorter  $\lambda$ ) are scattered more than photons with lower frequencies (long  $\lambda$ ): this phenomena is known as "Rayleigh scattering" which relates the amount of scattering to  $1/\lambda$ . In microscopy, the higher the scattering of fluorescent light through a phase, the less the photon yield (or count) at the detector. It follows that, assuming constant conformation of a FRET probe, by moving the focus along the z-axis while imaging a tissue, donor's fluorescence intensity is lost faster than acceptor's fluorescence at increasing depth, resulting in an artefactual change of the calculated FRET ratio and misleading data interpretation. Therefore, in biological context, Rayleigh scattering effect during FRET intensity-measurements, poses an additional problem when a calibration of the probe is required.

In order to translate a biologically-relevant ratio into a define concentration of substrate, for which the FRET-probe is sensitive, the FRET probe should undergo a calibration procedure and any artifact contribution, caused by e.g. the Rayleigh scattering, should be accounted for when fitting the calibration curve to the measured data. The relationship of FRET-ratio and substrate binding is described by the Hill equation (Figure 3B). In order to reconstruct the relationship between ratiometric fluorescence intensity and substrate concentration, it is customary to expose the FRET probe to a range of substrate concentrations around its dissociation constant. In cells, the calibration is achieved by equilibrating the extracellular solution with the cytosol of the cell and, depending on the sensed metabolite, by blocking its production and/or consumption. Many metabolites have their dedicated transporter (e.g. glucose, lactate, glutamate) which can be used for this purpose. However, ATP and other molecules relevant for metabolism, have no dedicated transporter and their equilibration in the cell requires cell membrane permeabilization. The calibration procedure will also require equilibration of the metabolites of interest in the same environment of the experimental condition to avoid artifact contribution. However, permeabilization of the phospholipid membranes in a highly organized tissue can be arduous as often results in considerable damage and lading to an altered structural organization and consequently, undesired changes in the focal plane. Also, any

attempt of calibration in cells will make the calibration curve not-usable for complex tissue in view of the mentioned Rayleigh effect. We therefore used an alternative imaging method which is relatively insensitive to photobleaching and photon scattering: fluorescence lifetime imaging microscopy (FLIM; Marx, 2017). FLIM measures the characteristic decay curves of fluorophores from which the corresponding lifetimes can be extracted. Taking ATeam1.03<sup>YEMK</sup> as example for a FRET sensor, in FRET-FLIM analysis the relevant moiety of the sensor is the donor (msecFP, for ATeam1.03<sup>YEMK</sup>) and its quenched state is reported as an indirect measure of the proximity of the acceptor (i.e. FRET). In correspondence of high FRET (e.g. ATeam1.03<sup>YEMK</sup> saturated by ATP and in “close” conformation) the donor fluorophore is highly quenched by the acceptor and its lifetime  $T_{av-w}$  is very short: this condition occurs when a cell is in its resting state and a lot of ATP is present (in mM order, Pathak et al., 2015; Rangaraju, Calloway, & Ryan, 2014). FLIM provides a quantitative way of expressing FRET and, given its relative independence to phenomena such as the Rayleigh scattering, calibration curves obtained in cells can be used to derive ATP concentrations in tissue with reasonable confidence.





## 2 Objectives

The general aim of this thesis is to study white matter metabolism with a special focus on the underlying mechanisms of axo-glia metabolic coupling. What is the correlation between metabolism and axonal ability of transmitting action potentials to the synaptic terminals? How are glial cells contributing to the functional integrity of axons in white matter? This study aims at contributing to the answer to those questions and aims at understanding the functional link that connects metabolism to the axonal activity.

To achieve these goals a white matter model is used: the optic nerve. The optic nerve can be isolated and used as an ex-vivo system that preserves white matter structure. Two state of the art techniques are combined to allow the synchronized monitoring of nerve conduction and axonal ATP as readout for metabolism.

Thus, by simultaneously monitoring optic nerve CAP and axonal ATP, our aims can be summarized: I) describe the axo-glia metabolic coupling under physiological conditions; II) test the hypothesis that designates lactate as the central metabolite for metabolic coupling; III) understand the role of glial cells in providing support during phases of transient energy deprivation and identify the possible metabolic pathways involved in axonal ATP homeostasis; IV) identify the pathological implications of impaired axonal metabolism in models of neurodegeneration where the axo-glia coupling is compromised.



### 3 Results

#### 3.1 ATeam1.03<sup>YEMK</sup> and ThyAT transgenic mouse line

Genetically encoded ATP-sensor ATeam1.03<sup>YEMK</sup> reports ATP levels with very high spatial and temporal accuracy (Imamura et al., 2009). We used ATeam1.03<sup>YEMK</sup> to track axonal ATP for studying white matter metabolism and the contribution of glial cells to axonal energy homeostasis during electrical activity. ATeam1.03<sup>YEMK</sup> binds directly to ATP via the bacteria-derived  $\epsilon$ -subunit of the  $F_0F_1$ -ATP synthase. The binding produces a conformational change of the sensor resulting in a spatial relocation of the genetically linked fluorophores (FRET-pairs) mseCFP and mVenus at the N- and C terminus of the  $\epsilon$ -subunit, respectively (Figure 3A). In absence of ATP, ATeam1.03<sup>YEMK</sup> is in its “open” configuration, permitting poor FRET between the two fluorophores. The binding of ATP molecules to the sensor produces a reorientation of the fluorophores’ dipoles in the FRET pairs and consequently an increase in FRET. The binding kinetics of ATeam1.03<sup>YEMK</sup> are described by the Hill equation (Figure 3B), following the typical sigmoidal course of a positively cooperative binding, having its  $K_d$  (apparent dissociation constants) equal to 1.2 mM (Imamura et al., 2009).

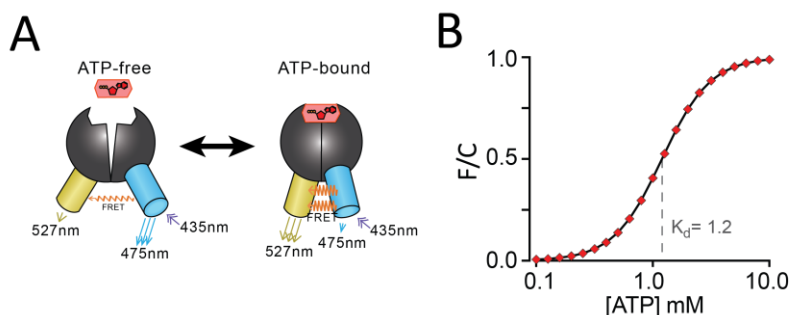


**Figure 3.** ATeam1.03<sup>YEMK</sup> is a genetically encoded FRET sensor for ATP

(A) Binding of ATP induces a conformational change in the genetically encoded ATP-sensor ATeam1.03<sup>YEMK</sup> thus increasing the FRET effect (YFP emission upon CFP excitation) and simultaneous decreased emission of CFP (upon CFP excitation). The ratio between FRET and CFP can thus be correlated to the concentration of ATP present in the cell.

(B) ATP-binding kinetic of ATeam1.03<sup>YEMK</sup> reported as FRET/CFP (F/C) ratio, follows a positively cooperative binding with a calculated  $K_d$  of 1.2 mM and  $n$  (Hill coefficient) of 2.1 (Imamura et al., 2009).

We generated transgenic mice for pan-neuronal *in vivo* expression of this sensor driven by the murine Thy1.2 promoter (Caroni, 1997). Upon pronuclear microinjection into the fertilized mouse oocytes, 21 copies of the transgene were inserted into the mouse genome, creating a new line [B6-Tg(Thy1.2-ATeam1.03<sup>YEMK</sup>)AJhi, also referred to as ThyAT]. The transgenic ThyAT mouse line

displayed widespread neuronal expression (Figure 4). In the retina, fluorescence marked ganglion cells and their axons (Figure 4G-H) project to the thalamic lateral geniculate nucleus through the optic nerve (Figure 4I-K).

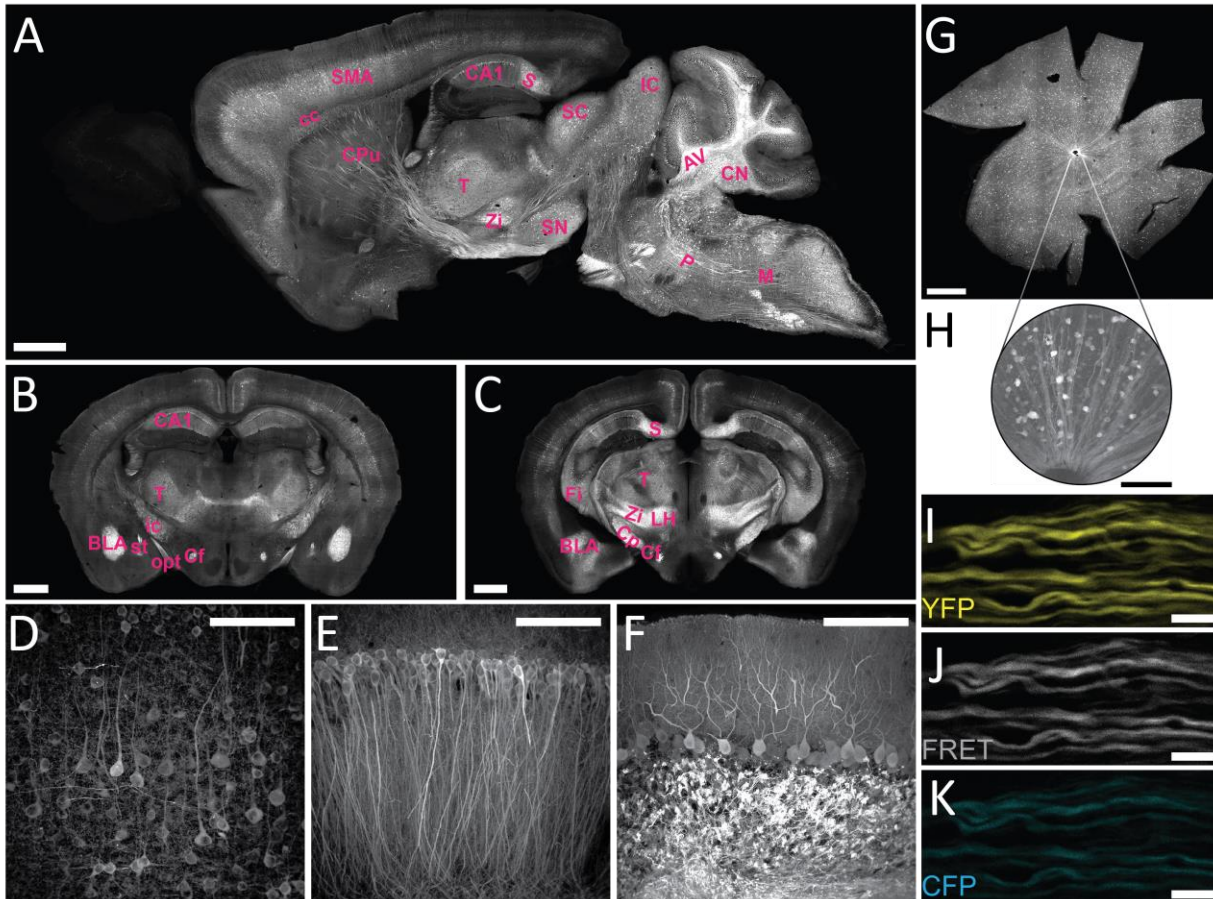


**Figure 4.** Characterization of the expression pattern of the newly generated B6-Tg(Thy1.2-ATeam1.03<sup>YEMK</sup>)A1hi (ThyAT)-mouse line.

**(A)** Sagittal section of the brain highlights broad ATeam1.03<sup>YEMK</sup> expression in neurons in almost all brain regions with the exception of the olfactory bulb. Scale bar: 1 mm. **(B), (C)** ThyAT expression pattern in coronal brain sections revealing sensor expression e.g. in thalamus, hypothalamus, amygdala, cortex and hippocampus. Scale bar: 1 mm. Abbreviations used in panels A-C are: AV: arbor vitae; BLA: basolateral amygdalar nucleus, anterior; CA1: CA1 region of the hippocampus; cc: corpus callosum; Cf: columns of the fornix; CN: cerebellar nuclei; Cp: cerebral peduncle; CPU: caudate putamen; Fi: fimbria; IC: inferior colliculus; ic: internal capsule; LH: lateral area of the hypothalamus; M: medulla; opt: optic tract; P: pons; S: subiculum; SC: superior colliculus; SMA: somato-motor area (Cortex); SN: substantia nigra; st: stria terminalis; T: thalamus; Zi: zona incerta (thalamus). Scale bar for B, C: 1mm. **(D)** Within the cortex, neurons expressing ATeam1.03<sup>YEMK</sup> are clearly visible including their processes. Note the lack of ATP-sensor localization to the nucleus. Scale bar: 100  $\mu$ m. **(E)** Also in the hippocampus neurons strongly express ATeam1.03<sup>YEMK</sup>. Scale bar: 100  $\mu$ m. **(F)** In the cerebellum, Purkinje cells express the ATP-sensor. In addition, incoming mossy fibers strongly express ATeam1.03<sup>YEMK</sup>. Scale bar: 100  $\mu$ m. Images in panels A, D-F are obtained on brain slices from a 4 month old animal, images in panels B and C are from mice at the age of 2 month. **(G)** Expression pattern of the ATP-sensor in the retina. Thy1.2 promoter drives the expression of ATeam1.03<sup>YEMK</sup> in ganglion cells. Scale bar: 1 mm. **(H)** Magnified view of neurons and axons in the retina expressing ATeam1.03<sup>YEMK</sup>. Scale bar: 100  $\mu$ m. **(I), (J), (K)** Representative images of optic nerve axons showing the YFP channel (I), FRET channel (J) and CFP channel (K). The ATeam1.03<sup>YEMK</sup> expression is present in different axons independent of their diameter. Scale bar: 10  $\mu$ m.

To initially assess functionality of the genetically encoded ATP FRET-reporter in the ThyAT line, we prepared primary mixed cultures from mouse E-13 embryos. Subsequently, we monitored the ATeam1.03<sup>YEMK</sup> signal in transgenic expressing neurons (Figure 5) while inducing intracellular ATP changes using a live-imaging epifluorescence microscope. We challenged neuronal energy metabolism by exposing neurons to glutamate, different concentrations of potassium, Na/K-ATPase block and inhibitors for glycolytic flux/TCA cycle while monitoring intracellular neuronal ATP levels. Under glutamate and potassium stimulation the intracellular ATP concentration has been previously reported to be considerably affected (Foo, Blumenthal, & Man, 2012). We found consistent decreases under all mentioned treatments. The strongest effect was observed under simultaneous exposure to 1 mM iodoacetic acid and 5 mM azide (blockers of glycolysis and OX-PHOS respectively, Figure 5B-C). Notably, after 10 min of glutamate stimulation, the ATeam1.03<sup>YEMK</sup> ratio dropped by 60% from its baseline value. This factor was comparable to that reported by Foo et al. (2012) where ATP was found to be reduced of about 50%, when neurons were exposed to 50  $\mu$ M glutamate for 60 min. However, given the sample number was limited (n = 1, 4 neurons), additional experiments are necessary in order to draw relevant conclusions.

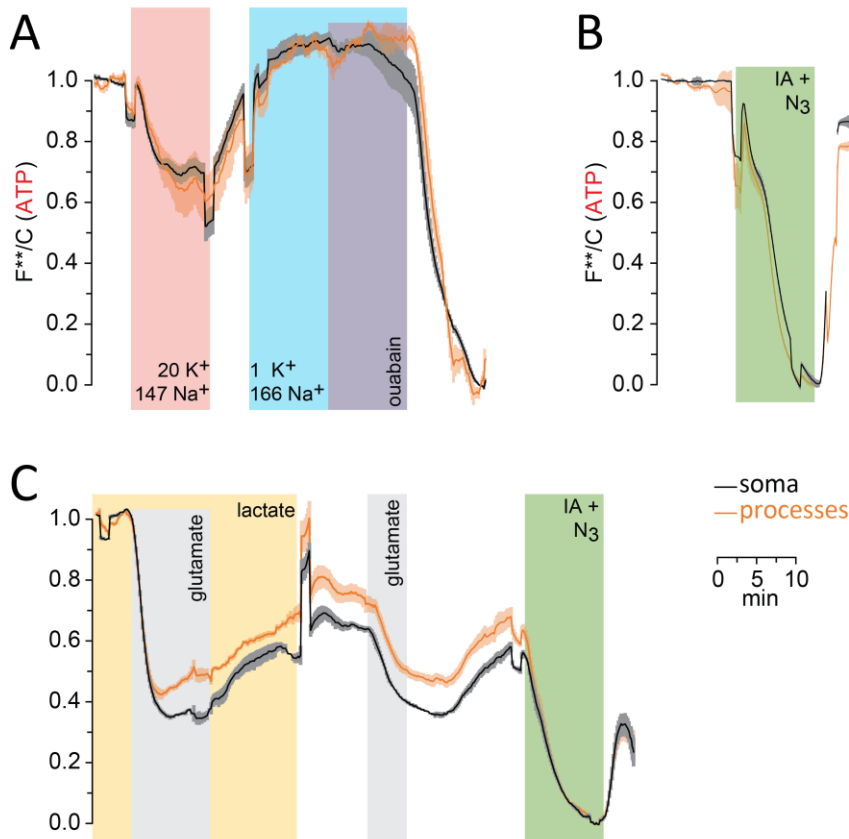


**Figure 5.** The ATP sensor Ateam1.03<sup>YEMK</sup> in cultured neurons detects ATP fluctuations during different treatments.

Primary neuronal cultures were prepared from transgenic mice expressing the ATP sensor Ateam1.03<sup>YEMK</sup> in neurons and ATP levels were monitored using live cell fluorescent imaging. Soma and processes from neurons are indicated in dark-gray and orange respectively. **(A)** ATP responses to subsequent increase/decrease in extracellular potassium and increase/decrease in extracellular sodium ( $K^+ = 20$  mM/  $Na^+ = 147$  mM and  $K^+ = 1$  mM/  $Na^+ = 166$  mM, red box and blue box respectively) from the physiological sodium-potassium concentrations (161 mM and 5.4 mM respectively) followed by exposure to 100  $\mu$ M ouabain (Na/K-ATPase blocker). **(B)** Blockade of ATP production with exposure to iodoacetic acid (1 mM, irreversible glycolysis blocker) and azide (5 mM, reversible OX-PHOS inhibitor) produces a fast and steep decay in the FRET-ratio. **(C)** Neuronal ATP fluctuates under subsequent exposure to glutamate/lactate, glutamate/glucose and iodoacetic acid/azide. Traces represent single experiments (neurons from a single mixed culture) variable number of cells (2-6 cells, 3-9 processes).

Nevertheless, given the consistency of the decay of ATeam1.03<sup>YEMK</sup> signal in correspondence to each of the treatments, we proceeded to investigate ATP dynamics in white matter. Given our primary aim of correlating axonal energy metabolism during electric activity, we acutely isolated optic nerves from adult ThyAT mice, assessing axonal ATP levels by confocal microscopy while simultaneously monitoring stimulus-evoked CAPs (Figure 6A).

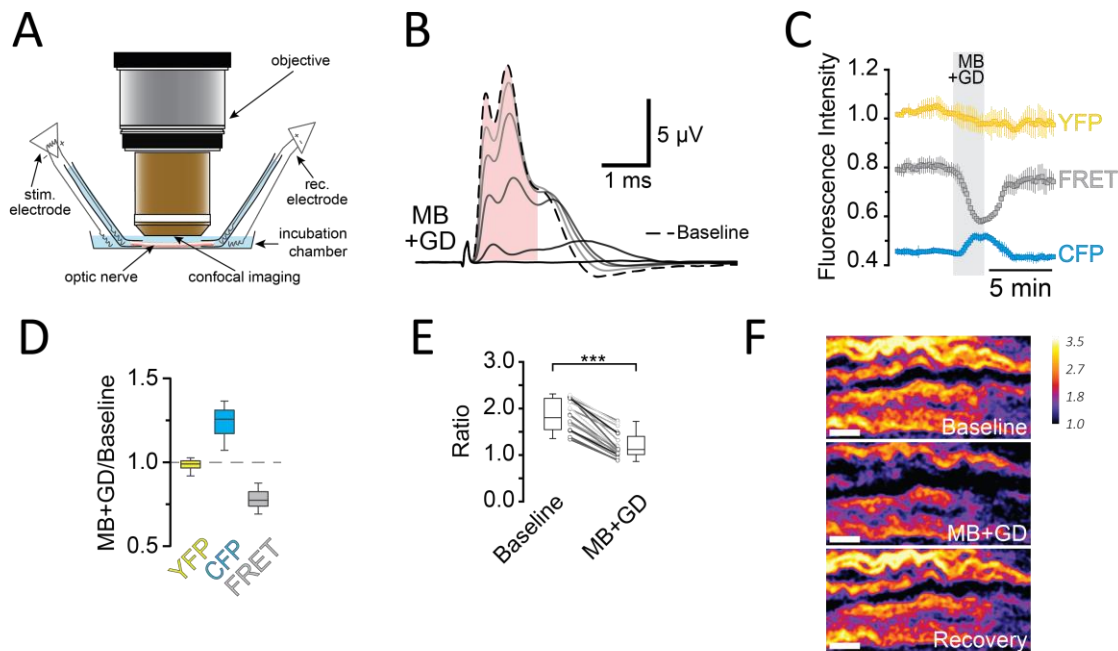


**Figure 6. Imaging of ATP combined with electrophysiology in acutely isolated optic nerves of ThyAT-mice.**

(A) Schematic representation of the set-up to acquire evoked CAPs in the optic nerve and to simultaneously investigate relative ATP levels by electrophysiology and confocal imaging, respectively. (B) Transition of the CAP waveform, acquired every 30 s, from baseline (dashed line) to exposure to MB + GD). The shaded area indicates the area under the CAP waveform considered for analysis. (C) Time course of fluorescence intensity recorded in the YFP, FRET and CFP- channels during application of mitochondrial blockage (MB) and glucose deprivation (GD) for 2.5 min. Values are normalized to YFP intensity prior to application of MB + GD ( $n = 3$  nerves). Time resolution: 10.4 s. (D) The combination of MB and GD is a fast and reliable way to deplete ATP in axons of the optic nerve. ATP depletion is measured as a decrease in FRET and increase in CFP, calculated as ratio between fluorophore intensity during MB + GD, over fluorophore intensity at baseline condition (MB + GD/Baseline). Notably, YFP emission upon YFP excitation remains unchanged ( $n = 5$  nerves). (E) FRET/CFP ratio values (not normalized) during baseline and MB + GD. The boxplots show summarized data of  $n = 19$  nerves, lines in between boxplots show changes in the FRET/CFP ratio of all 19 individual nerves. (F) Ratiometric images displaying the FRET/CFP ratio of the ATeam1.03<sup>YEMK</sup> sensor in the axons of the optic nerve during ATP depletion following MB + GD. The phases before (Baseline) and after (Recovery) are also shown. Scale bar: 10  $\mu\text{m}$ . Asterisks in (E) indicate significant differences among conditions: \*\*\* $p < 0.001$ ; Welch's t test.

Expression of the ATP-sensor in myelinated axons appeared robust in all recorded channels (Figure 4 I-K; see methods for imaging acquisition details). To verify sensor function also in the ex vivo preparations of optic nerve, we subjected the nerve to mitochondrial OX-PHOS blockade and simultaneous glucose removal (MB + GD). An immediate drop of the FRET signal (gray trace, Figure 6B) and an increase in CFP emission (blue trace) indicated that ATP levels in axons dropped. Changes in pH can modulate YFP-fluorescence (Nagai, Yamada, Tominaga, Ichikawa, & Miyawaki, 2004), thus provoking an artefactual change in the recorded FRET channel. Even though ATeam1.03<sup>YEMK</sup> has been

reported to be almost insensitive to pH variations within the physiological range (Imamura et al., 2009; Surin et al., 2014) we systematically monitored the acceptor fluorescence by direct excitation/emission during all reported experiments. During MB + GD the acceptor fluorescence was unchanged (Figure 6B-C, yellow trace), suggesting that pH changes are not the cause of altered FRET signals under this condition.

The ratio of FRET/CFP fluorescence (F/C-ratio) was calculated as a measure of cytosolic ATP concentration (Figure 6D) by dividing the average intensity of the corresponding channels for each frame and every time point (unless differently noted). The baseline F/C-ratio (control condition; 10 mM glucose) was calculated as the average F/C-ratio during the last 5 min of the initial baseline imaging time series (variable between 15-20 min). F/C-ratio was found to be similar and stable between the different nerves analyzed (Figure 6D), while after 2 min of MB + GD treatment, the ratio was reduced by  $35.1\% \pm 1.7\%$  ( $n = 19$  nerves; Figure 6D). In further experiments, F/C-ratios were normalized between MB one (10 mM glucose) and zero (MB + GD; Figure 7A). As expected, during MB + GD the decrease in axonal ATP was mirrored by a decay of CAPs, reflecting conduction blocks (Figure 7B-C). Strikingly, also the relative decline rates of axonal ATP and conductivity were similar (Figure 7D).

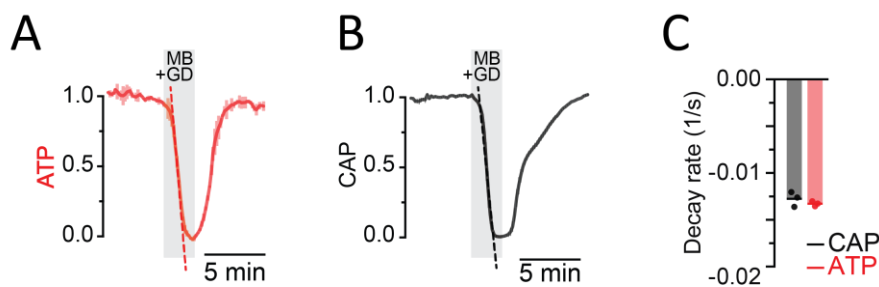


**Figure 7. ATP and CAP Area recordings during simultaneous mitochondrial blockade and glucose deprivation.**

**(A)** To assess ATP variations, the ratio of the fluorescence intensities of the FRET and CFP-channel was calculated (FRET/CFP ratio) and normalized to baseline (set as 1) and MB + GD (set as 0). The red dashed line visualizes the slope of ATP decay at the point of maximal velocity of ATP decay during mitochondrial blockage (MB + GD,  $n = 3$ ). **(B)** Evoked compound action potential (CAP) area is given as the normalized curve integral during MB + GD. The black dashed line represent the slope at the point of maximal velocity of CAP changes during MB + GD treatment ( $n = 3$ ). **(C)** Stripe plot describing CAP (black) and ATP (red) kinetics, expressed as maximal variation per s, during MB + GD ( $p = 0.39$ ,  $n = 3$ , Welch's t-test). Dots show individual data points, bars and lines represent the mean of all data. Red and black shaded areas adjacent to the traces in (A) and (B) represent SEM for ATP and CAP measurements, respectively.



### 3.2 Models of energy deprivation

We compared ATP and CAP dynamics in response to different modes of energy deprivation (Table 1; Figures 8-11). The paradigms used for energy deprivation included: glucose withdrawal (also referred to as aglycemia, GD; Figure 8), inhibition of mitochondrial OX-PHOS by pharmacological inhibition (MB, 5 mM azide; Figure 9A-C), through oxygen replacement with nitrogen in the aCSF ( $N_2$  or anoxia; Figure 9D), through MB + GD (combination of these, Figure 10A) and through oxygen glucose deprivation (OGD, a combination of hypoxia and aglycemia; Figure 8B).

Condition	Short description	Effect	Figure(s)
<b>GD</b>	Glucose deprivation	<i>ATP is not generated from glucose, however glycogen and other energy sources can be utilized</i>	6A-C; 9A-B, 9D-F
<b>MB</b>	Mitochondria complex IV inhibition by 5 mM azide	<i>Fast inhibition of OX-PHOS and mitochondrial ATP production. Glycolysis still active</i>	7A-C; 9A-B, 9D-F
<b><math>N_2</math></b>	Hypoxic condition created by replacement of $O_2$ with $N_2$ in the incubating chamber	<i>Oxygen is replaced by <math>N_2</math> in the incubation chamber: OX-PHOS efficiency is strongly reduced</i>	7D; 9C
<b>MB + GD</b>	Simultaneous inhibition of mitochondrial activity by 5 mM azide and glucose deprivation	<i>No OX-PHOS, no glycolytic production of NADH and ATP from glucose</i>	8A; 9A-B, 9D-F; [4B-F; 5A-C]
<b>OGD</b>	Simultaneous hypoxic condition and glucose deprivation	<i>Strong reduction of OX-PHOS, no glycolytic production of NADH and ATP from glucose</i>	8B; 9A-B, 9D-F

Table 1. Summary of energy deprivation models in the ex-vivo preparation of optic nerve.

### 3.2.1 Glucose deprivation

During glucose deprivation we observed a slow loss of ATP and CAP starting at about 13 minutes after the removal of glucose from the aCSF (Figure 8C). After 45 minutes of exposure the loss of CAP was complete and no response could be elicited (Figure 8A), ATP signal followed the kinetics of the CAP, reaching its relative zero by the end of the treatment (Figure 8C). Interestingly, at the end of GD, we found changes in fluorescence intensities in each of the three channels (Figure 8B) comparable to those observed during MB + GD (Figure 6D).

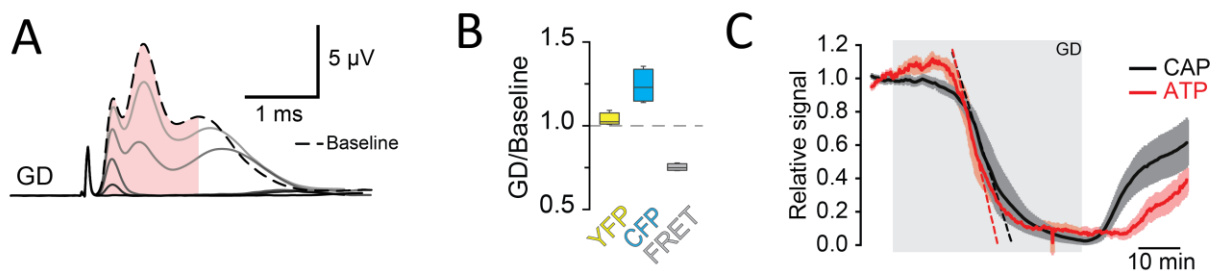


**Figure 8. Impairment of axonal ATP and CAP by glucose removal from the aCSF (glucose deprivation, GD, 45 min).**

**(A)** Single CAP waveform obtained under control conditions (baseline, dashed line) and during exposure of GD (total 45 min). Single waveforms are separated by 330 s and progressively decay in amplitude. The shaded area indicates the range of the CAP waveform set to quantify the CAP area for the baseline condition, the same time window was used for analysis of CAPs at subsequent time points. Under all conditions, no CAP could be elicited any longer by electrical stimulation at the end of the energy-depleting paradigm. **(B)** Changes of the fluorescence signal, relative to baseline, during glucose deprivation (GD). Fluorescence intensities of the three recorded channels between 44.75 min and 45 min of incubation with GD, were averaged ( $n = 4$  nerves). **(C)** GD (45 min, gray-shaded box) induces similar ATP (red) and CAP (black) decays starting at around 13 min after onset of the treatment. Red and black dashed, straight lines represent the maximum velocity of ATP and CAP decay (see Figure 9 for quantification). When 10 mM glucose is restored in the circulating aCSF, CAP recovery precedes ATP restoration ( $n = 4$  nerves).

Black and red shaded areas adjacent to each trace represent SEM for CAP and ATP measurements, respectively.

When nerves were reperfused with aCSF containing 10 mM glucose, following 45 min of aglycemia, CAPs recovered with a delay of about 3 min and the recovery of CAPs preceded the restore of ATP levels by several minutes (Figure 8C and 11D for quantification; GD). These data suggest that optic nerves, in absence of external substrates can keep on producing ATP, presumably by metabolizing astrocyte-derived glycogen (Brown et al., 2005).

### 3.2.2 Mitochondrial inhibition by azide or hypoxia

We inhibited mitochondrial OX-PHOS using azide (5 mM for 5 minutes; Figure 9A-C; MB) while leaving glucose available in the circulating aCSF. MB produced very quick changes in ATP and CAP (Figure 9C), comparable with those observed during MB + GD (Figure 7A-C and Figure 10A). Within few minutes loss of ATP and CAP was complete, indicating the prominent role of mitochondria in energy production in white matter. However, when the optic nerves were deprived of oxygen after its substitution with N<sub>2</sub> (gas mixture of 95% N<sub>2</sub>, 5% CO<sub>2</sub>; Figure 9D), the ATP signal, instead of decaying over time as predicted by the MB exposure, was found to increase by approximately 20-30% (after 45 min) mirroring a decrease in nerve conduction (about 60% decrease from baseline; Figure 11A-B).

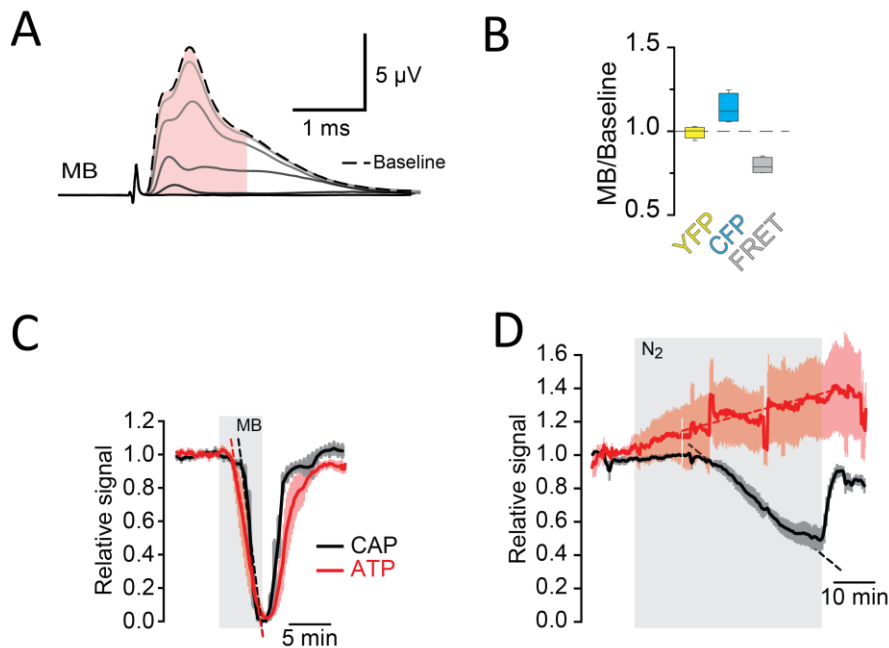


**Figure 9.** Effects of mitochondrial blockade by azide (MB) and hypoxia (N<sub>2</sub>) on axonal ATP and nerve CAP.

**(A)** Single CAP waveform obtained under control conditions (baseline, dashed line) and during application of MB (total 5 min). Single waveforms are separated by 30 s and their amplitude progressively decays during MB exposure. The shaded area indicates the range of the CAP waveform set to quantify the CAP Area for the baseline condition, the same time window was used for analysis of CAPs at subsequent time points. Under all conditions, no CAP can be elicited any longer by electrical stimulation at the end of the energy-depleting treatment. Compare waveform changes with figure 4B and 6A for data with GD and MB respectively. **(B)** Changes of the fluorescence signal, relative to baseline, during mitochondrial blockage (MB). Fluorescence intensities of the three recorded channels between 4.75 min and 5 min of incubation with MB were averaged ( $n = 4$  nerves). Compare channel intensity analysis in figure 4D and 6B for data with GD and MB respectively. In all cases, fluorescence in the CFP channel increased, while fluorescence in the FRET channel decreased. Of note, YFP emission upon direct YFP excitation remains stable in all condition. **(C)** Blockade of mitochondrial respiration by azide (MB, 5 min gray-shaded box) produces a fast decay in ATP (red) and CAP (black) starting at 1.8 min after beginning of treatment. When azide is removed, CAP and ATP are promptly restored, with CAP recovery preceding the ATP increase ( $n = 4$  nerves). **(D)** Hypoxia is produced in the optic nerve by substitution of oxygen with nitrogen (N<sub>2</sub>) in the gas-mixture

which enriches the aCSF solution as well as in the incubation chamber. The N<sub>2</sub> treatment lasts 45 min (gray-shaded box) during which a slow increase in ATP (red trace) is matched by a decrease in conduction (CAP, black trace).  $n = 4$  nerves. Black and red shaded areas adjacent to each trace represent SEM for CAP and ATP measurements, respectively. Red and black dashed, straight lines in (C) and (D) represent the maximum velocity of ATP and CAP decay (see Figure 9 for quantification).

### 3.2.3 Simultaneous glucose depletion and mitochondrial inhibition

In order to deplete the optic nerve of all its energy, we tested two different paradigms, used to simulate, in ex-vivo preparations, ischemic condition where blood supply is drastically reduced along with glucose and oxygen absence in the affected tissue. The treatment with MB + GD (prolonged to 5 min compared to 2.5 min of exposure used previously; Figure 6B-F and Figure 7) induced an immediate and fast decline of ATP, followed by an equally fast decline in CAP (Figure 10A). MB + GD had similar kinetics to MB treatment but much faster kinetics than GD, supporting the hypothesis that axonal ATP production strongly depends on mitochondrial respiration, and axonal glycolysis alone is insufficient to maintain ATP levels, even in the virtual absence of electrical activity (baseline recording conditions with 0.033 Hz stimulation frequency).

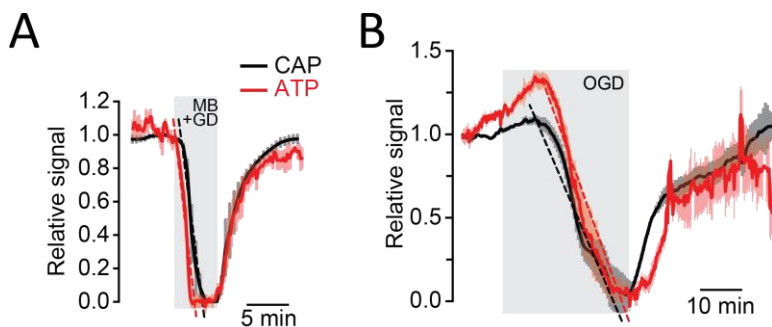


**Figure 10.** Impairment of axonal ATP and CAP during glucose deprivation and simultaneous inhibition of mitochondrial activity by azide (MB + GD) or hypoxia (OGD).

**(A)** Simultaneous removal of glucose and blockade of mitochondrial respiration with azide (MB + GD, 5 min gray-shaded box) produces a fast decay in ATP (red) preceding CAP decay (black), starting already 0.5 min after onset of treatment. Following azide removal and replenishment of glucose, CAP and ATP are restored ( $n = 4$  nerves). Red and black dashed, straight lines represent the maximum velocity of ATP and CAP decay (see Figure 9 for quantification and comparison with other conditions). **(B)** ATP and CAP are monitored during OGD treatment (simultaneous hypoxic condition lead by N<sub>2</sub> and glucose deprivation). After initial increase, both signals decay very quickly, reaching values close to zero within the 30 min OGD exposure. After the reintroduction of glucose and oxygen ATP and conduction are quickly restored.  $n = 3$  nerves. Red and black dashed straight lines in (A) and (B) represent the maximum velocity of ATP and CAP decay (see Figure 9 for quantification). Black and red shaded areas adjacent to each trace represent SEM for CAP and ATP measurements, respectively.

A second treatment that aimed at mimicking ischemic conditions is oxygen-glucose deprivation (OGD; Figure 10B), a combination of GD and hypoxia induced by nitrogen. ATP and CAP kinetics during OGD were much slower than those observed for MB + GD (Figure 10A), suggesting an incomplete blockade of mitochondrial activity by the exposure to low oxygen concentration caused by nitrogen. Interestingly, at the beginning of OGD we observed an increase in ATP signal, similar in amplitude to that observed during hypoxia in the presence of glucose (N<sub>2</sub>; Figure 9D), followed by a sudden decrease of both ATP and CAP. The decrease onset was comparable with the one observed during GD (Figure 11A) suggesting a role of glial glycogen as energy reservoir, also during OGD. Another parallelism with GD was observed for the recovery onset of ATP: following reperfusion with oxygen and glucose, the ATP signal recovery was in fact following behind the nearly instantaneous CAP recovery onset.

### 3.2.3.1 Comparison between energy-deprivation conditions in the optic nerve

With the exception of hypoxia, during all treatments, the nerve CAP waveform attenuation was similar, though with significantly different time courses for GD and OGD (Figure 8A and data not shown). Similarly, with the exception of hypoxia, for ATeam1.03<sup>YEMK</sup>, we found similar changes in fluorescence intensities in all three channels (Figure 6D, Figure 8B and Figure 9B and data not shown). By the end of GD, MB, MB + GD and OGD we observed an increase in CFP fluorescence, concomitantly with a decrease in YFP fluorescence upon donor excitation (FRET) indicating the transition of ATeam1.03<sup>YEMK</sup> to a conformation where ATP is not bound and FRET is consequently reduced. Pointing at the specificity of the effect, YFP fluorescence was found to be unchanged upon direct excitation (i.e. of the acceptor). The processed signals obtained from the integration of the evoked CAP waveform and from the normalized fluorescent intensity ratio FRET/CFP (F<sup>\*\*</sup>/C, see methods for details) were plotted against time to describe the conduction properties of the optic nerve (CAP) and the axonal ATP, respectively. We further analyzed different time courses of the ATP/CAP signals to all energy-deprivation treatments of the optic nerve. In particular, we analyzed several time-dependent parameters (decay and recovery onset, decay and recovery speed) to quantitatively describe the kinetics of the two signals during the energy deprivation models (Figure 11A-B, D-E). The total relative signal reversed after reperfusion with control aCSF was also considered (Figure 11F). From the comparative analysis it is clear that direct interference with mitochondrial OX-PHOS by

blockade of cytochrome c oxidase (complex IV) function in the electron transport chain (ETC), leads to a complete loss of ATP and CAP, which plateau at zero within a few minutes after the addition. The mechanism by which ATP and CAP were lost within such short time, seems to be independent on the presence of glucose in the media as indicated by the similar kinetics of MB and MB + GD (Figure 11A-B, D-E). The short exposure to azide lead to an almost full recovery after azide was washed out and glucose reintroduced (Figure 11F). On the opposite side, the kinetic of glucose deprivation was found to be very slow (Figure 11B,E), but eventually ATP reached values close to relative zero within the 45 minutes of aglycemia, and no CAP could be elicited. The recovery, likely due to the prolonged time course, was found to be partial (68% for CAP and 40% for ATP, Figure 11F, GD). Noteworthy, after glucose was restored in the aCSF, the CAP recovery preceded that of ATP by  $9.5 \pm 1.2$  min (Figure 11D; GD). We found a similar difference in the onset of recovery between CAP and ATP during glucose-oxygen reperfusion following OGD where ATP signal rescue followed behind that of CAP by  $7.3 \pm 1.4$  min. ATP-rescue latency might be explained by the axonal incapability of restoring the ATP pool immediately after the energy-deprivation ceased (see discussion section for further interpretation). Another notable finding was the un-expected low-impact of hypoxia as energy deprivation paradigm as indicated by a partial loss of CAP ( $56.1\% \pm 8.2\%$ ) by the end of the 45 minutes of nitrogen ( $N_2$ ) exposure, and an increase in ATP signal ( $132.7\% \pm 22.8\%$  from its baseline value). The dual response of CAP (decrease) and ATP (increase) might also be explained by the combined consequences of oxygen diffusion within the nerve and the nature of the measurements themselves. In fact, imaging samples axons at the very surface of the nerve, while CAP recordings are comprehensive of most of the fibers. These results, although apparently in contrast, might be explained by an initial surplus of oxygen which puts the optic nerve under oxidative stress.

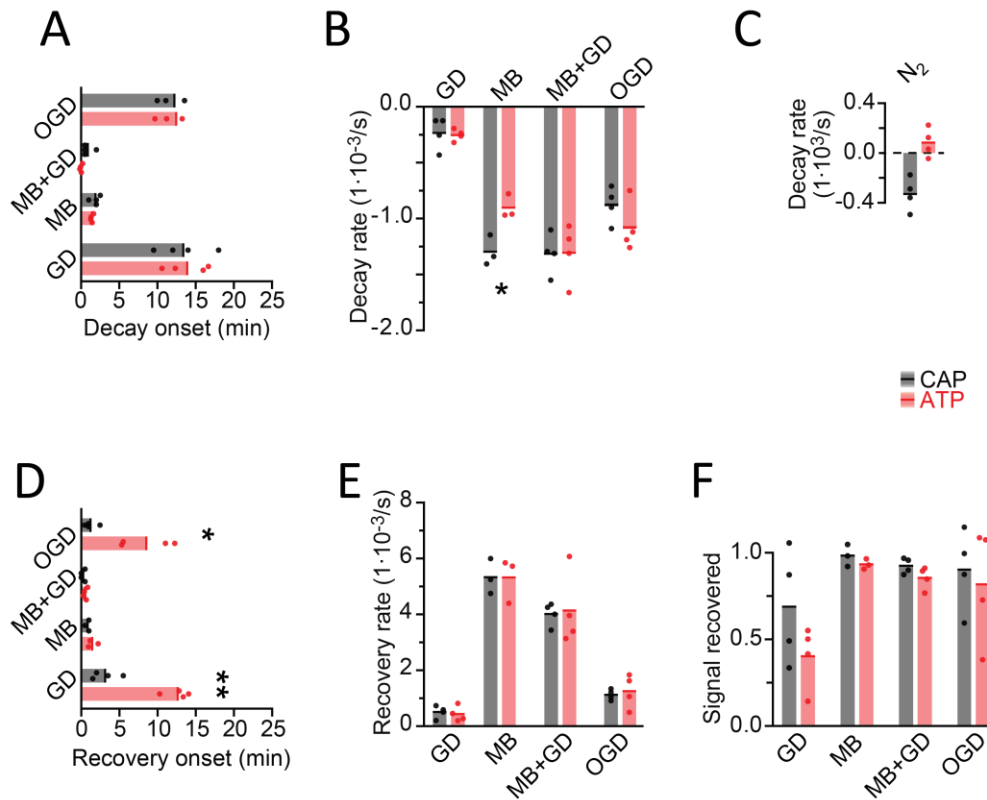


**Figure 11.** Quantification and comparison of CAP and ATP signals during all energy-failure paradigms.

Analysis includes glucose deprivation (GD), mitochondrial blockage (MB), the combination of both (MB + GD) and OGD. Hypoxia (C; N<sub>2</sub>) is considered separately for its very different effect/ kinetics. **(A)** Time of onset of the ATP and CAP decay. The slowest decay induction was observed during glucose deprivation (GD) and OGD. **(B)** Velocity of maximal signal change, after decay onset, for ATP and CAP during all treatments. **(C)** Maximal signal variation during hypoxia treatment with N<sub>2</sub>. Unlike nerve conduction (CAP), there is no loss in axonal ATP, whose signal increases over time. **(D)** Time of onset of ATP or CAP recovery after the energy-failure paradigm is ended and the optic nerves are reperfused with control aCSF containing 10 mM glucose and oxygen. **(E)** Rate of recovery of both ATP and CAP during reperfusion of the nerves with aCSF containing 10 mM glucose and oxygen after the indicated treatments. **(F)** Comparison of ATP and CAP area overall recovery after individual treatments. Data is presented as stripe plots, with dots representing individual data points, bars and lines showing the mean. Asterisks indicate statistically significant differences between ATP and CAP under the same condition (\* $p < 0.05$ , \*\* $p < 0.01$ ; one-way ANOVA with Newman-Keuls post-hoc test).

### 3.3 Electrical stimulation at high frequency

It is known that maintaining axonal conductivity *ex vivo* depends on energy-rich substrates while high frequency stimulation of axons causes CAPs to decrease (Brown et al., 2005, 2001). However, the impact of electrical activity and spiking frequency on axonal ATP levels, has never been studied.

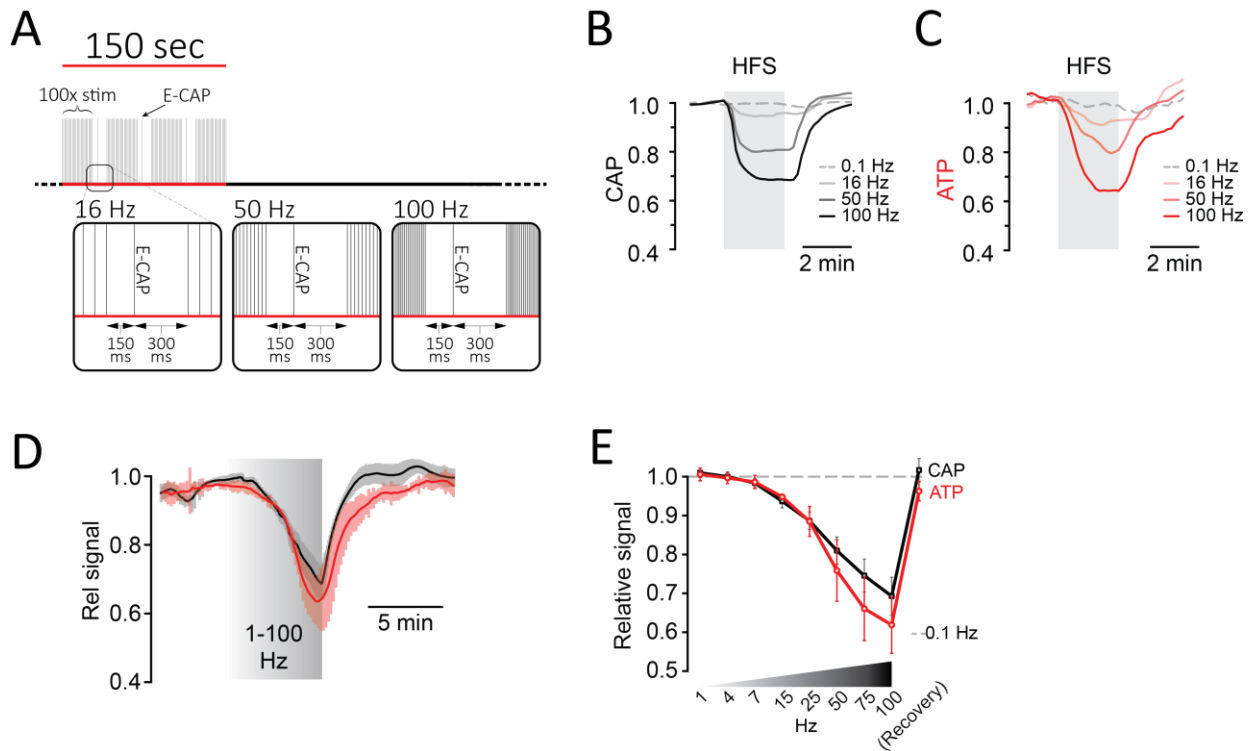


**Figure 12. Comparison of axonal ATP and nerve CAP dynamics during high frequency stimulation.**

**(A)** HFS protocol consisted in bursts of 100 stimuli at a given frequency (16, 50 and 100 Hz) with evoked CAP (E-CAP) recordings in-between. The time that divides the burst and the evoked CAP is set at 150 ms, after which 300 ms gap separates the following burst of stimuli. **(B)** The CAP area decreases over time during high frequency stimulation (HFS). The decay amplitude deviates from the absence of HFS, indicated by the dashed line (0.1 Hz, used for normalization to 1.0), and increases progressively with the increase in stimulation frequency (16 Hz, 50 Hz, 100 Hz). Traces from one representative nerve incubated in aCSF containing 10 mM glucose are shown. **(C)** Axonal ATP levels also decrease with increasing stimulation frequency, reaching a new steady state level which depends on the stimulation frequency. Same experiment as in panel B. **(D)** ATP and CAP traces of optic nerves stimulated with gradually increasing frequencies (RAMP). RAMP consists in subsequent 45 s steps of continuous stimulation at 1 and 4 Hz, followed by 6 burst-like stimulation steps at 7, 15, 25, 50, 75 and 100 Hz. RAMP stimulation produces a progressive loss of ATP and CAP followed by prompt signal recovery when the stimulation ceases. Black and red shaded areas adjacent to each trace represent SEM for CAP and ATP measurements, respectively. **(E)** RAMP single-frequency quantification of ATP (red) and CAP (black) signal amplitude (1 to 100 Hz and following recovery). The dashed line at 1.0 indicates ATP and CAP values at 0.1 Hz stimulation frequency, which are used for respective normalization. Black and red y-error bars represent SEM for CAP and ATP measurements, respectively. HFS and RAMP responses were recorded in optic nerves ( $n = 4$ ) incubated in 10 mM glucose aCSF.

The electrical stimulation provides a method to change the relative energetic demand of axons. Unlike the previously described energy failure paradigms, electrical stimulation doesn't directly interfere with axonal ATP production. Instead, it allows to experimentally manipulate its consumption by forcing the axons to quickly restore the ion gradient after the stimulus-evoked depolarization. Two different paradigms of electrical stimulation were used to study ATP dynamics:



high frequency stimulation (HFS) and continuously increasing stimulation frequencies (RAMP). HFS consisted in a series of three burst-like, fixed-high-frequency stimulations (16, 50 and 100 Hz; Figure 12A), each lasting 2.5 min, separated by 7.5 min of recovery time, i.e. low stimulation frequency, from the next train of stimuli (see method section for details). RAMP is a progressive 8-steps increase in frequency, each lasting 45-60 s, ranging from 1 to 100 Hz (see methods for details).

ThyAT optic nerves were subjected to HFS to study axonal ATP dynamics and correlate this with conduction responses. Both nerve CAP and ATP signal dropped in a stimulation frequency dependent manner (for CAP: 16 Hz:  $94.9\% \pm 1.5\%$ ; 50 Hz:  $79.6\% \pm 0.4\%$ ; 100 Hz:  $66.4\% \pm 1.0\%$ ; for ATP: 16 Hz:  $91.6\% \pm 1.0\%$ ; 50 Hz:  $82.3\% \pm 1.4\%$ ; 100 Hz:  $68.9\% \pm 2.8\%$ ;  $n = 5$  nerves; Figure 12 B-C and Figure 13A-B). The forced HFS thus produced progressive block along with slowing of conduction, likely because of the incapability of a subset of fibers to sustain the repolarization at the given stimulation. Strikingly, to the observed loss of conduction, didn't contribute the first peak of the CAP waveform which was stable even at the highest tested frequency (Figure 13A-B).

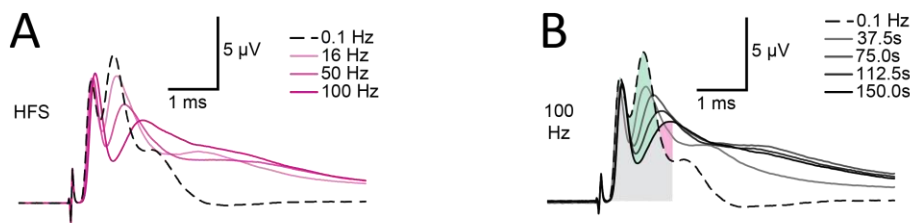


**Figure 13.** Example of progression of CAP waveform changes during high frequency stimulation (HFS).

(A) The three peaks recognizable in the baseline trace (dashed line) are differently affected by increasing stimulation frequency and for CAP analysis only the first two are considered. Shown are single traces obtained prior to stimulation (baseline) as well as at the end of a 2.5 min stimulation period at different stimulation frequencies (16 Hz, 50 Hz, 100 Hz) of a nerve incubated in aCSF containing 10 mM glucose. (B) Example of progression of CAP from baseline (dashed line) during stimulation of an optic nerve at 100 Hz incubated in ACSF containing 10 mM glucose for a total stimulation time of 2.5 min. Single traces are separated by 37.5 s. The shaded area indicates the area under the CAP wave form used for CAP quantification for the baseline condition (green) and after 150 s of HFS (red). Grey shading results from the overlay of green and red shading.

This indicates that the fast component of the CAP response can tolerate, within the tested time course, the HFS paradigm. At the same time, the loss in axonal ATP signal indicated higher ATP consumption in the fibers. Maximal ATP changes and maximal loss of conductivity correlated over stimulation frequencies (Figure 14C, magenta scatter plot/ linear regression); however, the causal relations are very likely more complex (see discussion below). Finally, both the rates of ATP decay and recovery correlated with the amplitude of ATP changes (Figure 16B, D; magenta scatter plot/ linear regression).

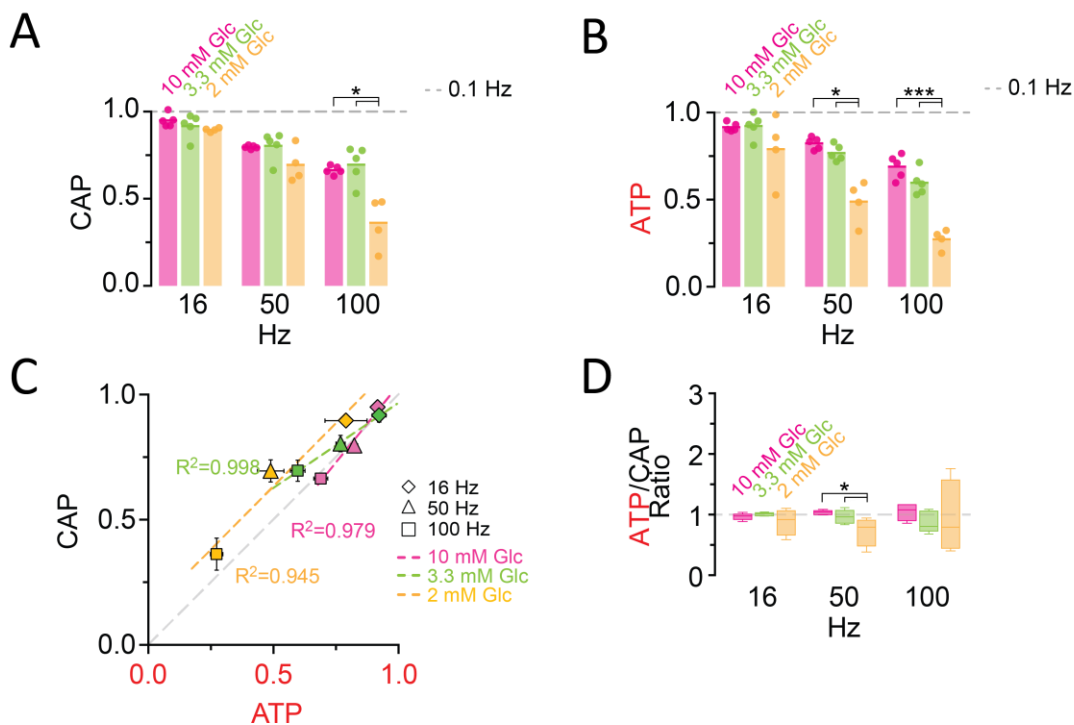


**Figure 14.** Quantification and correlation of CAP and ATP signals of optic nerve's axons stimulated at 16, 50 and 100 Hz (HFS) while supplied with different glucose concentrations (2, 3.3 and 10 mM).

(A) Remaining CAP area at the end of the HFS (overall decay amplitude) during incubation of nerves in different glucose concentrations quantified during the last 30 s of HFS. The stripe plot shows summarized data from  $n = 5, 5,$  or  $4$  nerves for 10 mM, 3.3 mM and 2 mM glucose, respectively. The dashed line at 1 shows CAP size at 0.1 Hz stimulation frequency, which was used for normalization. (B) Quantification of ATP decay amplitude during incubation of the same nerves as in (A) in different glucose concentrations. The dashed line at 1 shows ATP levels at 0.1 Hz stimulation frequency. (C) Correlation of the amplitude of ATP and CAP decay during HFS of nerves bathed in aCSF containing the glucose concentrations indicated. Data points are very close to the diagonal of the graph indicating that ATP and CAP change by similar factors. (D) Ratio of ATP and CAP drop during HFS in the presence of glucose in the concentrations indicated. If both parameters change by the same factor, this ratio remains equal to one. Data in (A-B) is presented as stripe plots, with dots representing individual data points and bars and lines showing the mean. Asterisks in (A-B) and (D) indicate statistically significant differences between glucose concentrations (\* $p < 0.05$ , \*\*\* $p < 0.001$ ; Welch's t-test).

Next, we asked whether lower physiological glucose concentrations have an impact on nerve conduction and axonal ATP levels when nerves are challenged with different spiking frequencies (HFS, Figure 14, 16). In presence of 10 mM and 3.3 mM glucose, CAP performance and ATP levels dropped similarly with increasing stimulation frequencies. However, when only 2 mM glucose were applied, both CAP and ATP levels were substantially decreased (Figure 14; yellow graphs), resulting in a very variable ATP/CAP ratio (Figure 14D). CAP waveforms were also significantly altered by low glucose with each peak being strongly reduced at the end of the HFS (2 mM vs 3.3 and 10 mM; Figure 15A-C). Single channels were also analyzed since these show the specific effect of ATP loss at each glucose condition. The largest divergence between donor and acceptor fluorescence was seen for 2 mM glucose (Figure 15D-F).

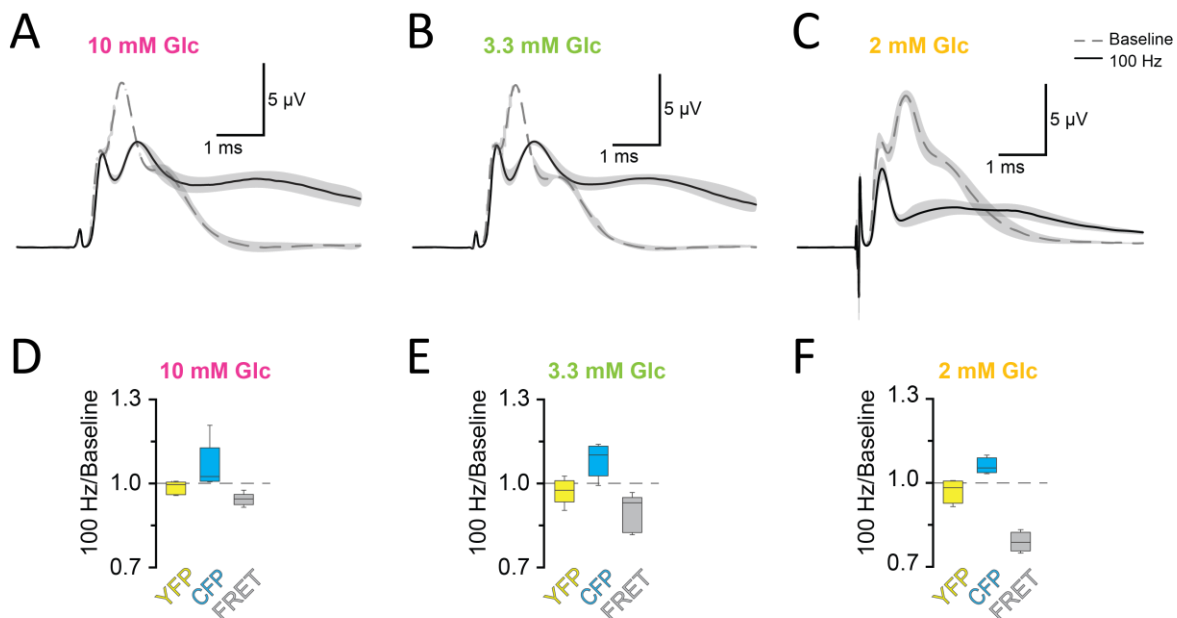


**Figure 15.** Example of CAP waveforms' and ATP sensor fluorescence intensities' changes during high frequency stimulation (HFS) of optic nerves incubated with aCSF containing different glucose concentrations.

Shown are mean CAP waveforms ( $n = 3$  nerves for each condition) incubated in ACSF containing 10 mM glucose (A), 3.3 mM glucose (B) and 2 mM glucose (C) prior to high frequency stimulation ("baseline"; dashed lines) or at the end of the 2.5 min HFS (100 Hz) period (solid lines). Grey areas indicate SEM. (D-F) Changes of the fluorescence signal at the end of the 2.5 min HFS (100 Hz) period relative to the baseline signal prior to stimulation of optic nerves incubated in ACSF containing 10 mM glucose (D), 3.3 mM glucose (E) and 2 mM glucose (F). During HFS, fluorescence in the CFP channel increased, while fluorescence in the FRET channel decreased. Of note, YFP emission upon direct YFP excitation remains stable.  $n = 5, 5, 4$  optic nerves for 10 mM, 3.3 mM and 2 mM glucose respectively.

This data suggests that 2 mM glucose is insufficient to keep viable ATP steady-states and a proper nerve conduction under the challenge of HFS in our ex vivo experimental settings. Further evidence of the sub-threshold provision of substrate, represented by 2 mM glucose condition, is given by its slower recovery rate following the cessation of HFS, when compared to axonal ATP recovery at higher glucose concentrations (0.21% ± 0.01% vs 0.40% ± 0.09% signal/s respectively for 2 mM glucose and for the averaged recovery rate at higher glucose concentrations, Figure 16D, yellow scatter plot/ linear regression). Remarkably, we found that after HFS cessation, both axonal ATP and CAP recovery rates increased with the increase in frequency stimulation and the amplitude of signal loss, indicating the presence of adaptive mechanisms (see discussion 4.3).

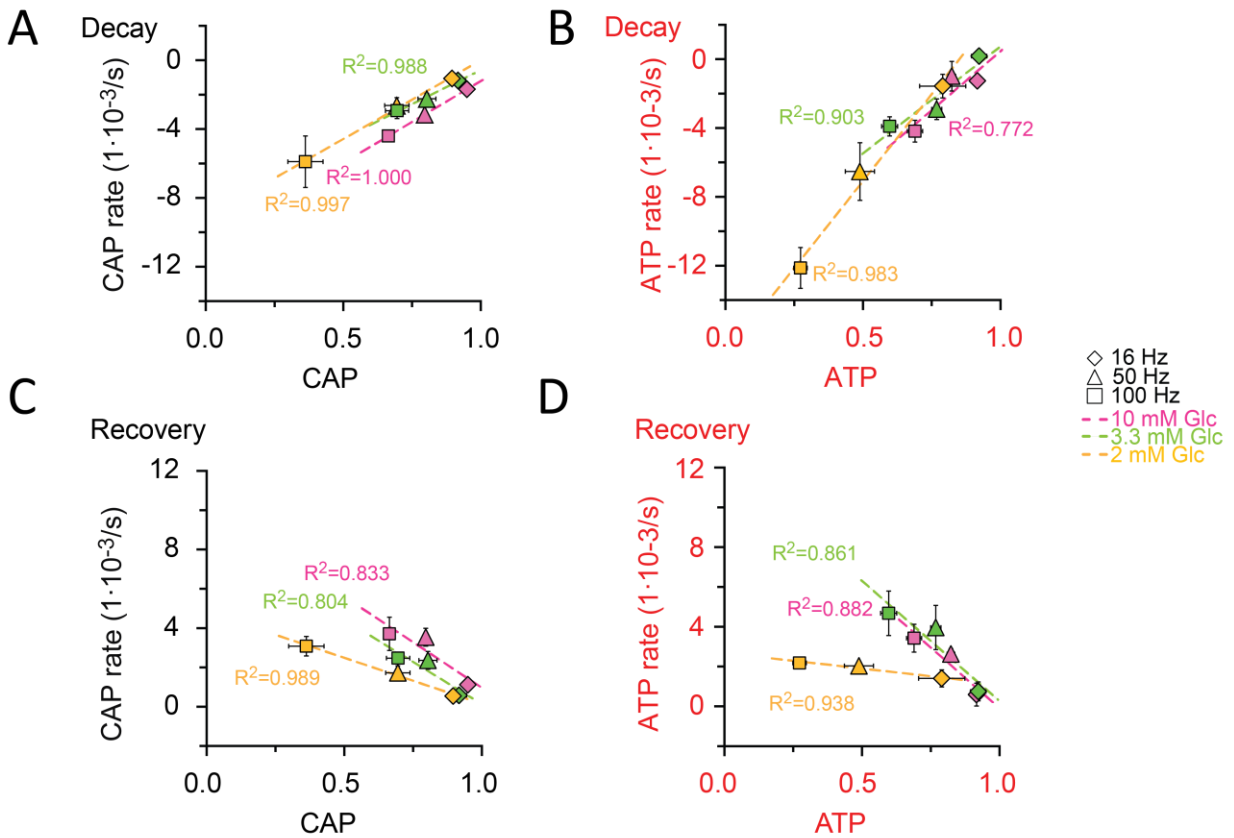


**Figure 16. Correlation of the rates and amplitudes of CAP and ATP changes during HFS in different glucose concentrations.** (A) Correlation of the velocity of the initial decay of CAP at the beginning of HFS and the amplitude of CAP decay at the end of HFS. The faster the CAP drops, the larger the CAP amplitude is. (B) Same analysis for ATP as for CAP area in panel A: the faster ATP consumption at the beginning of HFS correlates with a larger decrease in ATP signal amplitude. (C) Correlation between rates of CAP area recovery and the amplitudes of CAP changes after the cessation of stimulation, for different glucose concentrations. The velocity of CAP recovery increases with larger amplitude of CAP decay during stimulation. (D) Same analysis as in C for ATP: ATP recovery rates are strongly depending on the amplitude of ATP decrease during HFS at 10 mM and 3.3 mM glucose, but much less in the presence of 2 mM glucose. The graph summarizes data from n = 5, 4, or 4 nerves for 10 mM, 3.3 mM and 2 mM glucose, respectively.

We also investigated how substrates other than glucose can act as the sole extracellular energy source for catabolic pathways downstream of glycolysis. It has been previously shown how lactate and pyruvate can maintain conduction, in the same manner as glucose, within 2 hours of continuous perfusion at baseline stimulation (Brown et al., 2001). We tested optic nerves with high frequency stimulation while providing glucose, lactate or pyruvate (each at 10 mM concentration) under aerobic conditions. We found optic nerve conduction was maintained equally well with all the substrates (Figure 17), in agreement with the earlier findings (Brown et al., 2001), Presumably because absolute axonal ATP consumption is likely unaffected by the type of metabolic support.

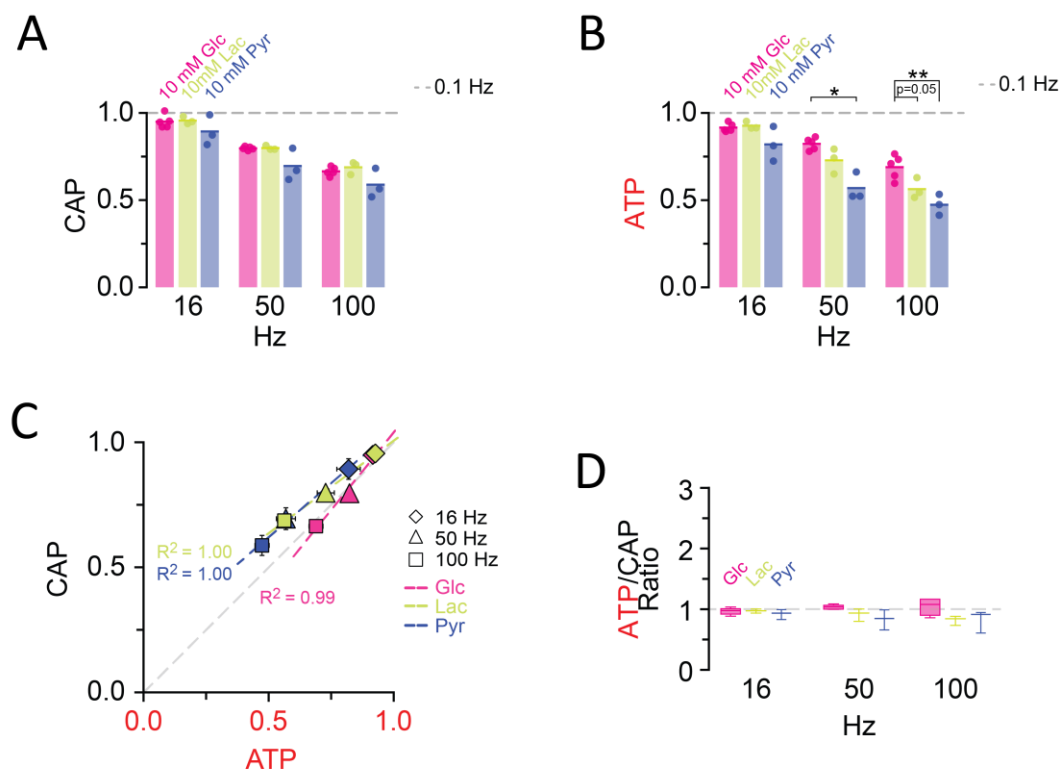


**Figure 17.** Comparison between glucose, lactate and pyruvate as exogenous energy substrates shows energy metabolism of axons is better maintained in the presence of glucose at higher frequencies.

(A) The comparison between CAP area decay of optic nerves incubated in aCSF containing 10 mM glucose ( $n = 5$  nerves) versus optic nerves incubated either in 10 mM lactate or 10 mM pyruvate ( $n = 3$  nerves) during HFS, shows no significant differences among the three substrates in maintaining the conduction ( $p > 0.05$ , Welch's t test). (B) By contrast, analysis of axonal ATP levels indicates that at higher frequencies glucose is a better substrate to maintain axonal ATP. Same experiments described in panel A. (C) Correlation of ATP and CAP decay amplitude during HFS of nerves bathed in aCSF containing glucose, lactate or pyruvate (each 10 mM) as energy substrates. (D) ATP to CAP amplitude ratio, calculated for nerves bathed in aCSF containing lactate (10 mM) or pyruvate (10 mM) as energy substrates during HFS. The ratio remains almost equal to one for all conditions supporting the concept that both ATP and CAP change by a similar factor.  $n = 5, 3, 3$  for glucose, lactate and pyruvate, respectively.

Asterisks in B indicate significant differences among conditions: \* $p < 0.05$ , \*\* $p < 0.01$ , \*\*\* $p < 0.001$ ; Welch's t test.

However, at the highest frequency 100 Hz, the relative decrease in axonal ATP levels was larger with lactate (or pyruvate) than with glucose (glucose:  $68.9\% \pm 2.8\%$ ; lactate:  $56.3\% \pm 2.8\%$ ; pyruvate:  $47.4\% \pm 2.8\%$ ;  $p = 0.05$  and  $p = 0.01$ , respectively;  $n = 3$  nerves; Figure 17B), showing that glucose maintains axonal ATP production better than lactate or pyruvate, at equimolar exogenous concentrations. Noteworthy, the linear 1:1 correlation for the observed changes in ATP and CAP parameters at increasing frequencies is maintained also for pyruvate and lactate.

### **3.4 CAG-GO-ATeam optic nerves: ATP and CAP responses to energy deprivation and comparison with ThyAT**

In collaboration with Akiyo Natsubori at Keio University (Tokyo), optic nerves from CAG-GO-ATeam mice were analyzed. Transgenic mice were generated in Japan by targeting the genetically encoded GO-ATeam ATP sensor, under the CAG promoter, to the ROSA-26 locus (Natsubori et al., unpublished). The mice were transported to the Max Planck Institute for Experimental Medicine for analysis and in-deep characterization of the GO-ATeam sensor during different WM energy deprivation paradigms. GO-ATeam is a red-shifted version of the original ATeam1.03: GO-ATeam carries a green (cp173-mEGFP) and orange (mKO $\kappa$ ) FPs as donor and acceptor, respectively (Nakano et al., 2011). CAG-GO-ATeam mice were expected to express the red shifted ATP sensor in most cells and axons; however, only sparse labeling expression was observed in LSM z-stack analysis (Figure 18B-D). The optic nerves were initially challenged with RAMP stimulation frequencies (1-100 Hz, total 7.8 min in 3.3 mM glucose aCSF) and ATP was monitored as previously described (Figure 6) after excitation and emission channels were adjusted to GO-ATeam (Figure 18A; see methods for more details). ATP was found to decay of about 15% after the max frequency (Figure 18E, RAMP - 100 Hz) was applied. However, during RAMP stimulation the amplitude of CAP decay was similar to that described for ThyAT. During 35 min of glucose deprivation (GD) ATP decayed sooner than CAP and reached a plateau after 80% of decay was reached (Figure 18F). This plateau at the end of GD was observed also in ThyAT optic nerves where, in contrast, the amplitude of ATP signal decay was nearly complete (plateauing at about 5%; Figure 8C).

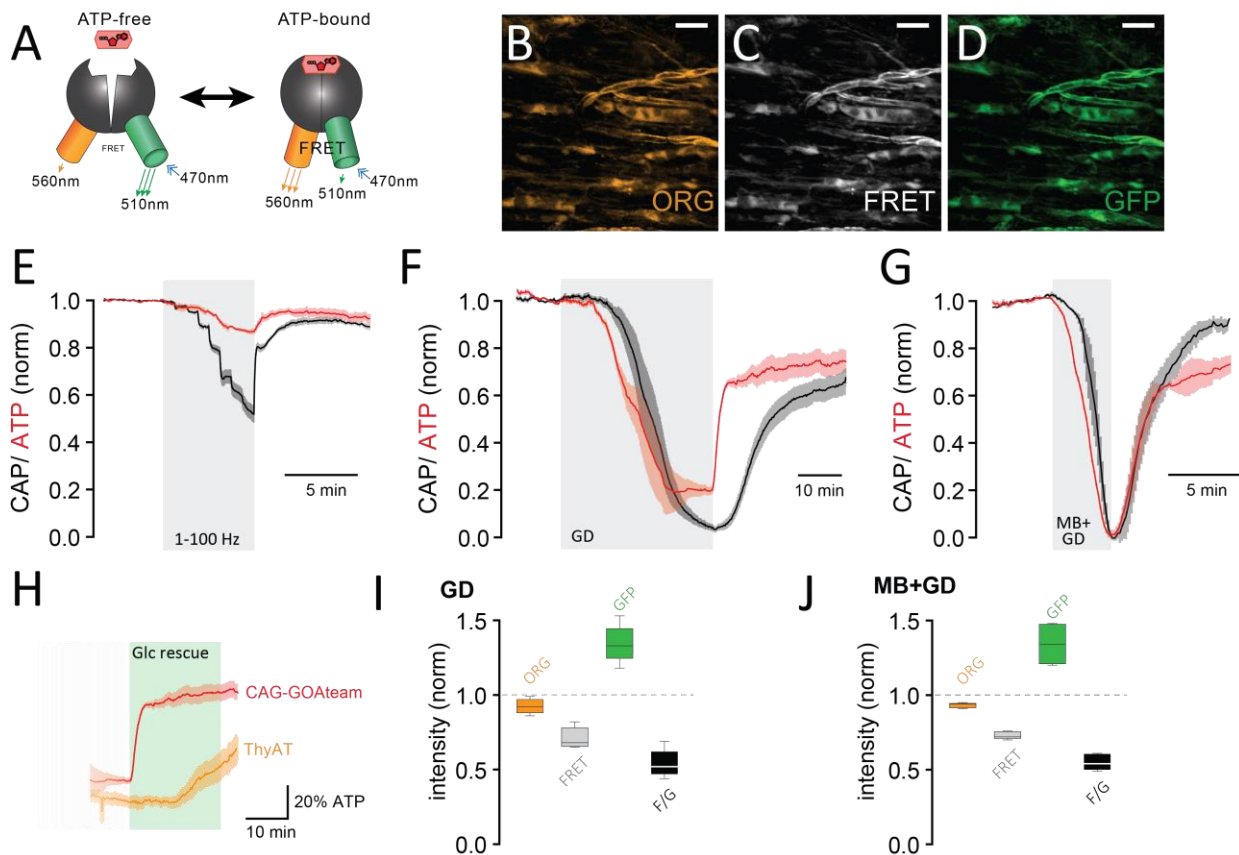


**Figure 18. CAG-GO-ATeam responses to energy deprivation paradigms**

(A) GO-ATeam is a red-shifted version of ATeam1.03 carrying a green donor (cp173-EGFP) and orange acceptor (mKO<sub>k</sub>) for FRET. Excitation and emission maxima are shown for both FPs. (B), (D) GO-ATeam is expressed under the CAG promoter in mice, leading to multiple cell type labelling in the optic nerve, as shown by 20  $\mu$ m z-projection in the three channels: ORG (orange, (B)) as result of excitation at 543 nm and emission at  $590 \pm 25$  nm; FRET (C) with excitation at 488 nm and emission at  $590 \pm 25$  nm; GFP as result of excitation at 488 nm and emission at  $525 \pm 25$  nm. (E) CAG-GO-ATeam optic nerves subjected to RAMP stimulation (7.8 min, 8 step frequencies between 1 and 100 HZ): CAP signal decay was similar to that observed in ThyAT optic nerves but ATP decay was barely visible compared to the large response observed in ThyAT optic nerves. (F) CAG-GO-ATeam optic nerves exposed to glucose deprivation (GD, 35 min) showed a similar time-course for CAP than ThyAT; ATP decay anticipated CAP's, plateau at 20% and its rescue was instantaneous after glucose was reintroduced (panel (H) for comparison between CAG-GO-ATeam and ThyAT). (G) Short exposure to MB +GD (4 min) induced a quick and transient loss in ATP and CAP in CAG-GO-ATeam optic nerves. (H) Comparison between CAG-GO-ATeam and axonal ThyAT ATP responses after glucose reperfusion (following 45 and 35 min glucose deprivation respectively): the rescue was instantaneous and preceded CAP's, in CAG-GO-ATeam optic nerves; the opposite situation is described in ThyAT optic nerves. (I) box plot of fluorescent signal change from baseline within the last 15 s of GD treatment: mKO<sub>k</sub> acceptor fluorescence decreased only as specific FRET effect (ORG vs FRET indicating ATP loss) while GFP donor fluorescence increased as result of decreased FRET efficiency (i.e. ATP loss), the ratio between FRET and Green fluorescence is calculated as F/G. (J) Box plot analysis of fluorescence signal change from baseline within the last 15 s of MB+GD treatment: ATP loss caused the same FP and ratio responses observed in (I). Scale bar in (B-D): 20  $\mu$ m.

ATP also recovered immediately as soon as glucose was restored: this instantaneous rescue preceded that of CAP and was not observed in ThyAT under similar treatment (Figure 8C; GD, 45

min). This instantaneous ATP rescue in CAG-GO-A<sub>Team</sub> optic nerves originates non-specifically from all cell types and could indicate a higher ATP demand or a reduced glycolytic capacity in axons, if compared to the delayed ATP rescue described for the axonal-specific ATP signal (ThyAT, Figure 18H) (see discussion 4.3). Moreover, MB+GD treatment successfully induced ATP and CAP loss in CAG-GO-A<sub>Team</sub> optic nerves with ATP decay slightly anticipating CAP's (Figure 18G; MB+GD, 4 min). The specificity of the FRET effect was observed in single-channel fluorescence intensity analysis for GD and MB+GD treatments (Figure 18I and 18G, respectively) similarly for the reported FRET effect observed in ThyAT optic nerves (Figure 6C-D and Figure 8B).

### 3.5 Ketogenic diet impact on B-Hydroxybutyrate metabolism in the optic nerve

Another substrate that can fuel mitochondrial TCA/OX-PHOS in the optic nerves is diacetic acid. Under physiological conditions, diacetic acid exists as its conjugate base acetoacetate which is normally produced in the liver starting from acetoacetyl-CoA and released into the bloodstream. Acetoacetate is the second ketone body circulating the bloodstream in terms of concentration, after  $\beta$ -hydroxybutyrate ( $\beta$ -HB), also produced in the liver. The interconversion of  $\beta$ -HB and acetoacetate is catalyzed by 3-hydroxybutyrate dehydrogenase and requires  $\text{NAD}^+$ /  $\text{NADH}$ . In the brain, the mitochondrial enzyme SCOT activates acetoacetate to acetoacetyl-CoA, by adding one -CoA group, acetoacetyl-CoA can finally be broken down by a thiolase enzyme into two molecules of acetyl-CoA that fuel the TCA cycle and generate ATP.

We tested acetoacetate under HFS and monitored ATP and CAP dynamics of the nerve. Surprisingly, in presence of 20 mM acetoacetate in the aCSF, the nerve was unable to maintain ATP and conduction even during the lowest stimulation frequency (16 Hz, Figure 19A) and no recovery was observed. We hypothesized that, under normal circumstances, the carbohydrate-enriched diet of the mice leads to poor systemic production of ketone bodies. These are then likely inefficiently absorbed and catabolized by CNS and white matter tracts to generate energy. Therefore, to push the CNS tissue to metabolically adapt to ketone bodies oxidation, we treated the mice for 4 weeks with a ketogenic diet (KD) after overnight starvation. We monitored ketone levels in the blood once a week and by the end of the 4-weeks KD treated mice showed increased levels of  $\beta$ -hydroxybutyrate



( $\beta$ -HB; Figure 19B), likely as a consequence of the  $\beta$ -oxidation in high amounts of fatty acids and acetyl-CoA production.

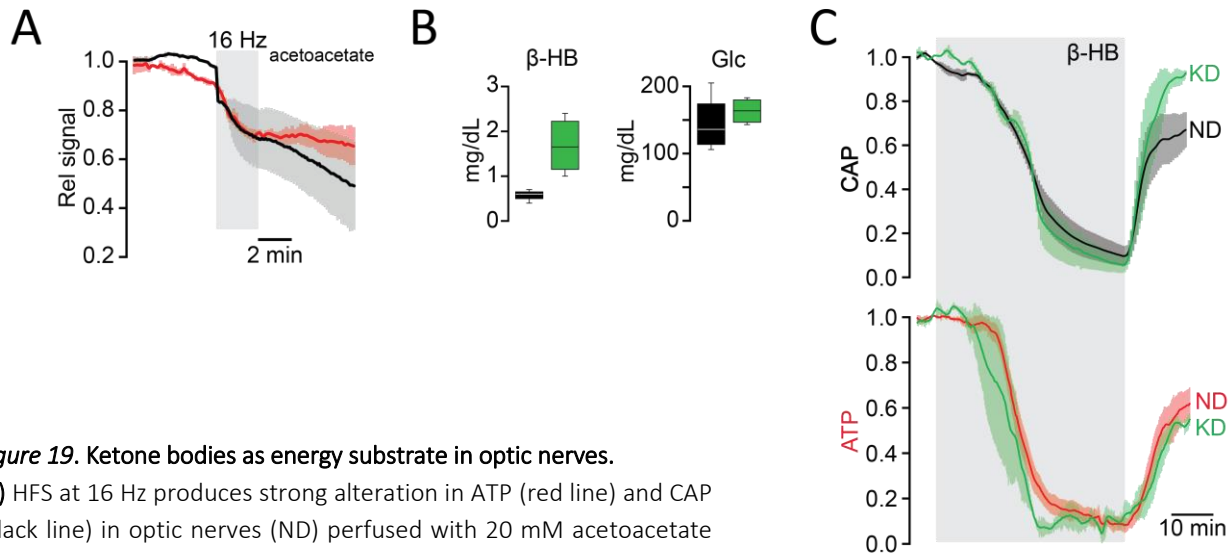


**Figure 19. Ketone bodies as energy substrate in optic nerves.**

**(A)** HFS at 16 Hz produces strong alteration in ATP (red line) and CAP (black line) in optic nerves (ND) perfused with 20 mM acetoacetate which is leading to recovery failure after the cessation of the stimulus.

**(B)** ThyAT mice were treated for 4 weeks with KD (high-fat diet) and glucose and ketone ( $\beta$ -hydroxybutyrate,  $\beta$ -HB) were monitored:

blood levels of glucose and  $\beta$ -HB at the end of the KD (green boxplot) and normal diet (ND, black boxplot).  $\beta$ -HB levels were enhanced in KD-treated mice **(C)** optic nerves were isolated and exposed to aCSF containing 20 mM  $\beta$ -HB as well as  $\alpha$ -glucosidase I and II (glycogen-degradation) blockers 1,4-Dideoxy-1,4-imino-D-arabinitol (20  $\mu$ M, DAB) and 1-Deoxynojirimycin (20  $\mu$ M, DNJ). CAP and ATP were monitored during the 45 min exposure to  $\beta$ -HB supplied aCSF, showing similar decay-kinetics to glucose deprivation (fig. 5), however recovery was more prompt than GD and CAP recovery was almost complete in optic nerves from KD-treated mice.  $n = 4$  nerves (ND, black and red traces for CAP and ATP respectively),  $n = 2$  nerves (KD, green traces).

We proceeded to test our hypothesis of a beneficial effect of ketogenic diet on white matter capability of processing ketone-bodies for energy production. Optic nerves from KD and normal diet fed (controls, ND) mice were isolated and superfused with aCSF containing only 20 mM  $\beta$ -HB for 45 min.  $\beta$ -HB was used instead of acetoacetate to maintain the continuity with the most abundant ketone body found in the blood ( $\beta$ -HB is on average  $2.0 \pm 0.5$  fold more abundant than acetoacetate in the blood; Tanda, Hinokio, Washio, Takahashi, & Koseki, 2014). Optic nerve CAP and axonal ATP were tracked using baseline stimulation at 0.1 Hz during baseline (glucose/  $\beta$ -HB),  $\beta$ -HB only and recovery (glucose/  $\beta$ -HB). To avoid glycogenolysis from glial stores, which may have been affected in KD treated mice, we supplied all the aCSF solutions with  $\alpha$ -glucosidase I and II (glycogen breakdown) inhibitors. No overall differences were observed between KD and ND treated optic

nerves during the 45 min exposure to  $\beta$ -HB (Figure 19C and Figure 20A-B). Conversely, after glucose was re-introduced in the aCSF, optic nerve CAPs from KD treated mice showed an enhanced recovery ( $91.2 \pm 2.8\%$  vs  $65.4\% \pm 8.7\%$  of ND condition; Figure 20C). This result was not surprising since previous evidences suggests the ketogenic diet to have neuroprotective effects under different insults and disorders (reviewed by Prins, 2008). Nevertheless, given the low number of nerves tested ( $n = 4$ ,  $n = 2$  respectively for ND and KD conditions), conclusions should be taken with caution.

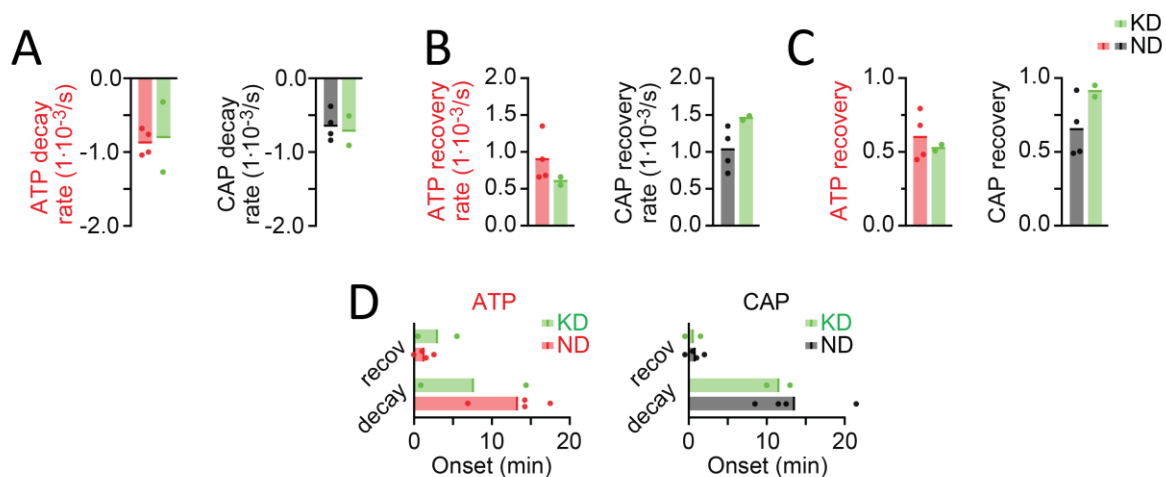


**Figure 20. Quantification of CAP and ATP signals during the different phases of  $\beta$ -hydroxybutyrate exposure in KD treated mice.**

(A) ATP and CAP in optic nerves from KD and ND treated mice show similar relative decays after the perfusion with 20 mM  $\beta$ -HB. (B) ATP and CAP signals in optic nerves from KD and ND during recovery after  $\beta$ -HB is substituted with glucose. (C) Quantification of the overall recovery of ATP and CAP signals after reperfusion with 10 mM glucose. (D) Time (min) of decay and recovery onset.  $n = 4$  nerves (ND, black and red traces for CAP and ATP respectively),  $n = 2$  nerves (KD, green traces).

### 3.6 Lactate metabolism in white matter

Following the systematic screening of substrates and concentrations that can be used by axons of the optic nerve to generate energy and maintain conduction, we aimed at understanding whether these axons require a pyruvate/lactate metabolism also in presence of glucose as the only energy substrate available. To address this question, we monitored optic nerves conduction and axonal ATP levels while pharmacologically interfering with endogenous lactate metabolism. To serve this purpose we supplemented low-glucose (3.3 mM) aCSF with D-lactate and AR-C155858. D-lactate is the optical isomer of its metabolizable form L-lactate and competes with it at the MCT transport site.

In addition, D-lactate interferes with lactate dehydrogenase (LDH) activity. AR-C155858 is a selective MCT1/ MCT2 blocker (Ovens, Davies, Wilson, Murray, & Halestrap, 2010).

At the highest frequency, D-lactate slightly reduced CAPs (20 mM, Figure 21A) but had a significantly stronger effect on axonal ATP (at 100 Hz: Glc:  $57.6\% \pm 2.0\%$ ; Glc + D-Lac:  $31.8\% \pm 0.5\%$ ;  $p = 0.009$ ;  $n = 3$  nerves; Figure 21B).

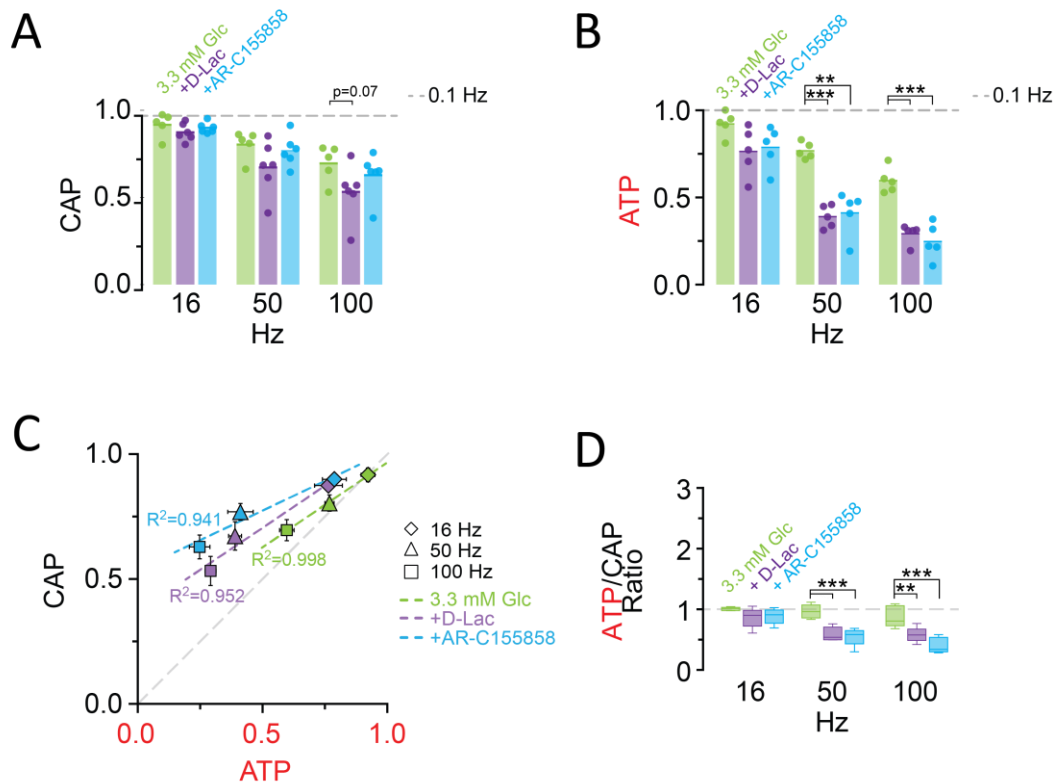


**Figure 21. Endogenous production of lactate from glucose in the optic nerve is essential to maintain ATP during HFS.**

(A) In the presence of glucose (3.3 mM;  $n = 5$  nerves) as exogenous energy substrate, inhibition of lactate metabolism by D-lactate (20 mM; competitive inhibitor of endogenous L-lactate metabolism at MCTs and LDH,  $n = 6$ ) or AR-C155858 (10  $\mu$ M; MCT1 and MCT2 selective inhibitor,  $n = 6$ ) does not significantly affect CAPs. (B) Analysis of ATP under the same conditions as in (A): ATP levels undergo a strong decrease at higher frequencies in the presence of D-lactate or AR-C155858. ( $n = 5$  nerves for all conditions). The dashed lines in panels A-B at 1 show CAP size or ATP levels at 0.1 Hz stimulation frequency used for normalization. (C) Inhibition of metabolism of endogenously produced L-lactate in the presence of glucose as the sole exogenous energy substrate shifts the correlation of ATP and CAP to the upper left showing that ATP changes more strongly than CAP. (D) The ratio of ATP and CAP drop decreases significantly in the presence of inhibitors of lactate metabolism, confirming that ATP changes more strongly than CAP.

Asterisks in (A-B and D) indicate significant differences among conditions: \* $p < 0.05$ , \*\* $p < 0.01$ , \*\*\* $p < 0.001$ ; Welch's t test.

Similarly, when MCT1/MCT2-mediated lactate transport was inhibited using the specific inhibitor AR-C155858, relative axonal ATP levels were strongly affected (10  $\mu$ M, at 100 Hz: 25.2%  $\pm$  2.7%;  $p = 0.004$ ;  $n = 3$  nerves), but with little effect on CAP performance (at 100 Hz: Glc = 76.4%  $\pm$  1.3%; Glc + AR-C155858 = 68.5%  $\pm$  2.2%;  $p = 0.06$ ;  $n = 3$  nerves; Figure 21A-B) as indicated also by the respective CAP waveforms (Figure 22). ATP/CAP ratios strongly deviated from the 1:1 ratio observed in the presence of glucose alone when lactate metabolism was impaired (Figure 21C-D). Collectively, these results strengthen the conclusion that generation of pyruvate/lactate is required by spiking axons of white matter to fuel ATP production.

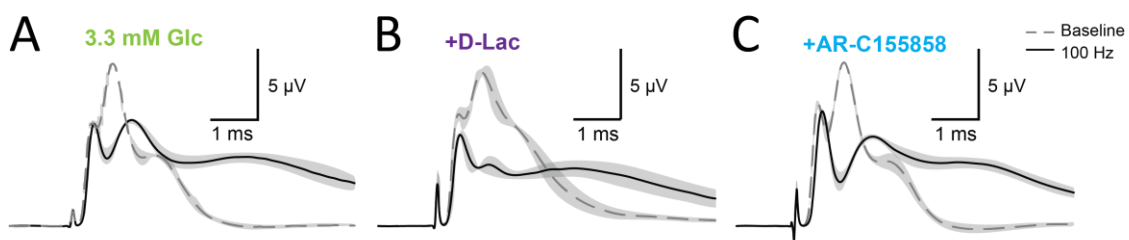


**Figure 22.** Example of CAP traces before and after high frequency stimulation (HFS) of optic nerves in the presence of inhibitors of lactate metabolism.

Optic nerves were incubated in ACSF containing 3.3 mM glucose in the absence of inhibitors (A) or in the presence of either 20 mM D-lactate (B) or 10  $\mu$ M AR-C155858 (C). Shown are mean CAP waveforms ( $n = 3$  nerves for each condition) prior to high frequency stimulation (“baseline”; dashed lines) or at the end of the 2.5 min HFS (100 Hz) period (solid lines). Grey areas indicate SEM.

### 3.7 ATP and CAP monitoring in *Slc16A1*<sup>het</sup> optic nerves

The direct impact of the oxidative production of lactate and pyruvate on axonal ATP homeostasis but not on conduction, as demonstrated by MCT/LDH inhibition during HFS, encouraged us to study the role of glial MCT1 in vivo. We crossbred ThyAT animals with the amyotrophic lateral sclerosis (ALS) murine model *Slc16A1*<sup>het</sup>. MCT1 is the most abundant pyruvate/lactate transporter in CNS, expressed in oligodendroglia and localized in non-compact myelin (Rinholm et al., 2011). *Slc16A1*<sup>het</sup> mice develop axonopathy at advanced age (Lee et al., 2012), with similar features as Plp1<sup>KO</sup> mice. In order to compare with ATP/CAP dynamics under MCT/LDH pharmacological inhibition, we tested optic nerves from ThyAT- *Slc16A1*<sup>het</sup> mice in similar experimental conditions.

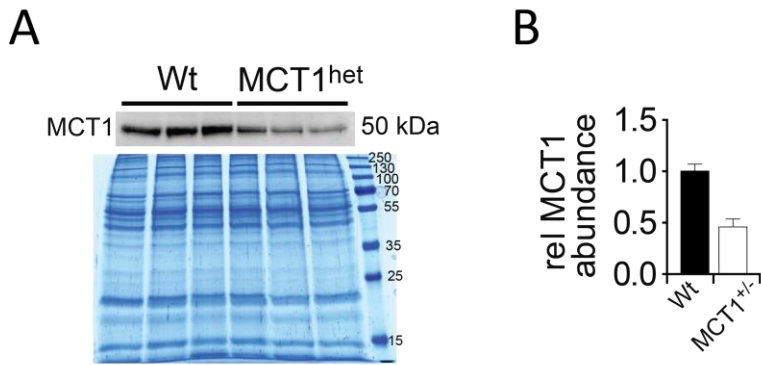


**Figure 23. Analysis of ATP and CAP during HFS in optic nerves from MCT1<sup>+/-</sup> mice.**

**(A)** Western blot of optic nerve lysates showing a reduced expression of MCT1 in *Slc16A1<sup>het</sup>* (MCT1<sup>het</sup>) mice. Coomassie staining is displayed as control. **(B)** Quantification reveals that optic nerves of MCT1<sup>het</sup> mice contain 46% ± 11% of MCT1 of wild type littermate controls (n = 5 each for wild type and heterozygous optic nerves). Data in this figure was kindly provided by Dr. Kathrin Kusch.

The nerves were in fact superfused with 3.3 mM glucose (and subsequently to 6.6 mM lactate) while challenged to trains of 16, 50 and 100 Hz stimulations (HFS). We observed only a non-significant trend towards reduced ATP levels in the optic nerves from ThyAT-*Slc16A1<sup>het</sup>* mice under the 2.5 min of stimulation (Figure 24). We concluded that a reduced MCT1-expression of 46% ± 11% (Figure 23) and the corresponding reduction of oligodendroglial lactate export capacity do not significantly impact on axonal energy metabolism, in the short term of HFS, as much as a probably more complete blockade of lactate metabolism provided by pharmacological inhibition of MCTs/LDH. Young *Slc16A1<sup>het</sup>* mice could also have compensatory mechanisms to bypass the reduced capability of shuttling lactate/pyruvate into the axonal compartment (see discussion 4.3).

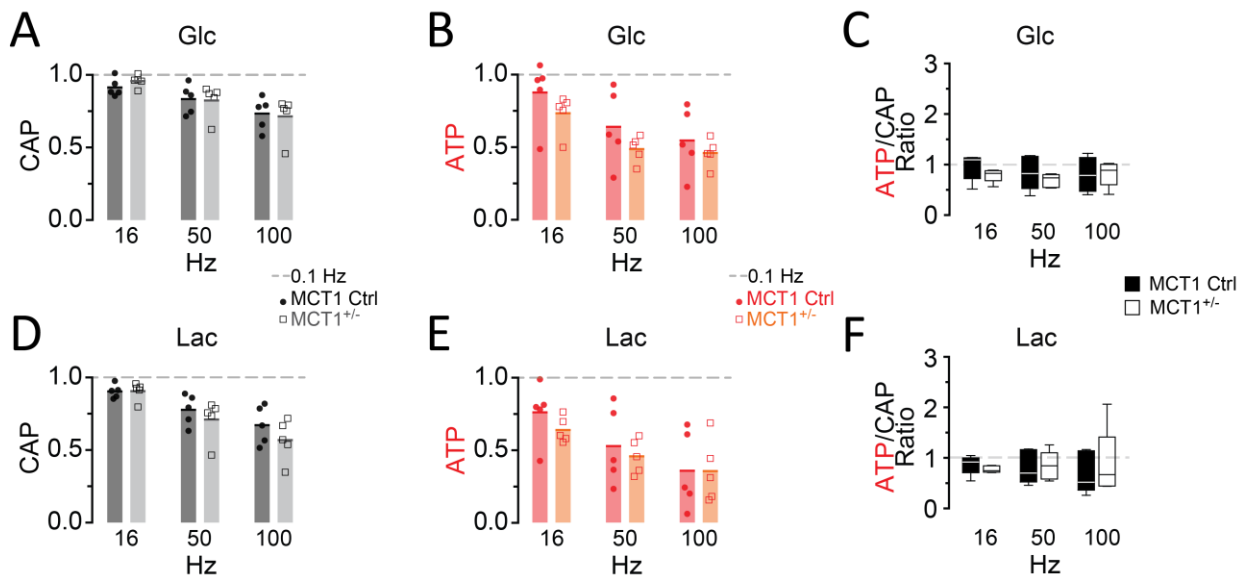


**Figure 24.** Analysis of ATP and CAP during HFS in optic nerves from 10 weeks old MCT1<sup>+/-</sup> mice.

(A), (B) No statistically significant difference of both CAP and ATP changes are observed between wild type and MCT1-heterozygous optic nerves incubated in 3.3mM glucose. (D), (E) No ATP or CAP significant difference is observed between MCT1<sup>het</sup> optic nerves and controls superfused with 6.6 mM lactate. The ATP/CAP ratio does not differ significantly between wild type and MCT1-heterozygous mice both in glucose (C) and lactate (F).  $n = 5$  for wild type and heterozygous mice,  $p > 0.05$ ; Welch's t-test.

### 3.8 ATP and CAP monitoring in PLP1<sup>KO</sup> optic nerves

Since electrical activity at high frequencies poses a metabolic challenge to myelinated nerves, the combined monitoring of axonal conductivity and energy metabolism should help understanding how the disease affects axonal integrity. X-linked spastic paraplegia type-2 (SPG2) is a human neurological disorder, caused by the null mutation of *PLP1*, an oligodendrocyte-specific gene (Schiffmann and Boespflug-Tanguy, 2001) which codes for the homonym protein and a smaller peptide DM20. In patients, progressive axonal loss in long myelinated tracts of the spinal cord is unexplained, but is recapitulated in Plp1<sup>KO</sup> mice (Boison & Stoffel, 1994; Klugmann et al., 1997), a bona fide SPG2 model (Griffiths et al., 1998; Edgar et al., 2004). Mice lacking PLP/DM20 show secondary molecular changes, among these the absence of SIRT2 (Werner et al., 2007) present in the non-compact myelin and potential axonal NAD<sup>+</sup>/NADH sensor (Gruenenfelder, Thomson, Penderis, & Edgar, 2011). Lack of SIRT2 might represent the first hint of a link between SPG2 and an impaired axo-glia metabolism.

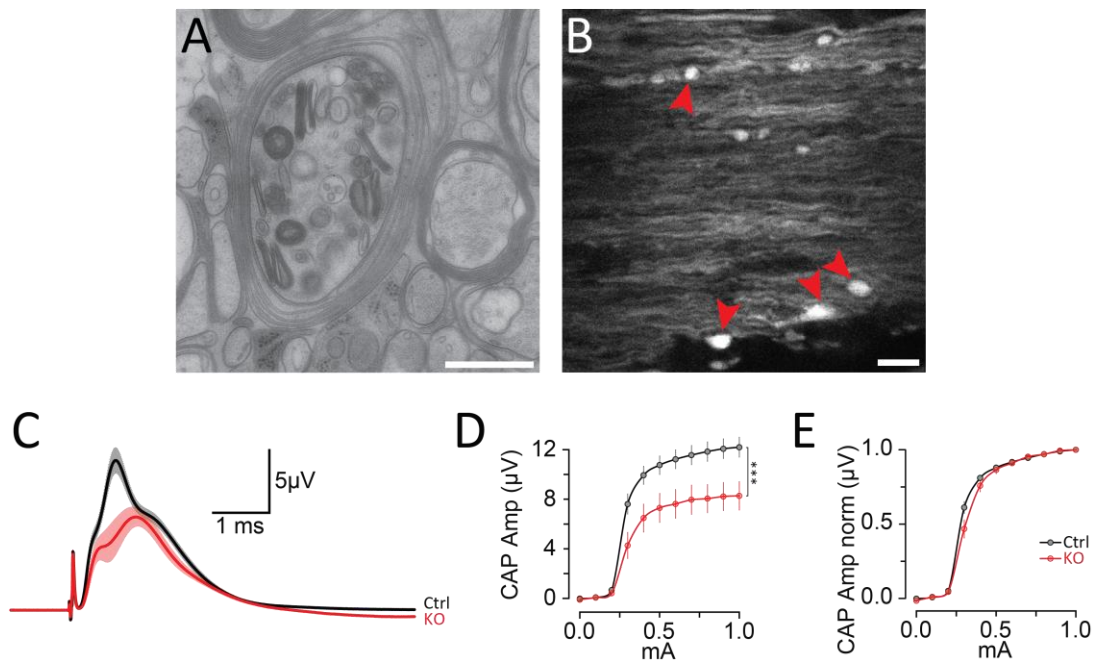


**Figure 25.** Optic nerves prepared from PLP<sup>KO</sup> mice, model of spastic paraplegia type-2, show axonal impairment at 10 weeks of age.

(A) Electron microscopic image of a high-pressure frozen optic nerve of a 10 week old PLP<sup>KO</sup> animal showing axonal swellings and accumulation of transported vesicles at the node of Ranvier. Scale bar: 0.5 $\mu$ m. The image was kindly provided by Dr. Wiebke Möbius. (B) Confocal image of an acutely recorded optic nerve from a ThyAT x PLP<sup>KO</sup>- mouse clearly showing axonal swellings (red arrowheads). Shown is the YFP channel of the ATP-sensor. Scale bar: 10  $\mu$ m. (C) Evoked response after supramaximal stimulation: CAP waveforms from PLP<sup>KO</sup> (red trace) and PLP<sup>CTRL</sup> (black trace) are shown. (D) Intensity-voltage plots from PLP<sup>KO</sup> and PLP<sup>CTRL</sup> optic nerves indicate an overall loss of conduction ( $32.2 \pm 9.8\%$ ). (E) Normalized intensity-voltage plots show no significant change in the excitability of the responding axons in PLP<sup>KO</sup>. Optic nerves from 10 weeks old animal were used (n = 5 for panel C-E).

Moreover, given the prominent role of oligodendrocytes in contributing directly to axonal energy metabolism (Funfschilling et al., 2012; Lee et al., 2012), we asked whether SPG2 mice exhibit an underlying defect of axonal ATP homeostasis contributing to a later axonal degeneration. As expected, CNS myelination of PLP<sup>KO</sup> mice appeared grossly normal (not shown), while by electron microscopy of myelinated axons the local accumulation of cargo within axons could be observed (I. Griffiths, 1998) (Figure 25A). These occasional axon swellings were also observed by acute confocal imaging of the axoplasmic ATP-sensor (Figure 25B).

Optic nerves from PLP<sup>KO</sup>-ThyAT mice were functionally challenged ex vivo by electrical stimulation using HFS and RAMP (Figure 25C-F and Figure 26C, respectively) and glucose deprivation (Figure 26D). During HFS both ATP levels and CAPs decreased more strongly in Plp1 mutant nerves

(PLP<sup>KO</sup>) than in wildtype controls, both in the presence of glucose and lactate as exogenous energy substrate (ATP levels at 50 Hz were reduced to 68.1% ± 2.7% and 52.1% ± 3.6% in Plp<sup>wt</sup> and Plp<sup>KO</sup> with glucose, and to 66.9% ± 5.2% and 39.0% ± 5.9% in Plp<sup>wt</sup> and Plp<sup>KO</sup> with lactate,  $p < 0.05$ ;  $n = 3$  and 4 nerves for Plp<sup>wt</sup> and Plp<sup>KO</sup>; Figure 26A-B). Interestingly, no significant difference of ATP levels was observed during stimulation at the highest frequency suggesting that a lower limit of ATP had been reached (Figure 26A-B).

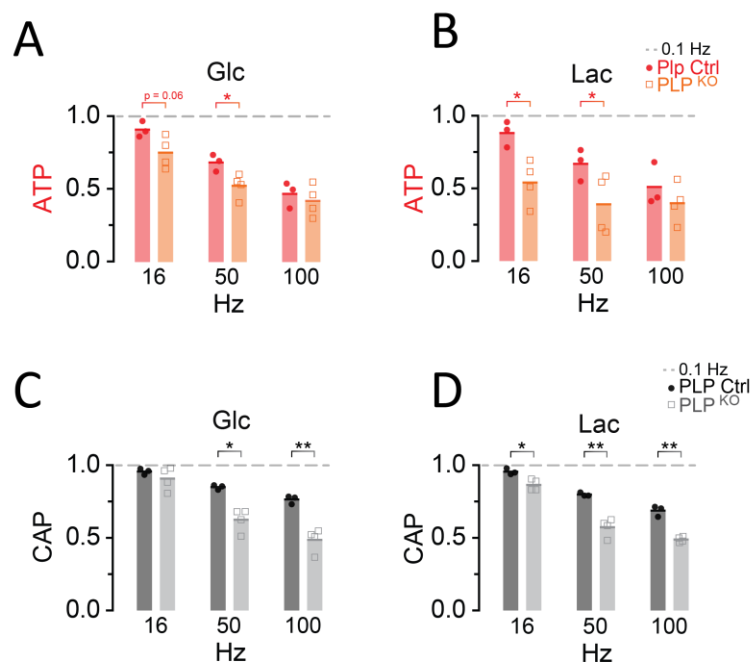


**Figure 26.** ATP and CAP responses in PLP<sup>KO</sup> optic nerves subjected to high frequency stimulation (HFS) with glucose or lactate as main substrate.

(A),(B) Comparison of the remaining ATP at the end of HFS, between PLP<sup>KO</sup> and Ctrl optic nerves incubated in aCSF containing 3.3mM glucose (A) and 10 mM lactate (B);  $n = 3$  for each genotype. (C), (D) Comparison of the remaining CAP at the end of HFS, between PLP<sup>KO</sup> and PLP<sup>Ctrl</sup> optic nerves incubated in aCSF containing 3.3 mM glucose (C) or 10mM lactate (D);  $n = 3$  for each genotype.

The dashed lines in panels C-F at 1.0 show CAP size or ATP levels at 0.1Hz stimulation frequency. Asterisks in C-F indicate statistically significant differences as indicated (\* $p < 0.05$ , \*\* $p < 0.01$ , \*\*\* $p < 0.001$ ; Welch's t-test).

Optic nerves from 10 weeks old animal were used;  $n = 3$  optic nerves per genotype. Error bars indicate SEM.

Using the same experimental conditions and 3.3 mM glucose as substrate, optic nerves from Plp1<sup>KO</sup>-ThyAT were also tested during RAMP stimulation (Figure 27). RAMP stimulation lasted for 7.8 min and covered 8 steps frequencies from 1 to 100 Hz. ATP measurement showed variability in optic nerves from Plp<sup>KO</sup>, and at the end of the stimulation no significant difference was found (Figure 27A



and 27B; ATP at the end of the RAMP stimulation was reduced to  $63.0\% \pm 3.2\%$  and  $74.9\% \pm 10.0\%$  in  $Plp^{wt}$  and  $Plp^{KO}$ ). CAP measurements were more consistent between conditions showing a prominent loss of conduction in  $Plp^{KO}$  ( $14.7\% \pm 4.3\%$  of remaining CAP) in comparison to  $Plp^{wt}$  ( $42.6\% \pm 1.9\%$  of CAP signal remaining at the end of the RAMP; Figure 27, bottom panels). The ATP and CAP signal rate change calculated for each given frequency reflected the overall decay, indicating 25 Hz as the frequency at which the CAP signal started diverging between  $Plp^{KO}$  and controls (Figure 27B bottom panel).

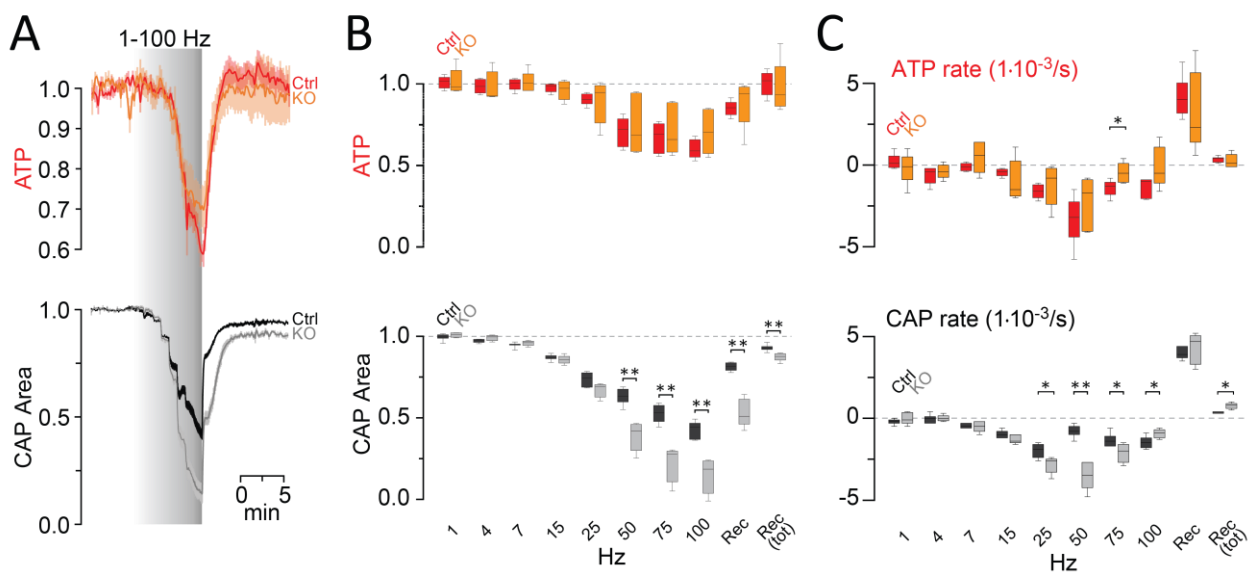


**Figure 27. Quantification of ATP and CAP signals in PLP<sup>KO</sup> optic nerves subjected to increasing frequency stimulation (RAMP, 1-100 Hz).**

(A) In presence of 3.3 mM glucose in the circulating aCSF, ATP (on top) and CAP (on bottom) responses to RAMP stimulation of PLP<sup>KO</sup> axons (orange/gray respectively for ATP and CAP) compared to control axons (red/black), show conduction blocks arising at higher frequencies in PLP<sup>KO</sup> axons but no significant difference in ATP kinetics.

(B) ATP (top) and CAP (bottom) signals in PLP<sup>wt</sup> (dark gray boxplot for CAP and red for ATP) and PLP<sup>KO</sup> (light gray boxplot for CAP and orange for ATP) were evaluated during the last 15 s of RAMP (maximum stimulation at 100 Hz) giving the total signal decayed during this stimulation paradigm. (C) Rates of ATP (top) and CAP (bottom) decay is calculated at each stimulation frequency.

Significant differences between genotypes are indicated by the asterisks as indicated (\* $p < 0.05$ , \*\* $p < 0.01$ , \*\*\* $p < 0.001$ ; Welch's t-test).

To better understand the white matter metabolic state of  $Plp^{KO}$ , optic nerves were finally exposed to glucose deprivation. Under GD the axonal demand for ATP is not altered by frequent depolarization however the lack of substrates' supply likely interferes with its constant production. During exposure to GD, axonal ATP and CAP decayed simultaneously. However, the velocity of decay

of ATP in Plp1<sup>KO</sup> optic nerves was significantly reduced in comparison to controls. Moreover, ATP recovery after glucose reperfusion was found to be significantly greater in Plp<sup>KO</sup> than Plp<sup>wt</sup> axons ( $p = 0.0079$ ,  $86.1\% \pm 1.5\%$  and  $60.67\% \pm 1.9\%$ , respectively; Figure 28A and 28C upper panel). ATP and CAP were also found to decay with significantly slower kinetics in Plp1<sup>KO</sup> optic nerves (Figure 28A and 28B) but the conduction was then restored with similar rate and extent in both genotypes after glucose reintroduction (Figure 28C lower panel).

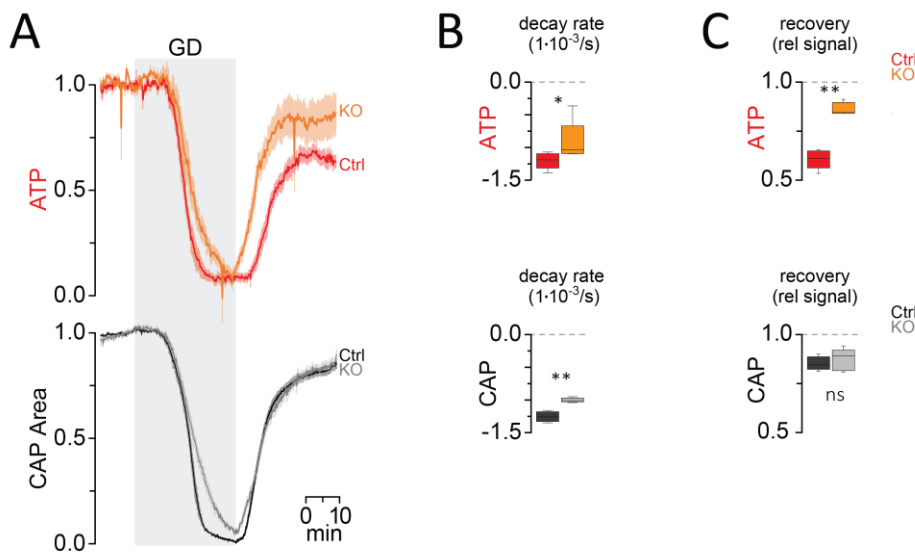


**Figure 28.** Quantification of ATP and CAP signals in PLP<sup>KO</sup> optic nerves subjected to glucose deprivation (GD).

(A) The calculated rate of signal decay following glucose deprivation shows ATP (top) and CAP (bottom) signals decaying slower in PLP<sup>KO</sup> axons than controls and an improved ATP overall recovered signal in PLP<sup>KO</sup> (orange trace) after glucose is reintroduced in the aCSF. (B) The maximal rates of signal decay is calculated during GD for ATP (top) and CAP (bottom) for PLP<sup>KO</sup> (orange/gray) and controls (red/black). (C) The maximal rates of signal recovery following glucose reperfusion is calculated for ATP (top) and CAP (bottom) for PLP<sup>KO</sup> (orange/gray) and controls (red/black).

Significant differences between genotypes are indicated by the asterisks as indicated (\* $p < 0.05$ , \*\*  $p < 0.01$ , \*\*\*  $p < 0.001$ ; Welch's t-test).

Maintaining the ex vivo optic nerve perfectly stable under the objective during combined confocal imaging and electrophysiology could be challenging in. However, we could smooth eventual noise and compensate for small drifts along each imaging axis by averaging channel intensities of entire frames. By doing so, we obviously average ATP transients and CAP recordings in potentially metabolically different fibers. The results provide an averaged response of all tens of thousands fibers that compose the optic nerve, clamped between the suction electrodes (Figure 6A). However, we noticed while calculating the ratiometric images of the baseline condition (with normal glucose and oxygen supply) large caliber fibers had higher ratios compared to smaller fibers (Figure 6E). Consequently, the approximation represented by averaging intensities from entire frames blurs possible different ATP responses belonging to these different populations of fibers. Consequently, we aimed to retrieve this information and cluster the analysis according to fiber diameter.

The relevance of fiber diameter can be seen in *Slc16A1<sup>het</sup>* mice, where small caliber fibers seem to pay the price of a reduced expression of the monocarboxylate transporter-1 (Lee et al., 2012). To cluster the analysis of PLP<sup>KO</sup> ATP responses to RAMP and GD according to fiber size, we developed an ImageJ macro to discriminate fiber size according to intensity. The criteria is based on the assumption that larger fibers contains a higher amount of ATeam1.03<sup>YEMK</sup> fluorescent molecules. After X-Y registration, the script applies a threshold to the images. The thresholded stacks (mask) are then used to generate ROIs (see methods and appendix §2 for details). With this method we could create two categories based on the fiber diameter: large fibers (identified by ROIs with diameter  $\geq 1.5 \mu\text{m}$ ,  $2.2 \pm 0.4 \mu\text{m}$  on average) and small fibers (all fibers where ROIs didn't satisfy the criteria of diameter  $\geq 1.5 \mu\text{m}$ ). Thus the ThyAT-PLP<sup>KO</sup> imaging dataset was re-analyzed (Figure 29). The analysis showed that the previously detected increase in recovery following GD and glucose reperfusion was mainly present in PLP<sup>KO</sup> small caliber fibers (Figure 29A, blue trace) and large caliber fibers didn't account for this recovery-boost (Figure 29B). During GD, all PLP<sup>KO</sup> caliber fibers showed a quicker recovery, anticipating that of PLP<sup>wt</sup> axons. During RAMP stimulation it is shown how ATP in small fibers is depleted more rapidly and to a larger extent than in large fibers (circa 20% difference; Figure 29C-D). However no major difference was noticed between genotypes during this stimulation paradigm (Figure 29C-D, blue and orange traces).

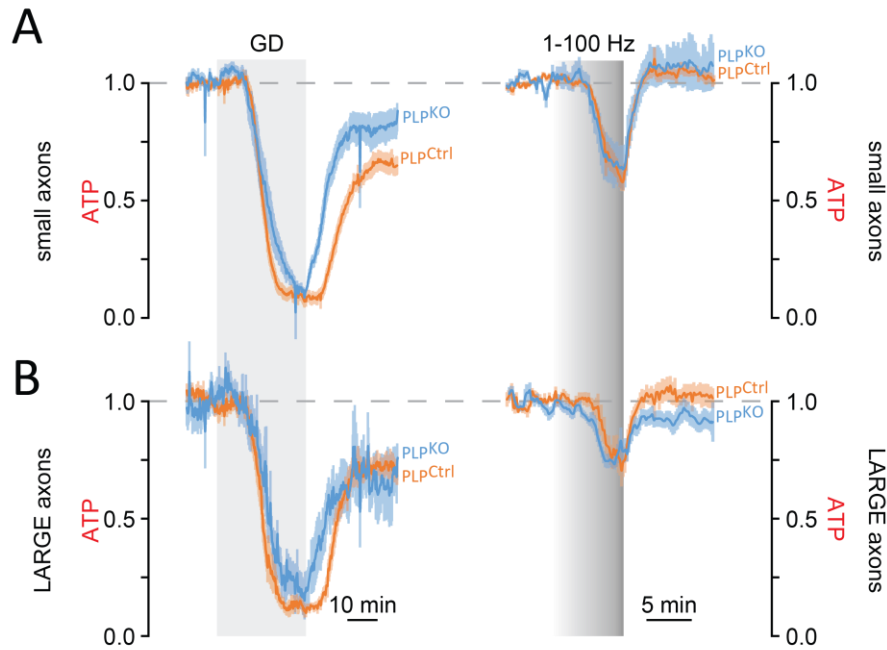


**Figure 29.** Further analysis of ATP in  $PLP^{KO}$  optic nerves subjected to RAMP/GD, using a FIJI-macro to separate ATeam1.03<sup>YEMK</sup> fluorescence in large and small fibers.

(A), (B) Exposure to glucose deprivation of  $PLP^{KO}$  optic nerves produces similar ATP decays in small (A) and large caliber axons (B). Recovered signal is enhanced, regardless of size, in all  $PLP^{KO}$  fibers but max overall recovery is greater only in small caliber  $PLP^{KO}$  fibers, while appears similar between knockouts and controls in large axons (B, blue and orange traces). (C), (D) RAMP stimulation produces larger decays in small axons (C) than in large ones (D), no differences between genotypes could be observed. Dataset analyzed here is the same of figure 27.

These findings demonstrate that in PLP-deficient mice, during transient GD, axonal ATP can be better maintained, probably as a result of compensatory mechanisms (see discussion 4.4). On the other hand, electrical stimulation, which directly impact on ATP consumption, shows no relevant differences in ATP steady states among genotypes. Conversely, the strong incapability of  $PLP^{KO}$  stimulated axons to maintain conduction might be explained by a structural defect rather than a metabolic impairment, not detected during a long exposure to substrate deprivation.

### 3.9 Spinal cord in-vivo imaging

Ex-vivo preparations preserve tissue organization and cell-cell connectivity, thereby representing extremely useful tools to investigate CNS metabolism and support. In addition, genetically encoded FRET-based reporters provide the necessary temporal and spatial resolution to resolve metabolite dynamics in a living system. We have combined two aspects to specifically study white matter energy metabolism and metabolic support mechanisms in the context of electrical stimulation by isolating optic nerves from transgenic ATP-reporter mice. Isolated optic nerves are kept in defined conditions where most experimental parameters are under the experimenter's control (e.g. temperature, amount of substrate, stimulation frequency, etc.). However, in these artificial conditions CNS metabolic states are likely very different from the in vivo scenario. Furthermore, long-term experiments are restricted to the viability time of the acute ex-vivo preparation (< 24 hours for optic nerves). Thus, fundamental questions that require long term observations (e.g. "what is the metabolic impact of myelin ensheathing on axons?") cannot be addressed in such system. To test in vivo relevance of our previous findings and to continue deepening in the still poorly understood territory of white matter metabolism we designed a strategy to study myelinated tracts in vivo in transgenic mice as well as in mice in which target cells are transfected via adeno-associated viruses (AAVs).

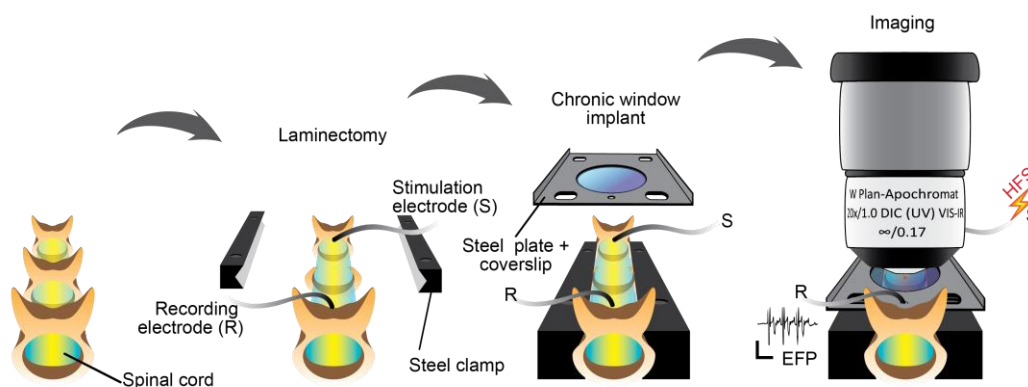


**Figure 30.** Laminectomy and chronic window implant in the spinal cord of a transgenic mouse.

Illustration of chronic window implant following removal of the lamina of the 12<sup>th</sup> thoracic vertebra (Laminectomy); Vertebrae T11 to L1 give support and are fixed by flanking steel clamps. A top plate is positioned along with tungsten electrodes for evoked CAP recordings. The window is sealed after the space between the CNS tissue and the top 5 mm circular coverslip is filled with transparent silicone. The skin is sutured and the implant stabilized with acrylic, providing a chronic window implant for repetitive imaging and recording.

Most of CNS white matter tracts run deeply into the tissue with few exceptions, therefore, we decided to focus the study on the spinal cord (SC) where projecting axons form ascending (sensory) pathways run on the top side of the SC tubular formation. These fibers compose the somatosensory dorsal column-medial lemniscus tract, which contains the axons of the primary somatosensory neurons whose cell soma is found in the dorsal root ganglia. We access this formation by surgically removing the lamina of the 12<sup>th</sup> thoracic vertebra (T12 laminectomy, Figure 30).

The vertebrae T11 to T13 were held together by steel clamps providing support for a steel top-plate. The steel implant carries a 5 mm coverslip on the top-side thereby providing a stable chronic window for repetitive imaging (Figure 30, see methods 6.14, and Farrar et al., 2012; Farrar & Schaffer 2014). The implant was successfully installed in ThyAT transgenic mice, without electrodes, to limit the time of surgery for imaging-only purpose. Imaging was carried at 5 days post-operative by acquiring 32  $\mu\text{m}$  z-stacks at 2  $\mu\text{m}$  step intervals. The z-stack max projection showed the in-vivo fluorescence of ATeam1.03<sup>YEMK</sup> in the ascending fibers of the fasciculus gracilis (Figure 31).

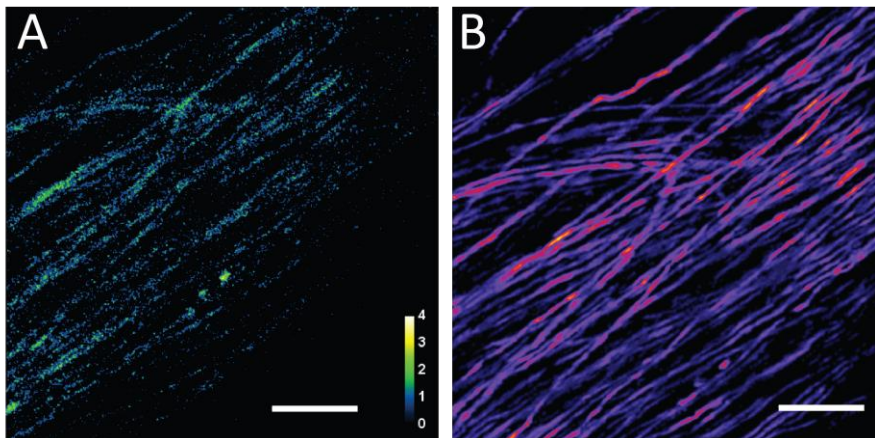


**Figure 31.** In vivo imaging of ThyAT spinal cord axons of the fasciculus gracilis (T12) using a chronic window.

**(A)** TCSPC-FLIM imaging of the Ateam1.03<sup>YEMK</sup> in axons of transgenic ThyAT mice. The averaged value measured for  $T_{a-w}$  is  $2.295 \pm 0.008$  ns. **(B)** Z-stack max projection of 30  $\mu\text{m}$  section of in-vivo spinal cord axons expressing ATeam1.03<sup>YEMK</sup>. Scale bars: 50  $\mu\text{m}$

## 4 Discussion

ATP is likely the principal molecule in energy metabolism, produced or consumed in virtually every metabolic pathway. For a long time, ATP analysis was performed using biochemical assays (using e.g. hexokinase enzymatic assay or firefly-luciferase), providing accurate estimates of ATP concentration but since these require cell/tissue lysate it was limited to poor cell-specificity, and poor spatial and temporal resolution. The emergence of genetically-encoded sensors for ATP quantification and the development of imaging techniques overcame these limitations, providing cell specificity along with high resolution both in time and space. Several genetically-encoded ATP sensors have been described and used in different studies to estimate the cytosolic ATP-concentration around 1-4 mM (Pathak et al., 2015; Rangaraju et al., 2014), well within the linear range of the ATP sensor used in this study.

This thesis aimed at understanding white matter metabolism and glial energy support contribution, by simultaneously monitoring axonal ATP and CAP recordings as functional readout of axonal integrity. This work focuses on optic nerve as white matter model, using an acute ex-vivo preparation. Despite missing one important parameter in metabolism, i.e. the active blood flow, this preparation has the considerable advantage of allowing precise control over other parameters, such as pH, temperature, substrates and electrical stimulation, which are fundamental in metabolism and not accessible in vivo. Moreover, unlike in-vitro systems, ex-vivo preparation offers the further advantage of preserving CNS structures: this conserved integrity is key to understanding the mechanisms of a functional cell-cell interaction. Thus, for the first time to our knowledge, we monitored optic nerve CAP and axonal ATP dynamics with very accurate spatial and temporal resolution, by taking advantage of neuronal (axonal) expression of the genetically encoded FRET sensor for ATP, ATeam1.03<sup>YEMK</sup> (Imamura et al., 2009), in a transgenic mouse line (ThyAT; Trevisiol et al., 2017). Having CAP and ATP as a readout for white matter energy metabolism, we manipulated the conditions in which the optic nerve was kept (e.g. firing rate, substrates, pharmacological inhibitors, etc.) to understand glial cell contribution in terms of metabolic support to axonal function. Following a precise characterization of the ATeam1.03<sup>YEMK</sup> expression in the CNS and a proof-of-principle experiment of transient axonal energy loss, we studied I) single metabolic pathway inhibition, II) effects of key substrates (e.g. glucose, lactate, ketone bodies, etc.) in maintaining energy production in white matter, III) effects of HFS on energy consumption, IV) white matter metabolic

responses of optic nerve from a mouse model of spastic paraplegia type 2 (HSP or SPG2, i.e. spastic gait gene 2) under stress condition, V) ThyAT expression in spinal cord axons in vivo, as tool for repetitive ATP-monitoring during long time periods.

The following key findings were thus provided by this thesis: I) axonal ATP changes often correlate with CAP, decaying in a stimulation-frequency dependent manner; II) lactate metabolism contributes to ATP homeostasis in the presence of glucose as the exogenous energy substrate; III) recovery rates of ATP after cessation of HFS positively correlate with amplitudes of ATP decrease, suggesting short term adaptations of metabolism to match ATP demand; IV) no major difference in maintaining energy production is observed between substrates like glucose, lactate and pyruvate, even under HFS; V) although ketone bodies, as sole energy substrate, are unable to maintain energy production in any condition, ketogenic diet provided a mean of axonal protection after transient glucose deprivation as indicated by enhanced CAP recovery in optic nerves; VI) loss of PLP1 in oligodendrocytes in a SPG2 mouse model, results in impaired axonal AP conduction during HFS but enhanced CAP/ATP homeostasis during glucose deprivation, indicating presence of compensatory mechanisms; VII) ThyAT expresses ATeam1.03<sup>YEMK</sup> in spinal cord axons in vivo and repetitive imaging is allowed by a chronic window implant.

Our study, by relying on the coupling of electrophysiological recordings of white matter tracts of ThyAT mice as axonal ATP reporter, provides a deeper understanding of WM metabolism, glial support and myelin.

### 4.1 Experimental limitations

Our experimental approach has some limitations which need to be considered for interpretation of the data. It should be noted that ATeam1.03<sup>YEMK</sup> reports the steady state concentration of ATP, which is in function of both production and consumption and therefore changes can be measured only if there is an imbalance between rate of ATP production and rate of ATP consumption. The transient decay in ATeam1.03<sup>YEMK</sup> ratio due to, for example, low substrate availability can be explained by the impossibility of ATP production in matching its relatively unchanged consumption. Therefore, the incomplete recovery of ATP signal after the stressful



condition of energy loss can be explained by the achievement of a new steady state, different from that observed at baseline, as a result of reduced consumption or production (Figure 32).

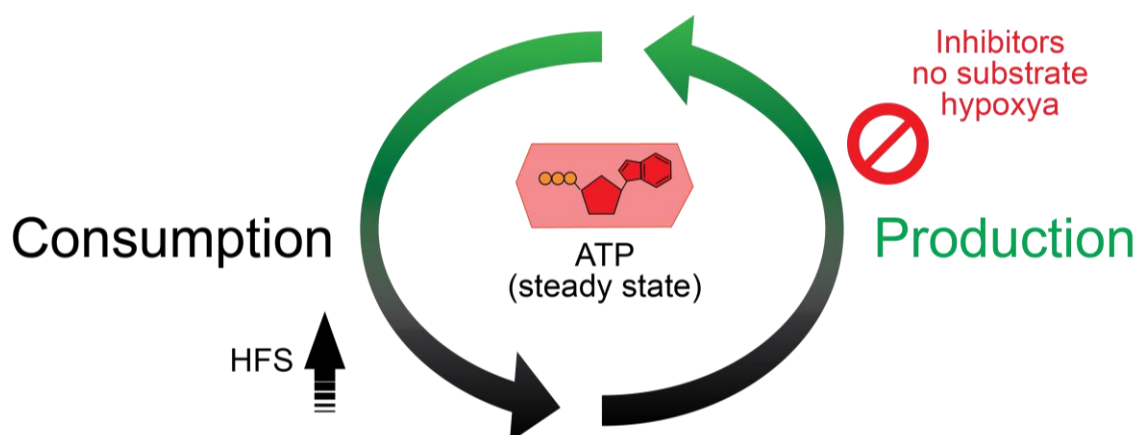


**Figure 32. Concept of ATP steady state**

Measured ATP is the result of a steady state to which two opposite processes contribute: production (via metabolic pathways) and consumption (via cellular processes). Consumption of ATP can be enhanced in neurons by electrical activity, while ATP production can be blocked by specific metabolic pathway inhibitors or lack of substrates/ oxygen.

Moreover, the correlation between two relative parameters' changes such as ATP and CAP at a given condition might appear controversial given CAP and ATP signals have different origins within the optic nerve. On one side, the CAP, evoked by supra-threshold stimulation, measures the sum of AP propagation along most of the axons (tens of thousands). In contrast, ATP imaging was performed on a single optical plane rather close to the surface of the nerve (within 15-20  $\mu\text{m}$ ), which typically contained  $29 \pm 5$  axons expressing ATeam1.03<sup>YEMK</sup>. Despite this apparent incongruence, we showed that the relationship between the two parameters is constant over many experiments (Figure 6E) suggesting that the selection of an imaging plane does not artificially determine the experimental outcome. Furthermore, comparison among experiments has been very useful, for example to confirm and understand the impact of lactate metabolism on CAP and ATP (Figure 21).

On the different nature of CAP and ATP, it has to be taken into account that in absence of active blood perfusion in the excised optic nerve ex vivo, the passive diffusion of substrates into the nerve poses the axons, and the associated glial cells located in the nerve's core, in a constant shortage of nutrients, compared to the axons and glial cells at the nerve's periphery. Due to the optical

scattering properties of a parallel organization of densely packed, highly myelinated axons that compose the optic nerve, even using 2-photon laser scanning microscopy, imaging within the core of the optic nerve is hardly possible (data not shown). Despite these limitations, our experiments present the best estimate of the simultaneous analysis of both parameters possible at the moment. Furthermore, the spatial resolution along with the averaging of the ATeam1.03<sup>YEMK</sup> signal over several axons, estimates axoplasmic ATP concentration changes of multiple fibers. At such optimized spatial and temporal resolution provided by our experimental setting, possible ATP microdomains caused by local ATP production, by mitochondria, or by consumption, e.g. by Na<sup>+</sup>/K<sup>+</sup>-ATPase at the plasma membrane (Haller, Mironov, & Richter, 2001), are missed. However, the presence of ATP microdomains is uncertain as ATP diffusion has been reported to be very fast and formation of ATP microdomains is not to be expected (Barros et al., 2013).

Finally, we considered unspecific changes, e.g. quenching of the FPs, in FRET fluorescence as potential artifacts in our measurements. In this regard, the most prominent problem that has been reported to our knowledge is yellow FP variants showing pH-dependent fluorescence changes also in physiological pH-range (Nagai et al., 2004; Zhao et al., 2011). Since ATeam1.03<sup>YEMK</sup> is a sensor based on CFP-YFP FRET pair, intrinsic changes in the YFP acceptor fluorescence could be wrongly interpreted as FRET specific effect. Even though ATeam1.03<sup>YEMK</sup> has been shown to be almost insensitive to changes in pH within the physiological range, likely due to the circular permutation of cp173mVenus (Imamura et al., 2009; Surin et al., 2014), we systematically monitored acceptor fluorescence upon direct excitation and found only minor changes in cp173mVenus fluorescence (Figure 6C-D, Figure 8B, Figure 9B and Figure 15D-F). Although we cannot fully exclude that other processes are interfering with other moieties of ATeam1.03<sup>YEMK</sup>, these results indicate that changes in pH in our experimental paradigm are possibly not directly interfering with ATP measurements.

## 4.2 Calibration of ATeam1.03<sup>YEMK</sup>

A known caveat for metabolic sensors based on the detection of a target substrate via binding proteins is their non-linearity behavior at extreme concentrations above and below their reported  $K_d$ . ATeam1.03<sup>YEMK</sup> has an apparent dissociation constant  $K_d$  equal to 1.2 mM (Imamura et al., 2009), which in practical terms means that the sensor responds in a linear way only for few millimolar units of ATP around this value (Figure 3A). At saturation, larger changes in concentrations are required to change the FRET ratio by the same amount observed in the linear phase. By calculating normalized-relative changes in FRET ratio we are prone to systematically underestimate (or, if approaching the linear range, overestimate) the calculated change in ATP underlying the ratio. This problem is particularly prominent when ATP rates and kinetics are considered. By reporting ATP rates to be enhanced following higher stimulation frequencies, we are forced to take the sensor linearity into account and make the assumption that at baseline, neuronal/axonal ATP match the values reported in the literature and close to the  $K_d$  of the sensor (1-4 mM; Rangaraju et al., 2014; Pathak et al., 2015). Given this assumption, by fitting the obtained data at HFS, we determined that the changes in ratio reflects those of ATP in a quasi-linear way and correlation between rates of ATP are valid. Nevertheless, the axonal ATP has never been experimentally assessed in a precise manner and the conclusions on ATP kinetics have to be taken with proper precautions.

Thus, for non-linearity corrections, a precise calibration of the sensor is required. However, the lack of transporters and the amount of metabolic pathways involved in the ATP homeostasis makes calibration procedures ex-vivo and in-vivo very problematic. Calibration in vitro using single-cell would represent a suitable approach, however due to the Rayleigh scattering phenomena, potential ratiometric intensity-based calibration curves obtained in cells cannot be applied to more complex systems such as acute CNS preparations where the matrix scattering elements contributes to artificial alteration in the FRET ratio. We took a different approach which does not rely on intensity determination of FRET: FLIM. Using FLIM and cell culture preparations we could describe variation in FRET as changes in lifetime  $T$  as confirmed by the observed transition of  $T$  in polar plot analysis where a pixel-based 2D coordinate transformation of  $T$  (for software limitation a single exponential decay was assumed) along a polar plot representation, displayed two different populations of the sensor's  $T$  at baseline (ATP) and following ATP washout (no ATP; Figure 33B, lower panel). We initially performed several tests using HeLa cells in order to find the highest and lowest  $T_{av-w}$  possible for the

sensor, obtaining positive results (Figure 33C). By transfecting primary astrocytes we attempt to reconstruct the calibration curve: unfortunately, using concentrations close to ATeam1.03<sup>YEMK</sup> saturation (e.g. 10 mM, Figure 33D) the  $T_{av-w}$  deviated considerably from its baseline, though closer values (or even lower than baseline's) were expected.

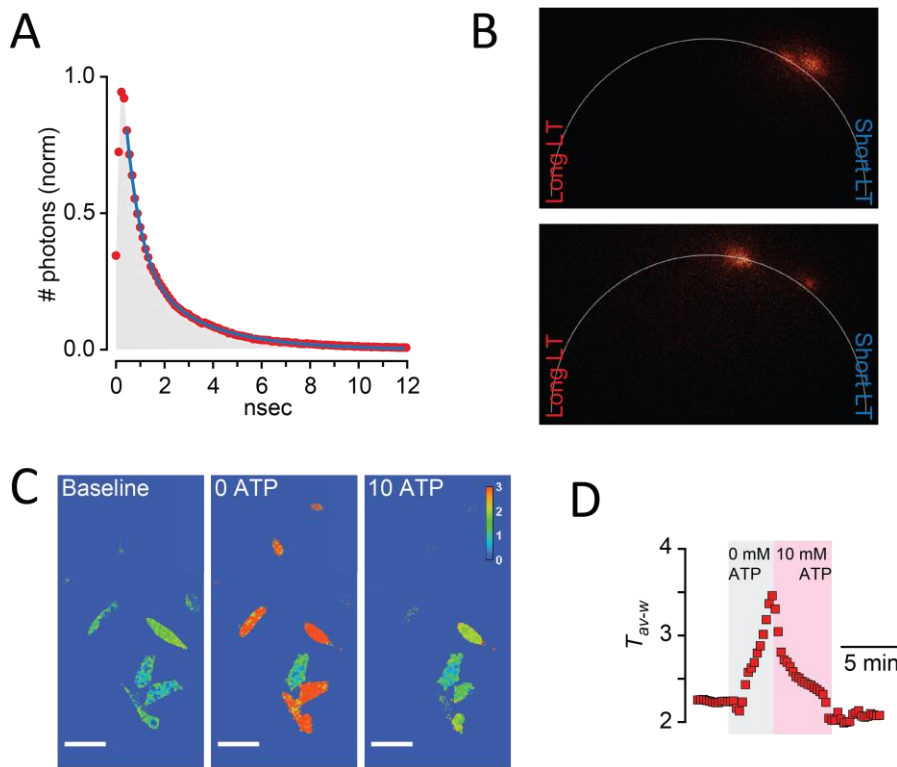


**Figure 33.** FLIM –TCSPC analysis of ATeam1.03<sup>YEMK</sup> in cultured cells and calibration.

(A) Histogram of photons' arrival at the TCSPC-PMT detector and double exponential fit model, displaying the fluorescence decay of ATeam1.03<sup>YEMK</sup> during baseline condition. (B) Phasor-plot analysis of the lifetimes (assuming mono-exponential decay) shows lifetime transition from short (baseline, on top) to long (absence of ATP: digitonin permeabilization and mitochondrial blockade with N<sub>3</sub>, bottom). (C) From left: mseCFP (donor of ATeam1.03<sup>YEMK</sup>) fluorescence transition from short to long lifetime values, when the plasma membrane of transfected HeLa cells is perforated by digitonin and ATP leaks out from cytoplasm (0 ATP). 10 mM ATP is then added in the imaging medium to saturate the sensor leading to a shortening of the LT (right). (D) Example of average-weighted lifetime ( $T_{av-w}$ ) transition during calibration to 0 mM ATP (permeabilization) and 10 mM ATP (+ 100 μM ouabain), in HeLa cells. Scale bar in (B): 50 μm.

Given it is unlikely astrocytic cytosolic ATP concentration is higher than the supposed saturation level of ATeam1.03<sup>YEMK</sup> we concluded that other processes interfered with the sensor. One likely process interfering with the fluorescence properties of the FRET-reporter could be the permeabilizing agent itself: both digitonin and aescin contain as many as 17 hydroxy groups per molecule which might cross-react with the probe.

### 4.3 Axonal ATP homeostasis and nerve conduction

Studying metabolism can be a true challenge given its hierarchical nature: metabolism in fact can be seen as a hierarchical organization spanning from single metabolites to entire CNS regions, passing through single metabolic pathways. Different techniques and model systems are required and should be used for the common aim of unraveling the whole picture (L Felipe Barros et al., 2017). The synchronized measurement of ATP as axonal energy state and nerve CAP, as a readout for nerve conduction and function, despite focusing on a single model system, covers many of these levels and allows for the first time to investigate their temporal and functional correlation in WM.

Interference with metabolic pathways of the axon, by withdrawal of substrates (GD), inhibition of mitochondrial OX-PHOS (MB) severely compromised axonal ATP as indicated by the lowest ratio obtained from ATeam1.03<sup>YEMK</sup>. The combination of GD and MB mimicked a sudden ischemic event and resulted in complete ATP loss. However, time courses of treatments differed: during GD, ATP signal began to decay only after 13 min and with a lower rate than after MB, where ATP decay was nearly instantaneous. The slower time course for energy loss observed during GD, is consistent with the breakdown of glycogen, which can be used as spare fuel (Brown & Ransom, 2007). We presumed that during MB, glycogen is still present but, in absence of active mitochondria, its breakdown by glycolysis only is insufficient to power ATP production in axons as indicated by the sudden and very fast decay of ATeam1.03<sup>YEMK</sup> ratio in the axons. These results suggest that axons strongly rely on mitochondria for ATP production. In most of energy-failure paradigms, ATP decrease matched CAP's, indicating a correlation between ATP depletion and conduction failure. Conversely, following reperfusion of the optic nerves with control aCSF, ATP signal recovered significantly later than CAP (following GD and OGD). ATP signal, unlike CAP's, is the result of two opposite processes, namely production and consumption, and its readout is the sum of both, i.e. the steady-state (see above). It is likely that ATP is produced at the beginning of reperfusion but is also immediately consumed e.g. for re-establishing ion gradients and consequently, it does not accumulate in the axoplasm. The belated onset of ATP recovery observed following OGD and GD, compared to the virtually instant rescue observed after MB and MB+GD cessation, can also be explained from the point of view of ATP production. While during aglycemia (GD) the nerve can still catabolize all available substrates, e.g. glucose, lactate and fatty acids, leading to an eventual depletion of all reservoirs (consistent with the slower decay of ATP), the sharp inhibition of mitochondrial respiration

(MB and MB+GD) doesn't allow this prolonged consumption and eventual depletion. Thus, while after glucose reperfusion following GD, glucose needs to reach the axons before it can be catabolized, after removal of the inhibitory action on mitochondria respiratory chain, following MB and MB + GD, metabolites still present in the axon can be metabolized immediately, in line with the quicker ATP recovery detected.

We experimentally achieved mitochondrial inhibition by addition of azide or by replacing oxygen with nitrogen. Although the mechanism of inhibition should be very similar for azide and nitrogen (reversible blockade of cytochrome *c* oxidase activity) we observed dissimilar dynamics of energy loss (MB vs. N<sub>2</sub>). Whereas 45 minutes of nitrogen (N<sub>2</sub>) exposure, in presence of glucose didn't cause ATP loss (contrary to expectations, the signal increased), a short 5 minute exposure to 5 mM azide, even in presence of glucose, caused complete ATP depletion. We presume that the substitution of oxygen with nitrogen (sparging) was incomplete and some dissolved oxygen might still have been present when the solution reached the nerve. Despite being provided with nitrogen, the chamber was in fact not air-tight. Given the very small volume of aCSF flowing to the nerve (high surface-to-volume ratio), the lack of air-tightness could have facilitated oxygen to dissolve into the aCSF transforming an intended anoxia into a milder hypoxia. The observed relative 20-30% increase in ATP signal from baseline, following nitrogen exposure was described both during N<sub>2</sub> and OGD. In absence of active perfusion of oxygen by blood circulation, aCSF saturation with 95% oxygen is possibly a compromise to maintain acute preparations of CNS structure viable *ex vivo*. Providing oxygen has a diffusion gradient towards the nerve core, under normal circumstances of oxygenated aCSF, the oxygen levels in the nerve's core correspond to hypoxic conditions (Mulkey, Henderson, Olson, Putnam, & Dean, 2001) while the axons running at the nerve's periphery are under oxidative stress (D'Agostino, Putnam, & Dean, 2007; Mulkey et al., 2001). During hypoxia, the imaged fibers at the periphery of the nerve are temporarily released from the oxidative stress induced by the high oxygen present at baseline, and normally used to keep acute preparations of CNS structure viable *ex-vivo*. Considering the nature of the recorder ATP (imaged within 20 μm from the surface) and CAP (reflecting the conduction of virtually all axons), the presence of a diffusion gradient for oxygen might explain the ATP-CAP signal divergence under N<sub>2</sub> treatment. The production of superoxide radicals are known to interfere directly with the cell energy metabolism at the level of the TCA cycle superoxide-sensitive enzymes: aconitase and fumarase (Gardner & Fridovich, 1993). Superoxide

might also induce axons and glial cells to activate compensatory mechanisms (e.g. glutathione) that require energy (Lu, 2009; Meister & Anderson, 1983). Similarly to N<sub>2</sub>, an initial 20-30% increase in ATP signal was also observed during OGD (combination of N<sub>2</sub> and GD; Figure 10C), but this effect was quickly overrun by the lack of substrates, setting the decay onset at 12.2 ± 1.0 min for ATP and 12.0 ± 1.0 min for CAP signal (Figure 10D, lower-right panel).

Given the low control on oxygen levels provided by N<sub>2</sub>, the pharmacological inhibition induced by azide provides a better model to study acute ischemic events in ex-vivo preparations. To study oxygen impact (normoxia, anoxia, etc.) on WM metabolism, devices that allow a precise control on oxygen partial pressure should be employed (Mauleon, Fall, & Eddington, 2012).

Axons of the optic nerve are sensory projections of the retinal ganglion cells (RGCs) and, under physiological conditions, action potentials are generated in frequencies between 0.1 and 25 Hz, with most firing rates between 3 and 10 Hz (data obtained for guinea pig; (Koch et al., 2006; Perge, Koch, Miller, Sterling, & Balasubramanian, 2009). The axonal ATP of optic nerves superfused with 10 mM glucose wasn't altered by physiological stimulation rates between 1 and 7 Hz (Figure 12D-E). The stability of the ATP signal under these physiological stimulations suggests that the metabolic architecture of the optic nerve is adjusted to maintain ATP constant under normal and sustained activity. As soon as the physiological activity threshold was exceeded by the HFS (>15 Hz), axonal ATP showed a reversible decline, whose amplitude directly correlated with the rise of the stimulation frequency. Even though these supra-physiological stimulation rates are not found in vivo, they represent an important tool to understand the metabolic adaptation to increase energy requirements by WM. Unlike the described energy failure paradigms, where the energy consumption was kept constant by the lack of substrate availability, during HFS the metabolic demand possibly increases in a stimulation-dependent fashion. The increase in demand is likely driven by the activation of the Na/K ATPase (Attwell & Laughlin, 2001; Johar, Priya, & Wong-Riley, 2014) and is accompanied by Ca<sup>2+</sup> accumulation in the axon following AP propagation (Lev-Ram & Grinvald, 1987; Zhang, Wilson, Williams, & Chiu, 2006): calcium influx regulates glycolysis via Ca<sup>2+</sup>/calmodulin-dependent protein kinase (Mieskes, Kuduz, & Soling, 1987) and trigger mitochondrial ATP synthesis by increasing malate-aspartate shuttle and pyruvate mitochondrial oxidation (Rueda et al., 2014). The idea of metabolic activation concomitant with the increased demand of ATP seems to be supported by the observation that, at HFS cessation, ATP recovery rates positively correlate with the amplitude

of signal decay achieved at the end of the stimulation. The experimental manipulation of WM energy production and consumption has the advantage of providing a better understanding of glial cell contribution in terms of energy support to axonal function.

To provide a different approach to the study of WM energy homeostasis, we employed CAG-GO-ATeam optic nerves in collaboration with Dr. Natsubori at Keio University. GO-ATeam, a red-shifted ATP sensor, is expressed globally in all CNS cell types: sparse labeling expression however, allowed to visualize single cells in the optic nerve (Figure 18B-D). Electrical stimulation (RAMP) showed mild ATP-depletion probably consistent with labeling of a smaller subset of axons than in ThyAT (indistinguishable from other cellular processes), however, direct ATP-responses by other cells (e.g. pericytes, oligodendrocytes, etc.) cannot be excluded because of the nature of the CAG reporter line. The prevalence of cells and processes in CAG-GO-ATeam optic nerves served as a point of comparison with axonal specific ATP reporter (ThyAT) nerves. While simultaneous blockade of mitochondria and glucose deprivation also depleted ATP very quickly, glucose deprivation in CAG-GO-ATeam nerves induced a faster affect albeit smaller in amplitude, on ATP loss, than ThyAT axons. Intriguing, the recovery from GD obtained by glucose reperfusion gave rise to an instantaneous ATP signal rescue in CAG-GO-ATeam. Conversely, in ThyAT optic nerves, the ATP rescue happened only after 10 minutes from glucose reintroduction in a similar paradigm. Given the higher specificity for axonal ATP provided by Thy1.2 promoter, we hypothesize that either I) axons are possibly less glycolytic and have to rely on other cells for support and energy production; II) axons require more energy to maintain their structure and function; III) during passive diffusion of substrates, glial cells and pericytes in particular are in front position to uptake and oxidize glucose. The first hypothesis is supported by the observation that lack of glial cell glycolysis results in neurodegeneration while neuronal glycolysis is not required (in drosophila; Volkenhoff et al., 2015; Schirmeier et al., 2016). On the second hypothesis, similarly to neurons in gray matter it can be assumed that most of the energy expenditure in WM is accounted by the axons (Harris & Attwell, 2012; Laughlin, de Ruyter van Steveninck, & Anderson, 1998). However, we cannot exclude coexistence of these three hypothesis and to further study metabolic heterogeneity in WM, the observations made in CAG-GO-ATeam and ThyAT optic nerves should be extended e.g. with other metabolic reporters/ promoters and by using specific metabolic pathway inhibitors.



Is lactate the substrate used by glial cells to bridge their metabolism to support energy production in axons?

Whether neurons, and their axons, prefer glucose or lactate as their main energy substrate during rest and activity is still a matter of debate (Díaz-García et al., 2017; Dienel, 2012; J. Hirrlinger & Nave, 2014; Luc Pellerin & Magistretti, 2012). Both substrates can sustain CAP propagation in the optic nerve and astrocytes metabolize stored glycogen to lactate, during HFS or OGD, to support axonal energy homeostasis (Brown et al., 2005, 2003, 2001). We investigated whether, under enhanced axonal energy demand forced by HFS, lactate and pyruvate can be utilized by the nerve in the same way as glucose. In line with previous findings (Brown et al., 2001), lactate and pyruvate support CAPs similarly as glucose even during HFS. However axonal ATP decayed significantly more during HFS when lactate or pyruvate were present as the sole energy substrates. Consistent with this result, under glutamate stimulation, ATP production in cultured cerebellar neurons has been shown to be well maintained only by glucose (Lange et al., 2015). Nevertheless, our results show that lactate derived from glucose oxidation is involved in axonal ATP homeostasis. Under inhibition of endogenous lactate metabolism, with D-lactate or by selectively blocking MCT1-2 by AR-C155858, ATP reached a significantly lower steady state at the end of HFS, as a result of either increased ATP consumption or reduced production (Figure 32). However, MCT1<sup>het</sup> optic nerves did not show significant differences in ATP levels after stimulation at HFS, compared to wild type mice. MCT1<sup>het</sup> mice have only half of the transporter proteins in glial cells and, even though old MCT1<sup>het</sup> mice show axonopathy in small caliber fibers (Lee et al., 2012), the reduced amount of transporters they have, or possible compensatory mechanisms, might play a role in maintaining WM energy metabolism viable at the studied time point (10 weeks). Thus, the pharmacological inhibition of MCTs and lactate metabolism provides a thorough approach to confirm the contribution of endogenous lactate production to ATP generation. Direct supply of lactate seems not to be as effective as endogenous glucose-derived lactate. Therefore, we suggest that WM organization creates a preferential pathway for glucose, the main circulating substrate. This preferential pathway uses GLUT1 transporters facing the luminal side to uptake glucose into glial cells which follows rapid hexokinase phosphorylation and conversion to lactate. Lactate produced from glucose can probably serve as a local supply, in contrast to when it is superfused in the aCSF. This preferential pathway relies also on gap-junction formations between glial cells (J. Hirrlinger & Nave, 2014) which allow endogenous lactate to diffuse

very quickly, without the need for rate-limiting MCTs, reaching axons faster. Using our experimental setup we could show this higher metabolic power of endogenously-produced lactate in maintaining ATP production and the dominant role of glucose in energy production in WM.

Glucose is the main carbon source leading to ATP generation in the CNS, however, ketone bodies are an important resource during prolonged caloric restriction periods. In absence of glucose, our results showed acetoacetate failed to maintain ATP production and conduction in the optic nerves, in the presence of  $\beta$ -Hydroxybutyrate ( $\beta$ -HB) as substrate. We hypothesize this was due to the rate limiting reaction of acetoacetate conversion into acetyl-CoA that fuels the TCA cycle. This limitation was likely due to low expression of mitochondrial SCOT enzymes. Bypassing this rate-limiting step by inducing ketogenic conditions, which increases expression of mitochondrial SCOT enzymes (Düking et al., unpublished data) or by inducing regulatory modifications on this ketolytic enzyme (Turko, Marcondes, & Murad, 2001) failed to maintain axonal ATP and CAP in the presence of  $\beta$ -HB as substrate. Strikingly, the recovery of optic nerve conduction, was nearly complete in optic nerves from ketogenic diet treated mice after glucose was re-introduced. This finding fits the extensive data supporting the neuroprotective effect of a ketogenic diet (Maalouf, Rho, & Mattson, 2009; Newman & Verdin, 2014, 2017; Rahman et al., 2014).

#### **4.4 Myelin role in controlling ATP homeostasis: PLP mutants**

Myelin lowers the energetic costs for action potential propagation, but at the same time it restricts the axons from accessing extracellular metabolites (J. Hirrlinger & Nave, 2014). To bypass this obstacle, oligodendrocytes use myelin sheaths as an active interface that metabolically support axons (Nave 2010; Lee et al., 2012; Fünfschilling et al., 2012; Hirrlinger & Nave 2014). What is the functional impact on this regulated coupling if myelin stability and function are compromised? We addressed this question by crossbreeding the ThyAT reporter mice with mice deficient for the major myelin protein PLP, a model mouse line for human spastic paraplegia type 2.

Optic nerves from 10 weeks old ThyAT  $\times$  PLP<sup>KO</sup> mice were acutely isolated. Although axonal degeneration is not reported at this age (Edgar et al., 2004; Griffiths et al., 1998) early signs of white matter impairment (i.e. axonal swellings, conduction loss and CAP lag) were observed (Figure 25). PLP<sup>KO</sup> optic nerves were thus challenged with HFS. The results reported a further conduction (CAP) impairment from the population of responding fibers (i.e. in which APs could be elicited) indicating

an enhanced susceptibility of PLP<sup>KO</sup> WM. Surprisingly, axonal ATP was barely altered during the stimulation and only minor impairments were shown when single frequencies (16, 50 Hz) were used. It is possible that during the transient increase in energetic demand triggered by HFS, the axons of PLP<sup>KO</sup> nerves are still well supported by glial cells and myelin instability does not interfere with the support mechanisms. Consequently, the observed conduction impairment in PLP<sup>KO</sup> nerves could be strictly functional, for example due to alteration in K<sup>+</sup> channel distribution, as reported for other myelin mutant models (Rasband, Trimmer, Peles, Levinson, & Shrager, 1999; Sinha, Karimi-Abdolrezaee, Velumian, & Fehlings, 2006).

We further investigated energy homeostasis in PLP<sup>KO</sup> mice by exposing the optic nerve to a transient period of aglycemia (glucose deprivation, GD). In sharp contrast to the predicted results, CAP and the ATP signal from PLP<sup>KO</sup> optic nerves decayed with slower kinetics than controls during the shortage of metabolites, possibly indicating the presence of compensatory mechanisms supporting PLP-lacking nerves. In line with this observation, as glucose was restored, PLP<sup>KO</sup> nerves also recovered much more vigorously than controls, outreaching controls in total ATP. An in-depth analysis showed small caliber fibers to contribute more substantially than large caliber fibers to this observed increase in ATP rescue. Interestingly, small fibers in the optic nerves of PLP<sup>KO</sup> mice show more frequent swellings than larger ones (Griffiths, 1998; Griffiths et al., 1998). Furthermore, as previously discussed, the increase in recovered ATP following an energy deprivation is a result of a new steady state and might be conceptually uncoupled from recovery of conductance (similar in extent for PLP<sup>KO</sup> and control nerves) indicating a more efficient mechanism of ATP generation which might be the result of a compensatory mechanism. Along these lines, two further observations should be considered: I) PLP<sup>KO</sup> mice show an increase of the GLUT1 and MCT1 transporters within myelin (Kusch et al., unpublished), which are found in non-compacted myelin regions at the inner and outer tongue in wildtype white matter; II) Non-compacted regions of myelin are more frequent in PLP<sup>KO</sup> animals (Möbius W., unpublished observation). These two findings might underlie an increase in the flow of substrates towards the axons and therefore might contribute to the observed phenotype. Further supporting this hypothesis, the observed dysregulation of kinase proteins involved in glucose metabolism in PLP<sup>KO</sup> (e.g. PAK1 and PEA-15, linked to regulation of PGM (Phosphoglycerate mutase, glycolytic enzyme) and GLUT1/3 insertion in the plasma membrane (Kusch et al., unpublished).

PLP<sup>KO</sup> mice develop an early axonal transport deficit with transport cargo, including mitochondria, being trapped on the distal side of nodes of Ranvier (Edgar et al., 2004). While myelin appears grossly normal at this early stage (as well as at the age of 10 weeks, our current experiments timepoint; Griffiths et al., 1998; Griffiths 1998), our findings suggest the presence of compensatory mechanisms, acting against a functional impairment and setting a new ATP steady state. During axonal action potential propagation, glutamate is released from axons activating NMDA receptors on myelin and resulting in Ca<sup>2+</sup> signals in myelin and oligodendrocytes (Kriegler & Chiu, 1993; Ileana Micu et al., 2007, 2016). Activation of NMDA receptors on oligodendrocytes also increase the membrane expression of GLUT1 transporters (Saab et al., 2016). The metabolic targets of Ca<sup>2+</sup> signals within the oligodendrocytes might include a Ca<sup>2+</sup>/calmodulin-dependent protein kinase (Mieskes et al., 1987), together with regulation of mitochondrial ATP synthesis via enhanced malate-aspartate shuttle and pyruvate mitochondrial oxidation (Rueda et al., 2014). This Ca<sup>2+</sup> regulated mechanism might result in an upregulation of lactate transfer from myelin to axons (Fünfschilling et al., 2012; Lee et al., 2012) which would therefore represent a prime candidate to enhance axonal ATP production. In conclusion, by monitoring axonal ATP and nerve CAP we could demonstrate the presence of energy adaptation mechanisms, mainly in small fibers, in parallel to conduction impairments. The CAP impairment could potentially reflect a myelin architectural deficit which is compensated by an enhanced flux of metabolites to the nerve. The physical absence of PLP1 in the myelin compartment of this mouse model for hSPG2 could in fact lead to myelin and conduction instabilities but also to cytosolic channel openings where transporters can be inserted, thereby facilitating the flux of metabolites and partially compensating the costs for AP propagation at high rates.

This approach for studying WM metabolism has proved to be very sensitive to detect mutant oligodendrocytes' effects on axonal energy metabolism and physiology, months before the onset of axonal loss and spastic paraplegia clinical symptoms. To unravel the complete pathological impact of PLP1 mutation on axonal metabolism, further analysis should be considered, for example aiming at blocking specific axonal support pathways or at visualizing additional metabolite fluxes between oligodendroglia and axonal compartment.

## 4.5 Conclusions

Our approach combines confocal axonal ATP imaging in a new transgenic mouse line with electrophysiology of CAPs in acutely isolated optic nerves. Such approach represents a novel method to assess energy homeostasis in correlation to the ability of electrical signal propagation along white matter tracts. This new technical approach allowed us to provide insights about energy metabolism in white matter. Moreover we demonstrated that CAP and the axonal energy status are not intimately correlated as previously assumed and a more complex interaction has to be considered. As disturbances of energy metabolism or glial support contributes to numerous CNS diseases, including spastic paraplegia investigated in this work, this new approach will allow to investigate metabolic dysregulations that precede or are concomitant with the degeneration process. Based on these insights, new therapeutic strategies might be designed aiming at preserving the axonal energy balance and the functional connectivity of neurons with their presynaptic terminals



## 5 Outlook

We combined metabolic imaging and nerve electrophysiology to generate a novel approach for studying metabolism and its implication in neuronal function. This new technical approach provides an advancement in the study of white matter metabolism and its energy balance by promoting the understanding of the complex metabolic connectivity within myelinated fiber tracts. The strength of this approach resides in its coverage of several complexity levels in the hierarchic structure of metabolism: from the single metabolite to the pathways involved in its production within and among cells, by using specific pathway inhibitors. It allows studying metabolites with unprecedented resolution in time and space. However, this approach can have certain limitations when substrate concentrations need to be quantified. Therefore, a reasonable alternative is fluorescence lifetime measurements using 2-photon laser-scanning microscopy (i.e. FLIM). Contrary to the intensity based approach used in this thesis, FLIM is insensitive to phenomena such as wavelength-dependent light scattering or bleaching. Therefore, together with proper calibration of metabolic sensors, FLIM can provide absolute readouts for metabolites allowing a more precise comparison between mutants and wildtype animals or between different regions of white and gray matter.

The use of ex-vivo preparations presents certain limitations as well. Two of these limitations are important in the assessment of metabolism: I) the lack of active blood perfusion which, as discussed, leads to non-linear phenomena like the passive diffusion of substrates, metabolites and gas across the tissue; II) the limited time window in which the preparation can be considered viable before intrinsic degenerative phenomena begin (i.e. Wallerian degeneration for white matter). To overcome these limitations, it is necessary to extend from ex-vivo observations to an in-vivo system where imaging and electrophysiology can be unceasingly performed over a prolonged period of time. Unfortunately, CNS white matter tracts, by running deeply within the tissue, give scarce accessibility to conventional optical systems. However, optical access to the spino-cortical white matter tracts using a single surgical procedure has been described (Farrar et al., 2012; Farrar & Schaffer, 2014). In this thesis, we demonstrate the feasibility of assessing the metabolic state of spino-cortical white matter in vivo using FRET. This preparation can be combined with electrophysiological recordings of CAP and with viral vector technology, offering an experimental platform that supports ex-vivo observations. Moreover, it can help understand white matter vascular coupling to glial cells and axons, and the correlation of axonal functional properties under physiological condition. It also

experimentally extends the limited time window that ex-vivo preparations provide, allowing the study of acute demyelination and oligodendrocyte remyelination, their role in axonal energy budget, and their impact on axonal functionality and viability.



## 6 Material and Methods

### 6.1 Solutions

All master solutions were pH adjusted to 7.4 at the experimental temperature using HCl or NaOH solutions following gas (carbogen/ nitrogen)-equilibration.

#### 6.1.1 aCSF

aCSF solution was used to superfused the optic nerves in the incubation chamber. aCSF was prepared by mixing 2X stock solutions A (NaCl, KCl) and B (NaH<sub>2</sub>PO<sub>4</sub>, NaHCO<sub>3</sub>, MgSO<sub>4</sub>) kept at 4 °C. CaCl<sub>2</sub> was then added from a 4 M stock solution (i.e. 2000 dilution) and glucose, sucrose and other substrates and drugs were finally added. The aCSF master solution was warmed to 37 °C and gassed with carbogen mixture (95% O<sub>2</sub> / 5% CO<sub>2</sub>) for about 1 hour before pH was adjusted and final solutions mixed separately. For lactate and other Na-salts compounds whose final concentration exceeded 1 mM, Na<sup>+</sup> was reduced in the stock solution to keep its concentration constant. In case the drug (e.g. AR-C155858) was diluted from DMSO stock, control solutions were created by adjusting DMSO volume. The composition of the aCSF master solution was:

	<b>mM</b>	<b>MW (g·mol<sup>-1</sup>)</b>	<b>mOsm</b>
NaCl	126	58.44	252
KCl	3	74.55	6
NaH <sub>2</sub> PO <sub>4</sub>	1.25	137.99	2.5
NaHCO <sub>3</sub>	26	84.01	52
MgSO <sub>4</sub>	2	246.48	4
CaCl <sub>2</sub>	2	147.02	6
Substrate	10	-	10

### 6.1.2 AP buffer

AP buffer was used for perfusion of mixed neuro-glia culture. AP buffer is an HEPES-based imaging medium. The master solution was prepared by mixing:

	<b>mM</b>	<b>MW (g·mol<sup>-1</sup>)</b>	<b>mOsm</b>
HEPES	20.0	238.31	20.0
CaCl <sub>2</sub>	1.8	147.02	5.4
MgCl <sub>2</sub>	1.0	203.3	3.0
KCl	5.4	74.56	10.8
NaCl	110.0	58.44	220.0
Na <sub>2</sub> HPO <sub>4</sub>	0.8	177.99	2.4
Substrate	20.0	-	20.0

CaCl<sub>2</sub> was added from a 4 M stock (2222.22 fold dilution) before pH adjustment to 7.4 using NaOH solution. Finally, substrates (e.g. glucose, sucrose) and drugs were all added separately from powder or stock solutions at the beginning of each experiment. For lactate and other Na-salts compounds whose final concentration exceeded 1 mM, Na<sup>+</sup> was reduced in the stock solution to keep its final concentration constant (110 mM). In case the drug (e.g. ouabain) was diluted from DMSO stock, control solutions were created by adjusting DMSO volume.

### 6.1.3 AT imaging medium

AT imaging medium was used for the calibration of Ateam1.03<sup>YEMK</sup> in HeLa cells and primary astrocytes. pH is kept constant by HEPES, carbonate as well as phosphate buffering. The master solution was prepared by mixing two 2x stock solution (1 = NaCl, KCl, HEPES, NaH<sub>2</sub>PO<sub>4</sub>, NaOH; 2 = MgSO<sub>3</sub>, NaHCO<sub>3</sub>, Na<sub>2</sub>HPO<sub>4</sub>) in equal amounts. CaCl<sub>2</sub> was added separately from a 4 M stock (2222.22 dilution factor). NaOH is included in the master solution in the attempt to balance the acidic pH created by HEPES and account for the extra Na<sup>+</sup> introduced. The final master solution was:

	<b>mM</b>	<b>MW (g·mol<sup>-1</sup>)</b>	<b>mOSm</b>
NaCl	91.77125	58.44	183.5425
NaHCO <sub>3</sub>	17.856	84.007	35.712
HEPES	20	238.3012	20
KCl	5.366	74.5515	10.732
MgSO <sub>4</sub> ·7H <sub>2</sub> O	0.811	246.4755	1.622
NaH <sub>2</sub> PO <sub>4</sub> ·H <sub>2</sub> O	0.906	137.99	1.812
Na <sub>2</sub> HPO <sub>4</sub> ·2H <sub>2</sub> O	0.2265	177.99	0.6795
CaCl <sub>2</sub> ·2H <sub>2</sub> O	1.8	147.02	5.4
Substrate	20	-	20
NaOH	15.5	39.9971	15.5

AT imaging medium was warmed to 37 °C or RT depending on the experimental temperature before pH was adjusted to 7.4 using HCl solution. Appropriate substrates and drugs were added to the final solution mixture. Na<sup>+</sup> and DMSO were adjusted in the control solution accordingly.

## 6.2 Transgenic mice

Animals were bred in the animal facility of the Max-Planck-Institute for Experimental Medicine and treated in accordance with the German Protection of Animals Act (TSchG §4 Abs. 3) and with the guidelines for the welfare of experimental animals issued by the European Communities Council Directive 2010/63/EU. Mice were housed in a 12h/12h light dark cycle with access to food and water ad libitum. The transgene construct was assembled in pTSC (P. G. Hirrlinger et al., 2005) containing Thy1.2 promoter sequences. The plasmid pDR-GW AT1.03<sup>YEMK</sup> containing the open reading frame of the ATP-sensor ATeam1.03<sup>YEMK</sup> (Imamura et al., 2009) was obtained from Wolf Frommer (via Addgene; plasmid #28004). The open reading frame of ATeam1.03<sup>YEMK</sup> was subcloned into the XhoI restriction site of pTSC using PCR. The linearized transgene was injected into fertilized mouse oocytes of the C57BL/6J mouse strain. Transgenic founders were identified using PCR based genotyping on genomic DNA isolated from tail tips (see section 6.2.3 and 6.2.4).

CAG-GO-ATeam mice were transferred from the department of neuropsychiatry at the Keio University School of Medicine in Tokyo (Japan) to our lab in Göttingen and kept in the quarantine of the animal facility until experiments were performed.

### 6.2.1 Determination of copy number

Mouse genomic DNA was isolated from tail biopsies of four C57BL/6J and six ThyAT-mice with Invisorb® Spin Tissue Mini Kit according to the manufacturer's instructions (Stratec Biomedical, Birkenfeld, Germany). Short FAM-labeled hydrolysis probes (UPL) were used for qPCR reactions (Roche Diagnostics GmbH, Mannheim, Germany). Primers and the UPL-probe were designed by ProbeFinder version 2.50 for Mouse (Roche Diagnostics; Primer Thy1s: TGCCGGTGTGTTGAGCTA; Thy1as: TGGTCCTGTGTTTCATTGCTG; UPL 60; amplicon 73 bp). The genomic sequence of Nrg1 was used to calibrate for the amount of DNA (Primer Nrg1s: GGCTATAATGCTAACACAGTCCAA; Nrg1as: AGTGGATCGTAACAACACTGTCA; UPL 38; amplicon 61 bp) as described (Besser et al., 2015). 10 to 25 ng of genomic DNA was subjected to qPCR amplification to measuring the amount of Thy1.2 on a Light Cycler 480 system (Roche Diagnostics GmbH, Mannheim, Germany) according to the manufacturer's instructions. The copy number of the Thy1.2-ATeam1.03<sup>YEMK</sup> transgene was calculated using the  $\Delta\Delta C_t$  method compared to wild type mice carrying only the two endogenous allele of the Thy1 gene (Besser et al., 2015). This analysis was kindly performed by Grit Marx, Carl-Ludwig-Institute for Physiology, University of Leipzig.

### 6.2.2 Analysis of the sensor expression pattern

Adult mice were transcardially perfused with 4% formaldehyde solution (PFA, in phosphate buffered saline: 137mM NaCl, 2.7mM KCl, 8mM Na<sub>2</sub>HPO<sub>4</sub>, 1.5mM KH<sub>2</sub>PO<sub>4</sub>, pH 7.4) under deep anesthesia. The brain and the eyes were removed and post-fixed for 24 h in the same fixative. 45 $\mu$ m thick sections were cut on a vibratome (Leica VT1000 S, Nussloch, Germany) and slices were mounted directly after cutting with Vectashield embedding medium (Vectashield HardSet™ Mounting Medium, Vector Laboratories, Burlingame, CA, USA). From the eyes retinal whole mounts were prepared.

For imaging of fixed brain slices and retina, confocal images were acquired on a LSM Olympus IX71 inverted microscope using an UPlanFL 10x/0.3 objective (Olympus) for overview images (Figure 3A-C, G) or an UApo/340 40x/1.35 oil objective (Olympus) for detailed images (Figure 3D-F, H), respectively. Microscopic images were acquired and processed using Olympus Software Fluoview v5.0. ATeam1.03<sup>YEMK</sup> sensor fluorescence was excited with a 488 nm argon laser and detected through

a BA 510-540 nm emission filter (AHF Analysentechnik AG, Tübingen, Germany). For all images, a Kalman filter of 2 was used for denoising and images were acquired with 1024 x 1024 resolution (pixel size for overview images: 0.9 $\mu$ m; pixel size for detail images: 0.35  $\mu$ m). Z-stacks comprise 12-38 singles z-planes for overview images and 30-85 z-planes for detailed images, respectively, with distances between each z-plane of 2  $\mu$ m (overview), 0.5 $\mu$ m (Figure 3D-F) and 0.35 $\mu$ m (Figure 3H). Single z-stacks were converted to maximum intensity projections (by using Fiji macro "Flattening V2f.ijm"; generously provided by Jens Eilers) and for overview images maximum intensity projections of different positions (210 for Figure 3A; 154 for Figure 3B; 160 for Figure 3C; 49 for Figure 3G) were stitched by using Fiji software and a Fiji stitching plugin (Preibisch, Saalfeld, & Tomancak, 2009). This analysis was in part kindly performed by Dr. Ulrike Winkler, Carl-Ludwig-Institute for Physiology, University of Leipzig.

### 6.2.3 Preparation of mouse genomic DNA

DNA isolation for transgenic animal identification via PCR genotyping was performed using two different and interchangeable methods:

#### 1) Nexttec™ Tissue & Cells kit-based genomic DNA isolation

Nexttec™ Tissue & Cells kit was used to isolate DNA from tail or ear biopsies. Isolation was performed according to manufactures protocol. Biopsies were lysed in 300  $\mu$ l lysis buffer (265  $\mu$ l buffer G1, 10  $\mu$ l buffer G2, 25  $\mu$ l buffer G3) by vigorous shaking for 60-120 min at 1200 rpm and 62 °C. Meanwhile, Nexttec™ cleanPlate96 were equilibrated with 350  $\mu$ l Prep buffer for 5 min at RT and centrifuged for 1 min at 350 G. 120  $\mu$ l of the lysates were loaded onto the columns and centrifuged at 750 G for 1 min into fresh tubes. Lysates were diluted 1:5 in ddH<sub>2</sub>O. 1  $\mu$ l of the lysate was used in genotyping PCR reactions.

#### 2) Chloroform DNA extraction

DNA was isolated from tail or ear biopsies using 400  $\mu$ l of extraction buffer (0.5% SDS, 0.1 M NaCl, 0.05 M Tris (pH 8.0), 3 mM EDTA), added directly into each tube containing the biopsy. In addition, 75  $\mu$ l of 8 M potassium acetate (sterile-filtered; pH not adjusted), and 400  $\mu$ l chloroform were added. The solution was mixed by vortexing for approximately 10 s, until a cloudy appearance was obtained. Samples were then centrifuged (5415 D Eppendorf) for

10 min at 4 °C (750 G). 200 µl of the supernatant containing the genomic DNA were transferred to a new tube and precipitated chloroform waste was kept under fume cupboard and properly discarded. 400 µl 100% ethanol were added, and the samples were mixed by inverting the tubes. Subsequently, samples were centrifuged for 10 min at RT (maximum speed). The supernatant was completely removed and the pellets were air dried for 30-45 min. Finally, 200 µl Tris buffer (10 mM Tris pH 8.0) were added to resuspend the DNA. Samples were vortexed and stored at 4 °C for further analysis.

#### 6.2.4 Genomic DNA analysis by PCR DNA-amplification

Polymerase chain reaction (PCR) is a multi-step enzymatic amplification of a DNA sequence (template) of interest in vitro (Mullis et al., 1986). The reaction cycles through denaturation, annealing, and extension of the DNA template sequence using flanking primers, i.e. two short (18-30 bp) single strand DNA sequences complementary to the 5'-3' (sense) and 3'-5' (antisense) regions upstream and downstream the sequence of interest. PCR reactions require a thermostable DNA polymerase, which is stable at the melting temperature of the double stranded DNA and has an optimal activity at around 72 °C. Standard PCR master mixes for genotyping were set up with RedTaq polymerase (Sigma) or GoTaq DNA polymerase (Promega) following manufacture's specification. Specific primers for every mouse line were used.

PCR master mix for RedTaq polymerase:

1.00 µl	DNA (100 pg-100 ng)
0.10 µl	sense primer (50 pM)
0.10 µl	antisense primer (50 pM)
2.00 µl	dNTP mix (2 mM)
2.00 µl	10x RedTaq buffer
0.80 µl	RedTaq polymerase (1 U/µl)
14.00 µl	ddH <sub>2</sub> O

PCR master mix for GoTaq polymerase:

1.00 µl	DNA (100 pg-100 ng)
0.10 µl	sense primer (50 pM)
0.10 µl	antisense primer (50 pM)
2.00 µl	dNTP mix (2 mM)
4.00 µl	5x GoTaq buffer
0.15 µl	GoTaq polymerase (5 U/µl)
12.65 µl	ddH <sub>2</sub> O

### 6.2.5 Primers

Primers were designed based on the template sequence information using the DNASTar™ LaserGene SeqBuilder software, and OligoAnalyzer 3.1 (<http://eu.idtdna.com/calc/analyzer>). Oligonucleotides were synthesized in-house at the AGCTlab (AGCTlab@em.mpg.de) of the Max-Planck-Institute of Experimental Medicine.

Sense primer for ThyAT:

5'-TCTGAGTGGCAAAGGACCTTAGG-3'

Antisense primer for ThyAT:

5'-CGCTGAACTTGTGGCCGTTTACG-3'

Sense primer for PLP

5'-TTG GCG GCG AAT GGG CTG AC-3'

Antisense primer #1

5'-GGA GAG GAG GAG GGA AAC GAG-3'

Antisense primer #2

5'-TCT GTT TTG CGG CTG ACT TTG-3'

### 6.2.6 PCR programs for genotyping

*ThyAT*:

95 °C<sup>03:00</sup>

{60 °C<sup>00:30</sup>

72 °C<sup>00:30</sup>

95 °C<sup>00:30</sup>}<sub>35</sub>

60 °C<sup>00:30</sup>

72 °C<sup>05:00</sup>

4 °C<sup>II</sup>

[Expected bp product: 247bp].

*PLP<sup>KO</sup>*:

95 °C<sup>03:00</sup>

{56 °C<sup>00:30</sup>

72 °C<sup>01:00</sup>

95 °C<sup>00:30</sup>}<sub>36</sub>

56 °C<sup>02:00</sup>

72 °C<sup>10:00</sup>

4 °C<sup>II</sup>

[Expected bp products: 300 bp (absence of *Plp<sup>KO</sup>*) and 150 bp (*Plp<sup>wt</sup>*). Heterozygote animals should be recognized by the presence of both products].

### 6.3 Ketogenic diet

After one-off overnight food-restriction, the mice were fed *ad libitum* with fat-enriched diet (Ssniff Spezialdiäten GmbH: Ketogenic HF diet #E15149) for 30 days before the final ex-vivo experiment was performed. The high-fat food contained 79.2% Fat, 8.4% proteins, 4.4% ash (minerals), 4.3% fibers and 2.4% carbohydrates, carrying about 7.5 kcal/g, i.e. approximately 3.5 kcal/g more than the normal chow. Control mice were kept on the regular high-carbohydrate food-pellet and didn't undergo starvation.



#### 6.4 Blood measurement of glucose and $\beta$ -hydroxybutyrate

To monitor the efficacy of ketogenic diet in enhancing blood ketone levels we withdrew blood samples from mice that were kept on ketogenic diet and control mice once a week for 4 weeks. After the mice were secured in a restrainer, the tail was wiped several times with 80% ethanol solution and their tail vein was punctured to obtain blood samples. Glucose and  $\beta$ -hydroxybutyrate were measured from the blood sample, using Freestyle Precision blood sugar monitor (Abott Diabetes Care, Wiesbaden, Germany). BW of mice was also assessed at the same time of blood withdrawal.

#### 6.5 Mixed myelinating co-cultures

The preparation was adapted from Thomson et al., 2006, Thomson et al., 2008. ThyAT mice were mated with C57BL6/N mice. Following confirmed-plugging procedure, defined as embryonic day 0.5 (E0.5), embryos were collected on embryonic day 13.5 (E13.5). The spinal cord was dissected and enzymatically dissociated by addition of 0.25% trypsin (Invitrogen). Enzymatic activity was stopped by further addition of plating medium (50% DMEM, 25% horse serum, 25% Hank's balanced salt solution without  $\text{Ca}^{2+}$ ,  $\text{Mg}^{2+}$ ) containing 2.5  $\mu\text{g/ml}$  DNase I (Sigma). Cells were then dissociated into cell suspension by triturating through 20- and 23-gauge needles and spun at 800 rpm for 5 min in 15 ml tubes. The pellet was resuspended in 1-2 ml of plating medium. Cells were initially plated at a density of  $1.5 \cdot 10^4$  cells/100  $\mu\text{l}$  onto poly-L-lysine (in boric acid buffer, pH 8.4)-coated coverslips, which were then placed into a 35-mm Petri dish. The cells were left to adhere for 2–3 h in a humidified atmosphere of 5%  $\text{CO}_2$  at 37 °C, after this time 200  $\mu\text{l}$  of differentiation medium was added. This medium contained DMEM (4.5 mg/l glucose), 10 mg/ml biotin, 0.5% hormone cocktail (1 mg/ml apotransferrin, 20 mM putrescine, 4  $\mu\text{M}$  progesterone and 6  $\mu\text{M}$  selenium), 50 nM hydrocortisone and 10  $\mu\text{g/ml}$  insulin (all reagents from Sigma). Cultures were maintained by replacing half of the medium with fresh medium three times per week. After 12 d in culture, cells were fed with differentiation medium with reduced concentration of insulin (0.2  $\mu\text{g/ml}$ ). Cultures were maintained for 25 days and cells were imaged between day in vitro DIV 26 and DIV 28.

## 6.6 HeLa cell line culture

For preliminary FLIM-imaging experiments, human cervical cancer cells (HeLa) were used. HeLa cells were kindly provided by Prof. Dr. Luis Pardo at MPI-EM as frozen stocks. Astrocytes were isolated by differential adhesion following dissociation from cerebral cortices of P0-2 rat pups as described previously (Barros et al., 2009; McCarthy and de Vellis, 1980). All cells were maintained at 37 °C and 7.5% CO<sub>2</sub> in their respective culturing media based on Dulbecco's modified Eagle's medium (Gibco, DMEM 1 g/L glucose [HeLa] or 4.5 g/L glucose [astrocytes], without glutamine) and supplemented with 10% fetal bovine serum (Gibco), 1% L-glutamine (Gibco GlutaMAX), and 1% antibiotics (penicillin-streptomycin, Gibco).

All cells were seeded at  $2.0 \cdot 10^4$ . Depending on their density, HeLa cells and primary astrocyte were transfected, 24-72 hours after seeding, with (per coverslip/reaction): 530 ng AT1.03<sup>YEMK</sup> plasmid DNA, diluted in 53 µl Opti-MEM by using 1.6 µl of Lipofectamine 2000 transfection reagent (Invitrogen) .

## 6.7 Optic nerve preparation and electrophysiological recordings

For optic nerve experiments mice were used in an age of 8 to 12 weeks. Optic nerves were excised from decapitated mice, placed into an interface Brain/Tissue Slice (BTS) chamber system (#65-0073; Harvard apparatus) and continuously superfused with artificial cerebrospinal fluid (aCSF). The perfusion chamber was continuously aerated by a humidified gas mixture of carbogen (95% O<sub>2</sub>/5% CO<sub>2</sub>) and experiments were performed at 37°C. The temperature in the chamber was maintained constant at 37 °C using a feedback-driven temperature controller (model TC-10, NPI electronic) connected to a temperature probe (TS-100-S; NPI electronic) inserted in the BTS incubation chamber.

The signal from a custom-made recording suction electrode was sent to a headstage (Heka Elektronik) and subsequently amplified 200 or 500 times, low-pass filtered at 30 kHz (defined by the preamplifier), and acquired at 100 kHz using an HEKA EPC9 double-patch clamp amplifier (Heka Elektronik). The signal amplification was obtained using serial amplification, by the Ext 10-2F amplifier module (10 fold; NPI electronic) and by the low-noise voltage preamplifier SR560 (20-50 fold amplification; Stanford Research System). The reference channel was recorded by an aCSF-filled glass capillary next to the recording suction electrode, in contact with the bathing aCSF. All glass capillaries

were purchased at World Precision Instruments (1.5 mm, #1B150-6). The suction electrodes were prepared by manually bending the glass capillaries on a Bunsen burner flame to an approximate angle of 40°. The opening was then adjusted to optic-nerve diameter by melting and polishing the tip of the glass capillary on the flame. Finally, 0.25 mm chlorided silver-wire (WPI) was inserted in the suction electrodes and solder to a gold pin to be connected to the battery anode and cathode wires (stimulation) and to the headstage (recording). Both suction electrodes were stabilized using heat-shrinking tubes and attached to the arms of two micromanipulators (Luigs & Neumann) that helped driving the electrodes to the optic nerve, laying inside the BTS incubation chamber. The optic nerve orientation in the suction electrodes followed the physiological sensory propagation, with the stimulated end being always at the proximal side (i.e. near retina) and the recorded end at the distal side (i.e. near the optic chiasm). The stimulating electrode, connected to the battery (Stimulus Isolator 385; WPI), delivered a supramaximal stimulus of 0.75 mA to the nerve evoking compound action potentials (CAP). The recording electrode was connected to the EPC9 amplifier.

The CAP, elicited by the maximum stimulation of 0.75 mA, was recorded at baseline stimulation frequency at 0.1 Hz. During HFS a burst-stimulation was applied, the burst consisted of 100 stimuli at the given frequency (16, 50 or 100 Hz), separated by 460 ms, during which the CAP response was recorded; HFS overall duration was kept constant at 150 seconds, independent of the frequency. RAMP stimulation consisted of 8 subsequent steps at 1, 4 (continuous), 7, 15, 25, 50, 75 and 100 (burst-like) Hz stimulation for a total duration time of 7.8 min. CAP recovery from HFS and RAMP was monitored at 0.2 Hz for 7.5 min.

## 6.8 Optic nerve imaging

Live imaging of ThyAT and GO-ATeam optic nerves was performed using an up-right confocal laser scanning microscope (Zeiss LSM 510 META/NLO) equipped with an Argon laser and a 63x objective (Zeiss 63x IR-Achroplan 0.9 W). The objective was immersed into the aCSF superfusing the optic nerve. Theoretical optical sections of 1.7  $\mu\text{m}$  over a total scanned area of 66.7  $\mu\text{m}$  x 66.7  $\mu\text{m}$  (512 x 512 pixels) of the optic nerve were obtained every 10.4 s in three channels for ThyAT. GO-ATeam signal was acquired over a larger area of 133.3  $\mu\text{m}$  x 133.3  $\mu\text{m}$  (512 x 512 pixels) For ThyAT the recorded channels are referred to as CFP (band pass 470-500 nm), FRET and YFP (long pass 530 nm). CFP and FRET channels were obtained by collecting photons using two PMT-detectors upon

458 nm excitation. Acceptor (YFP) fluorescence was obtained by excitation at 514 nm. For GO-ATeam the three channels are referred to as GFP (band pass 500-550 nm), FRET and OGR (band pass 565-615 nm). GFP and FRET channels were obtained after excitation at 488 nm and ORG following excitation at 543 nm.

The two excitation-scan events are referred to as "tracks". Track scan time was set at 1.3182 s for all experiment, as result of pixel dwell time equal to 2.5143  $\mu$ s and two-line scan averaging.

### **6.9 aCSF based solutions for optic nerve CAP/ ATP recording**

Optic nerves were superfused by aCSF containing (in mM): 124 NaCl, 3 KCl, 2 CaCl<sub>2</sub>, 2 MgSO<sub>4</sub>, 1.25 NaH<sub>2</sub>PO<sub>4</sub>, and 23 NaHCO<sub>3</sub>. aCSF was continuously bubbled with carbogen (95% O<sub>2</sub> / 5% CO<sub>2</sub>). aCSF control (or standard) solution is prepared with 10 mM glucose (Fluka BioChemika). Glucose was substituted with the appropriate energy substrates as indicated in each experiment. For glucose deprivation (GD), glucose was removed from the aCSF and substitute by sucrose (Merck Millipore) to maintain the correct osmolarity. For mitochondrial blockage (MB), aCSF containing 10 mM glucose was supplemented with 5 mM sodium azide (Merck Millipore). For the combination of MB + GD, glucose was substituted by sucrose and 5 mM sodium azide was added. For different

For HFS, aCSF was supplemented with different substrates and/or concentration. Glucose was used at three concentrations: 10 mM, 3.3 mM and 2 mM, and to maintain osmolarity constant sucrose was added accordingly (e.g. for 3.3 mM glucose aCSF, 6.7 mM sucrose were added). L-lactate and pyruvate (Sigma-Aldrich) were used at 10 mM. Inhibitors of lactate metabolism were added to a basal concentration of glucose of 3.3 mM: the MCT1 inhibitor AR-C155858 (Med Chem Express) was used at 10  $\mu$ M and all solutions were adjusted for DMSO (in which AR-C155858 was dissolved); sodium D-lactate (Sigma-Aldrich) was used at 20 mM in a low sodium (104 mM Na) aCSF control solution. In the HFS (16 Hz) stimulation using acetoacetate as energy substrate, glucose and sucrose (10 mM each, in the control solution) were replaced by 20 mM acetoacetate (sigma). For the ketone-body incubation the control solution had, in addition, 10 mM sucrose and was supplemented with glycogen phosphorolysis and debranching inhibitors 30  $\mu$ M 1,4-Dideoxy-1,4-imino-D-arabinitol hydrochloride (DAB, Sigma), 30  $\mu$ M 1-Deoxynojirimycin Hydrochloride (DNJ, Santa Cruz Biotech). Glucose and sucrose (10 mM each) were then replaced by 20 mM B-Hydroxybutyrate (Sigma).

## 6.10 Coverslip preparation

In order to fit cell preparation into the custom-made perfusion chamber for live-cell imaging, 30 mm diameter coverslips (Thermo Fisher Scientific, #1.5;  $0.17 \pm 0.01$  mm thickness) were used. To restrict the cell plating to the field of view of the chamber, the coverslips were endowed with a  $\varnothing$  13 mm silicone rings which reduced the plating surface to 132.73 mm<sup>2</sup>. Coverslips were treated with consecutive washes in nitric acid, distilled water and ethanol before the silicone rings were attached by negative vacuum pressure obtained by ethanol evaporation. Coverslips were successively autoclaved and coated with 10x poly-L-lysine in boric acid buffer before transfer into 35 mm petri dishes and usage. Cells were maintained in 250-300  $\mu$ l of their respective culturing medium

## 6.11 Solutions for ThyAT neuronal ATP imaging

Primary ATeam1.03<sup>YEMK</sup> expressing neurons in mixed cultures from ThyAT E13.5 embryos were imaged between day 26<sup>th</sup> and day 28<sup>th</sup>. Cells were pre-incubated for about 30 minutes to allow adaptation to the imaging AP buffer medium (in mM): HEPES 20.0, CaCl<sub>2</sub> 1.8, MgCl<sub>2</sub> 1.0, KCl 5.4, NaCl 110.0, Na<sub>2</sub>HPO<sub>4</sub> 0.8, glucose/lactate 20.0. For K<sup>+</sup> and Na<sup>+</sup> stimulation NaCl and KCl components of the medium were changed to reach the reported concentrations (K<sup>+</sup>: 1 or 20 mM; Na<sup>+</sup>: 146.6 or 165.6 mM). For glutamate stimulation 100  $\mu$ M glutamate (Sigma) and 100  $\mu$ M glycine (Sigma) were used. Ouabain (Sigma, 7.3 mg/mL in DMSO) was used to block Na/K ATPase at 100  $\mu$ M and other solutions were consequently corrected for DMSO (1  $\mu$ L per mL). Iodoacetic acid (AppliChem) was used as GAPDH inhibitor (i.e. glycolysis blocker (Schmidt & Dringen, 2009) at 1 mM. Azide (Merck) was used at 5 mM to inhibit ATP synthesis in the mitochondria (Bowler, Montgomery, Leslie, & Walker, 2006).

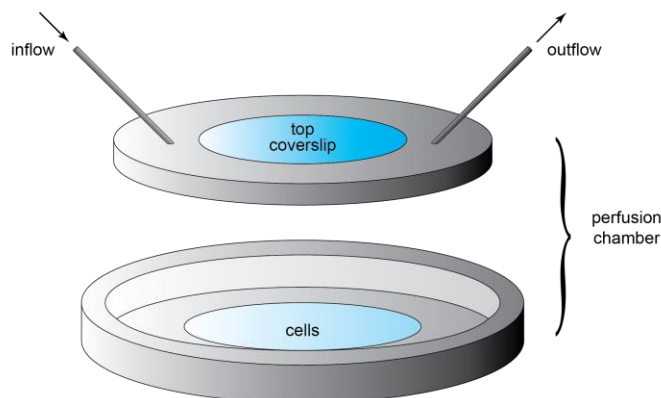


**Figure 34. Custom perfusion chamber for cell imaging.**

A thin volume of liquid constantly perfuses the cells by flowing between the bottom coverslip and the fixed coverslip on the chamber's lid. The perfusion chamber is a closed system where solutions circulate via gravity flow.

## 6.12 Solutions for FLIM calibration

The cells were put into a custom-built perfusion chamber (figure 34) connected to a gravity flow perfusion system (model VC-3/VM-8, ALA Scientific) 24-36 hours after transfection. The culturing medium was exchanged with imaging medium (in mM): NaCl 91.171, NaHCO<sub>3</sub> 17.856, HEPES 20.000, KCl 5.366, MgSO<sub>4</sub> 0.811, NaH<sub>2</sub>PO<sub>4</sub> 0.906, Na<sub>2</sub>HPO<sub>4</sub> 0.227, CaCl<sub>2</sub> 1.800 30-60 min before each imaging session to allow cells to adapt to the medium. The pH of the imaging medium was adjusted using 5 M NaOH solution to 7.40 at room temperature. To achieve cell permeabilization and ATP calibration, the following components were added to the imaging medium in different combination as specified in each calibration step: 6 μM digitonin/escin (Sigma-Aldrich), 5 mM azide (NaN<sub>3</sub>, Merck KGaA), 25 mM sucrose (Merck KGaA), 25 mM glucose (Merck KGaA) 250 μM ouabain (Sigma-Aldrich), and ATP (ATP Na<sub>2</sub> Sigma-Aldrich, variable concentrations).

## 6.13 FLIM imaging

Images were taken with an upright 2-photon microscope (TriM Scope II, LaVision BioTec). For excitation of the fluorophores a Titanium:Sapphire tunable laser (Chameleon Vision II, Coherent) was used. The excitation wavelength was set at 840 nm and emitted photons were collected via a 20 X objective (W Plan-Apochromat 20x/ 1.0 DIC CG = 0.17 M27 75 mm, FWD = 1.7 mm; Zeiss #421452-9880-000) using a band-pass filter 485/20 nm to monitor donor fluorescence only. Imaging was done at nominal laser intensity 1.8%, EOM 100%, unless otherwise noted. The laser has a pulse length of 140 fs and a repetition rate of 78 MHz, which limits the duration of a single measurement to a

maximum of 12.8  $\mu$ s. The actual measurement length is 11.95 ns. Images were taken a pixel dwell time of 9.21 ns. Line averaging of 3 was used.

The emitted photons were directed by a silver mirror via the band-pass filter 485/20 to a 16 channel PMT-array for time-correlated single-photon counting (TCSPC) (FLIM X16 TCSPC detector, LaVision BioTec). The FLIM detector has a total counting rate of 76 MHz with a dead time of 5.5 ns (per channel). The nominal temporal bin size in the histogram is 80 ps. The temporal resolution of the detector electronics was determined to be  $\sim$  110 ps (full-width half-maximum of IRF). The IRF was measured taking advantage of the second harmonic generation (SHG) phenomena through excitation at 840 nm of dextrose crystals (sugar cubes) in order to generate a very fast SHG signal, recorded at half-wavelength (BP filter 420/10 nm). The imaging parameters were kept constant in all other measurements (unless otherwise noted). In order to avoid pile-up effects, which are responsible for introducing artefactual shortening of the measured lifetime due to a combination of increased number of events (photons) happening during detector dead-time, we followed the manufacturer recommendation and kept the MAX count/ pixel dwell time ratio  $\leq$  35. Preliminary tests were performed with a Rhodamine-101 sample, in order to compare  $T$  to the benchmark value of 4.0 ns (value measured at the LaVision setup was 3.9 ns).

For ratiometry the mirror was replaced by a 495 nm beam splitter. The signal was directed onto two gallium arsenide phosphide photomultiplier tubes (GaAsP PMT) which recorded the YFP and CFP signals, respectively.

All FLIM-imaging experiments were performed at room temperature, unless differently noted.

## **6.14 In vivo imaging**

### **6.14.1 Anesthesia and pain management during the postoperative phase**

For surgical procedure we used a completely reversible anesthesia (in German: Vollantagonisierbare Anästhesie or VAA). VAA combines three different drugs with some overlapping sedative effects, in the attempt to reduce undesired side effects: Medetomidine, Midazolam and Fentanyl (MMF; Fleischmann et al., 2016). Medetomidine is an  $\alpha_2$ -adrenoreceptor agonist, produces dose-dependent sedation and analgesia: the stimulation of  $\alpha_2$ -adrenoreceptor in the CNS leads to GABA release and decreased release of acetylcholine. The analgesic potency of medetomidine is

caused by an inhibition of the spinal nociceptive reflexivity. Midazolam is a member of the substance group of the benzodiazepines. It has an anxiolytic and relaxing effect, and it blocks convulsion. Fentanyl is a strong opioid agonist providing very potent but short analgesic effects. With the exception of metamizol, all anesthetics and drugs were prepared by mixing each active pharmaceutical ingredient (API) in sterile saline solution (i.e. excipient, 0.9% NaCl) to reach 1 ml of volume per 100 g of body weight (BW). After the BW of the mouse was assessed (typically between 20-30 g), MMF was injected IP at 0.1  $\mu$ l per 10 g. MMF was prepared according to the following scheme:

<b>API</b>	<b>mg/ml stock</b>	<b>dosage mg per 100 gr BW</b>	<b><math>\mu</math>l/ 100 g BW</b>
Fentanyl	0.05	0.005	100.000
Midazolam	5	0.5	100.000
Medetomidine	1	0.05	50.000
0.9% NaCl			750.000

MMF anesthesia can be antagonized by atipamezole and flumazenil (AF). Atipamezole displaces medetomidine from the  $\alpha_2$ -adrenoreceptor, thus antagonizing its effects. Similarly, flumazenil is a highly selective antagonists of GABA<sub>A</sub> receptors, and is used to reverse benzodiazepine (midazolam) effects. Finally, naloxone has an antagonistic effect on opioid receptors, it was prepared for mice that could show side effects due to fentanyl overdose (e.g. respiratory depression). AF was injected at 0.1  $\mu$ l per 10 g of BW at the end of the surgical procedure. It was mixed as follows:

<b>API</b>	<b>mg/ml stock</b>	<b>dosage mg per 100 gr BW</b>	<b><math>\mu</math>l/ 100 g BW</b>
Atipamezole	5	0.25	50.000
Flumazenil	0.1	0.05	500.000
Naloxone	0.4	0.12	300.000
0.9% NaCl		to 1 mL	450.000
0.9% NaCl (Naloxone)		to 1 mL	150.000



Buprenorphine is a partial opiate agonist, and was also administered to the mice at the end of the surgical procedure via IP injection to provide acute pain relief in the postop. Buprenorphine has a duration of action in the range of 24 hours. Buprenorphine was mixed as follows:

<b>API</b>	<b>mg/ml stock</b>	<b>dosage mg per 100 gr BW</b>	<b>μl/ 100 g BW</b>
Buprenorphine	0.33	0.01	30.303
0.9% NaCl			969.697

Metamizol was given to the mice as pain killer for 3 days after the surgery. A solution 0.2 % glucose and 5 g/L of metamizol was prepared to replace the drinking water, as well as to soak the food-pellet into a petri dish positioned on the bottom of the cage. The solution in the water bottle and the food were replaced daily.

<b>API</b>	<b>mg/ml stock</b>	<b>dosage mg per 100 mL 0.2% glc solution</b>	
Metamizol	500	500	1 mL in 99 mL of 11.2 mM glc solution sterile
	<b>g · mol<sup>-1</sup></b>	<b>Concentration in dH<sub>2</sub>O</b>	<b>g/L</b>
Glucose(H <sub>2</sub> O)	198.17	11.21 mM	2.2222

The mice were kept on a moist tissue placed on top of a polyester heating foil (Conrad electronics) during the surgery and the temperature was monitored via a thermometer probe placed between the animal and the heated plate. To track the anesthesia, animal's heart rate, breathing, arterial oxygen saturation and pulse distension were also monitored via the oximeter MouseOx Plus (Starr Life Sciences Corp.).

### **6.14.2 Surgery**

After IP injection with MMF the animal's reflexes were tested via tail and paw pinch every 3-5 minutes from the moment the animal fell asleep. After no reflex could be observed the animal was injected with 1 mL of saline solution IP. The mouse was shaved in the dorsal area and the skin was dabbed with paper-tissue soaked with 80% ethanol. The mouse's vital parameter were continuously monitored via the oximeter after being transferred on a heated plate. After the incision, the muscles and the transverse ligaments were separated from the side of the three thoracic vertebrae T11-T13. Two steel clamps were then positioned on the side of the exposed vertebrae and T12 laminectomy was performed using a micro-drill (World Precision Instruments) equipped with a carbide spherical ball mill 0.5 mm diameter (#1/4 Circuitmedic). The steel top plate was then anchored to the side bars with steel screws. The hollow space between the spinal cord tissue and the top plate was filled with transparent silicone (Kwik-Sil, World Precision Instruments #600022). A 5 mm round coverslip (Thermofisher) was rapidly placed on top of the silicone to provide a flat imaging surface. The skin above and below the implant was sutured using non-absorbable silk (Silkam DS12, B. Braun #0762067). The steel implant was sealed to the skin using self-curing dental acrylic. At the end of the procedure the mouse was injected with AF and buprenorphine and placed in a new cage to recover and monitored for the following week.

### **6.14.3 Imaging**

Imaging was performed at the upright 2-photon microscope (TriM Scope II, LaVision BioTec). Following MMF anesthesia the mice were placed on a custom holder which locks the steel implant on the top plate. The holder was transferred on a custom chamber heated via a self-adhesive polyester heating foil (Conrad Electronic) attached to a 12V power supply. The chamber was in turn locked on a custom stage that replaced the manufacturer's one. The holder was adjusted on the z-axis to position the mouse at the correct distance between the objective and the heated chamber. The holder was made to coarsely rotate around the x-axis and the y-axis to best position the implant in the center of the objective. Fine x-y movements were obtained by the motorized x-y table. The mouse body-core was lifted from the chamber and the front and rear limbs were fixed to the steel

holder via rubber bands to distribute the weight. The chamber was finally closed by three Plexiglas walls that helped to keep the heath confined around the animal.

For excitation of the fluorophores a Titanium:Sapphire tunable laser (Chameleon Vision II, Coherent) was used. The excitation wavelength was set at 840 nm and emitted photons were collected via a 20X objective (W Plan-Apochromat 20x/ 1.0, FWD = 1.7 mm) and separated by their  $\lambda$  with a 495 nm beam splitter which reflected with a 45° angle the  $\lambda \leq 495$  nm. The separated light-beam were then directed towards two gallium arsenide phosphide photomultiplier tubes (GaAsP PMTs) which recorded the YFP and CFP signals. CFP signal was further filtered by a CFP 485/20 BP filter positioned in front of the detector. Unless differently noted, images were acquired using a pixel size of 0.494  $\mu\text{m}$  and dwell time of 9.29  $\mu\text{s}$ .

## **6.15 Data analysis**

### **6.15.1 CAP**

Optic nerve function was monitored quantitatively as the area under the supramaximal CAP. CAP responses were acquired using an HEKA EPC9 double-patch clamp amplifier (Heka Elektronik), following 200 or 500 fold amplification and low pass filtering at 30 KHz (defined in the preamplifier). All the waveforms were converted using the PatchMaster software (provided by the manufacturer) into '.mat' format and loaded into a custom script where CAP area is calculated as the area under the waveform (AUW) and plotted against time (cf. appendix §1). The integration of AUW is done in a range of approximately 1.5 ms, defined by the beginning of the response (typically at 0.2 ms after the stimulus artifact) and by the lowest point that marked the end of the second peak of the curve, characteristic of the optic nerve evoked CAP. The CAP area is considered to be proportional to the total number of excited axons and represents a convenient and reliable means of monitoring optic nerve axon function (Saab et al., 2016; Stys, Ransom, & Waxman, 1991). Data were normalized to the mean obtained during the initial 15 min (defined as baseline, i.e. no experimental condition applied). Results from several nerves were pooled, averaged, and plotted against time.

### 6.15.2 ATP

The relative amount of ATP in the optic nerve was calculated in two steps. Initially, the mean intensity of FRET and donor (CFP for ATeam1.03<sup>YEMK</sup> and GFP for GO-ATeam) channel were extracted from the imaging time-series (in Fiji-ImageJ) and the ratio F/C or F/G was calculated. All fibers visible in the field of view were included with in the analysis without any prior selection. The ratio (F/C or F/G) was then normalized to zero using the F/C or F/G value obtained by application of MB + GD at the end of each experiment, i.e. by depleting all axons from ATP. Furthermore, F/C and F/G values obtained during baseline recordings in 10 mM glucose at the beginning of each experiment were set to one. In order to separate the ATeam1.03<sup>YEMK</sup> signal of small and large caliber fibers a custom macro for FIJI was used (cf. appendix §2): the macro generates a processed time-series stack to first increase the intensity signal-to-noise by consecutively: multiply all the available channel, remove outliers, smooth and finally apply a gaussian-blur filtering. The newly generated time-series is then used to align all images using the 'Register Virtual Stack Slices' and 'Transform Virtual Stack Slices' FIJI plugins (ImageJ plugins are available at: [http://imagej.net/Register\\_Virtual\\_Stack\\_Slices](http://imagej.net/Register_Virtual_Stack_Slices) and [http://imagej.net/Transform\\_Virtual\\_Stack\\_Slices](http://imagej.net/Transform_Virtual_Stack_Slices)). The registered stack is then thresholded based on the average stack-intensity and used as a mask to separate, in each channel, the large and small axons. Intensities are then calculated and imported in excel to further process the signals by calculating the FRET/CFP normalized ratio as described above.

### 6.15.3 ATP & CAP parameters

For GD, MB, B-HB, HFS, RAMP and MB + GD conditions,  $m$  coefficients for the slope-intercepts at the point of maximal change of the ATeam1.03<sup>YEMK</sup> signal were used to calculate the CAP and ATP rate per second, during the initial decay and the recovery following either reperfusion with aCSF containing 10 mM glucose or following return to baseline stimulation at 0.2 Hz. The time of the start of decay/recovery of the ATP and CAP curves were defined as the first time-point at which the slope-intercept of the signal was above a threshold value based on the standard deviation calculated at the baseline. For HFS, RAMP analysis three parameters were considered for both CAP and ATP: 1) the overall amplitude obtained by averaging the data at the time points within the last 15 s of the stimulation 2) the rate of initial decay defined within the 45 seconds that followed the

beginning of the stimulation 3) the rate of recovery defined within the 60 seconds that followed the end of the stimulation. Rates were calculated from the  $m$  coefficients for the slope-intercepts in the defined time-range.

#### 6.15.4 FLIM

Single-time-point measurements were saved as .tif image stacks with the third axis representing TCSPC time: each stack contained 109 images, each representing single temporal bins that described the fluorescence decay. In order to subtract background, the third axis of each stack was squeezed (projected) into a 2D plane and then thresholded to remove background noise and high-intensity signals correlated to lifetime shortening due to pile-up. The thresholded stacks were converted to 8-bit masks of 0/255 value. For each given timepoint the 3D data containing TCSPC information, was multiplied by the corresponding mask. These operations were performed via a custom-made Fiji macro (cf. appendix §3-4). The background-cleared image stacks were finally uploaded into MATLAB® where we used a MATLAB script modified from that kindly provided by Dr. Ingo Gregor (Georg-August-Universität Göttingen, Enderlein group) which applies a deconvolution algorithm and was modified to iterate through the entire time-series and through several ROIs obtained and saved as x, y coordinates using ImageJ (cf. appendix §4). At each time point and for each ROI, the script applies a double-exponential decay scheme. The script outputs the amplitude-weighted lifetimes calculated as

$$T_{aw} = \frac{\sum(A_i \cdot \tau_i)^2}{\sum A_i \cdot \tau_i}$$

and plotted against time.

#### 6.16 Western blot and quantification

##### Optic nerve lysate preparation

A total protein preparation of MCT1<sup>het</sup> optic nerves was prepared by homogenizing both optic nerves including the chiasma in 500 µl RIPA-buffer (150 mM NaCl, 50 mM Tris/HCl, pH 6.8, 1% [v/v] Triton X-100, 0.5% [w/v] sodiumdeoxycholate, 0.5% [w/v] SDS and Roche complete protease inhibitor (Roche)) using a Precellys 24 homogenizer (Bertin technologies) equipped with Soft tissue homogenizing CK14 tubes (Bertin technologies) by 3 cycles at 6500 rpm for 10 s with intermittent

cooling of the samples on ice. Debris was removed by centrifugation for 5 min at 17000 G at 4 °C and samples were frozen at -80 °C prior to analysis. Mice were analyzed at an age of eight weeks. Protein concentration was determined using the DC Protein assay (Biorad) according to the manufacturer's instructions.

Western blot analysis was kindly performed by Dr. Kathrin Kusch - Neurogenetics department, Max-Planck Institute for Experimental Medicine.

### **6.16.1 Immunoblotting**

Immunoblotting was performed as described before (Werner et al., 2007). Briefly, 20µg protein sample in sample buffer containing 2%[w/v] LDS, 0.5%[v/v] Triton X-100 and 0.5%[w/v] sodiumdeoxycholate were separated on 12% polyacrylamide-SDS-gels in Laemmli-buffer. For immunoblotting, proteins were blotted onto polyvinylidene difluoride membranes (PVDF, Roche), blocked with 5% [w/v] skim milk in TBST (150mM NaCl, 10mM Tris/HCl, pH 7.4, 0.05%[v/v] Tween 20) and incubated with primary antibodies diluted in the same solution for 48h at 4°C. After washing with TBST, blots were incubated with horse radish peroxidase coupled secondary antibodies (Dianova), washed with TBST and developed by enhanced chemiluminescence (Western Lightning ECL, Perkin Elmer) using a luminescence imager (Intas). The antiserum specific for MCT1 was raised in rabbit using a synthetic peptide located at a conserved intracellular loop of MCT1 (SLC16a1; NH<sub>2</sub>-CDANTDLIGGSPKGEKL-CONH<sub>2</sub>). Antibodies were purified by affinity chromatography to the immunizing peptide and used in a final concentration of 180 pg/ml. For quantification of MCT1 amount, 16-bit tiff images obtained from the luminescence imager were analyzed in ImageJ by densitometry using the "gels" plugin. Signal intensities for MCT1 were normalized to mean signal intensity for MCT1 of the wild type samples.

To determine equal protein loading, gels prepared with the same samples were stained with colloidal coomassie. Briefly, gels were fixed subsequent to electrophoresis in 50% [v/v] ethanol, 10% [v/v] acetic acid for 1h at room temperature, washed twice in distilled water for 15min and stained with colloidal coomassie (0.08% [w/v] Coomassie Brilliant Blue G250, 1.6% [v/v] ortho-phosphoric acid, 8% [w/v] ammonium sulfate, 20% [v/v] methanol] over night at room temperature. Gels were washed several times in distilled water and documented using a transmitted light scanner.

Immunoblot analysis was kindly performed by Dr. Kathrin Kusch - Neurogenetics department, Max-Planck Institute for Experimental Medicine.

### 6.17 Electron microscopy

PLP<sup>KO</sup> mice were sacrificed by cervical dislocation and their optic nerves carefully removed. The nerves were cut in half and placed in an aluminum specimen carrier submerged in a solution of 20% PVP (polyvinylpyrrolidone, MW = 10`000 from Sigma) in PBS. After adjusting the level of liquid in the carrier, a second carrier was placed on top as a lid. Then the complete assembly was immediately transferred into the high-pressure-freezer (HPM100, Leica, Vienna, Austria) and frozen with liquid nitrogen. Subsequent freeze-substitution was carried out using a Leica AFS II (Leica, Vienna, Austria) as follows: Samples were first kept in tannic acid (0.1% in acetone) at  $-90\text{ }^{\circ}\text{C}$  for 100h, washed with acetone (4 x 30 min,  $-90\text{ }^{\circ}\text{C}$ ), and then transferred into OsO<sub>4</sub> (EMS; 2% in acetone,  $-90\text{ }^{\circ}\text{C}$ ). The temperature was raised from  $-90\text{ }^{\circ}\text{C}$  to  $-20\text{ }^{\circ}\text{C}$  in increments of  $5\text{ }^{\circ}\text{C}/\text{h}$ , then kept unaltered at  $-20\text{ }^{\circ}\text{C}$  for 16 hours, and then raised from  $-20\text{ }^{\circ}\text{C}$  to  $+4\text{ }^{\circ}\text{C}$  in increments of  $10\text{ }^{\circ}\text{C}/\text{h}$ . Then samples were washed with acetone (3 x 30 min at  $4\text{ }^{\circ}\text{C}$ ), allowed to adjust to room temperature (1 hour), and finally transferred into Epon (Serva) (50% Epon in acetone for 3 hours, 90% Epon in acetone for 18 hours, 100% Epon for 6 hours). The samples were placed in an embedding mold and polymerized ( $60\text{ }^{\circ}\text{C}$ , 24 hours). Ultrathin sections (50 nm) were cut using a Leica Ultracut S ultramicrotome (Leica, Vienna, Austria) and stained with an aqueous solution of 2% uranyl acetate (Merck, Darmstadt, Germany). The sections were viewed in a LEO EM 912AB electron microscope (Zeiss, Oberkochen, Germany) and pictures were taken with an on-axis 2048x2048-CCD-camera (TRS, Moorenweis, Germany).

Transmission electron microscopy imaging was kindly performed by Dr. Wiebke Möbius - Neurogenetics department, Max-Planck Institute for Experimental Medicine.

### 6.18 Presentation of data

All data are presented either as mean  $\pm$  SEM. or as stripe plots showing all data points and the mean (line within the plot). If not indicated otherwise in the figure legends, data was statistically evaluated using Welch's t-test and assuming a normal distribution (\*  $p < 0.05$ ; \*\*  $p < 0.01$ ; \*\*\*  $p < 0.001$ ).

### **6.19 Analysis scripts**

Scripts to analyze data were written in MATLAB<sup>®</sup> as well as in ImageJ (FIJI). The scripts were used to process and analyze the CAP (MATLAB, appendix §1), the ATeam1.03<sup>YEMK</sup> FRET-LSM imaging timeseries (ImageJ, appendix §2) and the FLIM data (ImageJ and MATLAB<sup>®</sup>, appendix §3-4). The MATLAB script to analyze FLIM data was modified from the one kindly provided by Dr. Ingo Gregor (Third Institute of Physics – Enderlein Lab).



## 7 Reference list

- Attwell, D., & Laughlin, S. B. (2001). An Energy Budget for Signaling in the Grey Matter of the Brain. *Journal of Cerebral Blood Flow & Metabolism*, *21*(10), 1133–1145. <https://doi.org/10.1097/00004647-200110000-00001>
- Bajar, B. T., Wang, E. S., Zhang, S., Lin, M. Z., & Chu, J. (2016). A guide to fluorescent protein FRET pairs. *Sensors (Switzerland)*, *16*(9), 1–24. <https://doi.org/10.3390/s16091488>
- Bak, L. K., Walls, A. B., Schousboe, A., Ring, A., Sonnewald, U., & Waagepetersen, H. S. (2009). Neuronal glucose but not lactate utilization is positively correlated with NMDA-induced neurotransmission and fluctuations in cytosolic Ca<sup>2+</sup> levels. *Journal of Neurochemistry*, *109*(SUPPL. 1), 87–93. <https://doi.org/10.1111/j.1471-4159.2009.05943.x>
- Barros, L. F., Bolaños, J. P., Bonvento, G., Bouzier-Sore, A.-K., Brown, A., Hirrlinger, J., ... Weber, B. (2017). Current technical approaches to brain energy metabolism. *Glia*. <https://doi.org/10.1002/glia.23248>
- Barros, L. F., San Martín, A., Ceballo, S., Ruminot, I., Lerchundi, R., Frommer, W. B., & Barros, L. F. (2013). A Genetically Encoded FRET Lactate Sensor and Its Use To Detect the Warburg Effect in Single Cancer Cells. *PLoS ONE*, *8*(2), e57712. <https://doi.org/10.1371/journal.pone.0057712>
- Barros, L. F., San Martín, A., Sotelo-Hitschfeld, T., Lerchundi, R., Fernández-Moncada, I., Ruminot, I., ... Espinoza, D. (2013). Small is fast: astrocytic glucose and lactate metabolism at cellular resolution. *Frontiers in Cellular Neuroscience*, *7*(March), 27. <https://doi.org/10.3389/fncel.2013.00027>
- Beis, I., & Newsholme, E. A. (1975). The contents of adenine nucleotides, phosphagens and some glycolytic intermediates in resting muscles from vertebrates and invertebrates. *The Biochemical Journal*, *152*(1), 23–32. <https://doi.org/10.1042/bj1520023>
- Beltrán, F. A., Acuña, A. I., Miró, M. P., Angulo, C., Concha, I. I., Castro, M. A., ... Castro, M. A. (2011). Ascorbic acid-dependent GLUT3 inhibition is a critical step for switching neuronal metabolism. *Journal of Cellular Physiology*, *226*(12), 3286–3294. <https://doi.org/10.1002/jcp.22674>
- Berg, J., Hung, Y. P., & Yellen, G. (2009). A genetically encoded fluorescent reporter of ATP:ADP ratio. *Nature Methods*, *6*(2), 161–6. <https://doi.org/10.1038/nmeth.1288>
- Bergles, D. E., Roberts, J. D. B., Somogyi, P., & Jahr, C. E. (2000). Glutamatergic synapses on oligodendrocyte precursor cells in the hippocampus. *Nature*, *405*(6783), 187–191. <https://doi.org/10.1038/35012083>
- Boison, D., & Stoffel, W. (1994). Disruption of the compacted myelin sheath of axons of the central nervous system in proteolipid protein-deficient mice. *Proceedings of the National Academy of Sciences*, *91*(24), 11709–11713. <https://doi.org/10.1073/pnas.91.24.11709>

- Bowler, M. W., Montgomery, M. G., Leslie, A. G. W., & Walker, J. E. (2006). How azide inhibits ATP hydrolysis by the F-ATPases. *Proceedings of the National Academy of Sciences of the United States of America*, *103*(23), 8646–8649. <https://doi.org/10.1073/pnas.0602915103>
- Brown, A. M., Baltan Tekkök, S., & Ransom, B. R. (2004). Energy transfer from astrocytes to axons: the role of CNS glycogen. *Neurochemistry International*, *45*(4), 529–36. <https://doi.org/10.1016/j.neuint.2003.11.005>
- Brown, A. M., & Ransom, B. R. (2007). Astrocyte glycogen and brain energy metabolism. *Glia*, *55*(12), 1263–71. <https://doi.org/10.1002/glia.20557>
- Brown, A. M., Sickmann, H. M., Fosgerau, K., Lund, T. M., Schousboe, A., Waagepetersen, H. S., & Ransom, B. R. (2005). Astrocyte glycogen metabolism is required for neural activity during aglycemia or intense stimulation in mouse white matter. *Journal of Neuroscience Research*, *79*(1–2), 74–80. <https://doi.org/10.1002/jnr.20335>
- Brown, A. M., Tekkök, S. B., & Ransom, B. R. (2003). Glycogen regulation and functional role in mouse white matter. *The Journal of Physiology*, *549*(Pt 2), 501–12. <https://doi.org/10.1113/jphysiol.2003.042416>
- Brown, A. M., Wender, R., & Ransom, B. R. (2001). Metabolic substrates other than glucose support axon function in central white matter. *Journal of Neuroscience Research*, *66*(5), 839–843. <https://doi.org/10.1002/jnr.10081>
- Caroni, P. (1997). Overexpression of growth-associated proteins in the neurons of adult transgenic mice. *Journal of Neuroscience Methods*, *71*(1), 3–9. [https://doi.org/10.1016/S0165-0270\(96\)00121-5](https://doi.org/10.1016/S0165-0270(96)00121-5)
- Castro, M. A., Beltrán, F. A., Brauchi, S., & Concha, I. I. (2009). A metabolic switch in brain: glucose and lactate metabolism modulation by ascorbic acid. *Journal of Neurochemistry*, *110*(2), 423–440. <https://doi.org/10.1111/j.1471-4159.2009.06151.x>
- Castro, M. A., Pozo, M., Cortés, C., García, M. D. L. A., Concha, I. I., & Nualart, F. (2007). Intracellular ascorbic acid inhibits transport of glucose by neurons, but not by astrocytes. *Journal of Neurochemistry*, *102*(3), 773–782. <https://doi.org/10.1111/j.1471-4159.2007.04631.x>
- Cooper, G. M., & Hausman, R. E. (2007). *The Cell: A Molecular Approach 2nd Edition*. Sinauer Associates.
- D'Agostino, D. P., Putnam, R. W., & Dean, J. B. (2007). Superoxide ( $\cdot\text{O}_2^-$ ) Production in CA1 Neurons of Rat Hippocampal Slices Exposed to Graded Levels of Oxygen. *Journal of Neurophysiology*, *98*(2), 1030–1041. <https://doi.org/10.1152/jn.01003.2006>
- De Biase, L. M., Nishiyama, A., & Bergles, D. E. (2010). Excitability and synaptic communication within the oligodendrocyte lineage. *The Journal of Neuroscience*, *30*(10), 3600–11. <https://doi.org/10.1523/JNEUROSCI.6000-09.2010>

- Díaz-García, C. M., Mongeon, R., Lahmann, C., Koveal, D., Zucker, H., & Yellen, G. (2017). Neuronal Stimulation Triggers Neuronal Glycolysis and Not Lactate Uptake. *Cell Metabolism*, *26*(2), 361–374.e4. <https://doi.org/10.1016/j.cmet.2017.06.021>
- Dienel, G. A. (2012). Brain Lactate Metabolism: The Discoveries and the Controversies. *Journal of Cerebral Blood Flow & Metabolism*, *32*(7), 1107–1138. <https://doi.org/10.1038/jcbfm.2011.175>
- Duncan, I. D., Hammang, J. P., Goda, S., & Quarles, R. H. (1989). Myelination in the jimpy mouse in the absence of proteolipid protein. *Glia*, *2*(3), 148–54. <https://doi.org/10.1002/glia.440020303>
- Edgar, J. M., McLaughlin, M., Yool, D., Zhang, S.-C. C., Fowler, J. H., Montague, P., ... Griffiths, I. R. (2004). Oligodendroglial modulation of fast axonal transport in a mouse model of hereditary spastic paraplegia. *Journal of Cell Biology*, *166*(1), 121–131. <https://doi.org/10.1083/jcb.200312012>
- Farrar, M. J., Bernstein, I. M., Schlafer, D. H., Cleland, T. A., Fetcho, J. R., & Schaffer, C. B. (2012). Chronic in vivo imaging in the mouse spinal cord using an implanted chamber. *Nature Methods*, *9*(3), 297–302. <https://doi.org/10.1038/nmeth.1856>
- Farrar, M. J., & Schaffer, C. B. (2014). A procedure for implanting a spinal chamber for longitudinal in vivo imaging of the mouse spinal cord. *Journal of Visualized Experiments: JoVE*, (94), 1–9. <https://doi.org/10.3791/52196>
- Fehr, M., Lalonde, S., Lager, I., Wolff, M. W., & Frommer, W. B. (2003). In vivo imaging of the dynamics of glucose uptake in the cytosol of COS-7 cells by fluorescent nanosensors. *Journal of Biological Chemistry*, *278*(21), 19127–19133. <https://doi.org/10.1074/jbc.M301333200>
- Ferreirinha, F., Quattrini, A., Pirozzi, M., Valsecchi, V., Dina, G., Broccoli, V., ... Rugarli, E. I. (2004). Axonal degeneration in paraplegin-deficient mice is associated with abnormal mitochondria and impairment of axonal transport. *Journal of Clinical Investigation*, *113*(2), 231–242. <https://doi.org/10.1172/JCI200420138>
- Fields, R. D. (2011). Nonsynaptic and nonvesicular ATP release from neurons and relevance to neuron–glia signaling. *Seminars in Cell & Developmental Biology*, *22*(2), 214–219. <https://doi.org/10.1016/j.semcdb.2011.02.009>
- Figley, C. R., & Stroman, P. W. (2011). The role(s) of astrocytes and astrocyte activity in neurometabolism, neurovascular coupling, and the production of functional neuroimaging signals. *European Journal of Neuroscience*. <https://doi.org/10.1111/j.1460-9568.2010.07584.x>
- Fleischmann, T., Jirkof, P., Henke, J., Arras, M., & Cesarovic, N. (2016). Injection anaesthesia with fentanyl–midazolam–medetomidine in adult female mice: importance of antagonization and perioperative care. *Laboratory Animals*, *50*(4), 264–274. <https://doi.org/10.1177/0023677216631458>

- Foo, K., Blumenthal, L., & Man, H.-Y. (2012). Regulation of neuronal bioenergy homeostasis by glutamate. *Neurochemistry International*, *61*(3), 389–396. <https://doi.org/10.1016/j.neuint.2012.06.003>
- Fünfschilling, U., Supplie, L. M., Mahad, D., Boretius, S., Saab, A. S., Edgar, J., ... Nave, K.-A. (2012). Glycolytic oligodendrocytes maintain myelin and long-term axonal integrity. *Nature*, *485*(7399), 517–21. <https://doi.org/10.1038/nature11007>
- Ganesan, S., Ameer-Beg, S. M., Ng, T. T. C., Vojnovic, B., & Wouters, F. S. (2006). A dark yellow fluorescent protein (YFP)-based Resonance Energy-Accepting Chromoprotein (REACH) for Forster resonance energy transfer with GFP. *Proceedings of the National Academy of Sciences*, *103*(11), 4089–4094. <https://doi.org/10.1073/pnas.0509922103>
- Gardner, P. R., & Fridovich, I. (1993). Effect of Glutathione on Aconitase in Escherichia coli. *Archives of Biochemistry and Biophysics*, *301*(1), 98–102. <https://doi.org/https://doi.org/10.1006/abbi.1993.1120>
- Griffiths, I. (1998). Axonal Swellings and Degeneration in Mice Lacking the Major Proteolipid of Myelin. *Science*, *280*(5369), 1610–1613. <https://doi.org/10.1126/science.280.5369.1610>
- Griffiths, I., Klugmann, M., Anderson, T., Thomson, C., Vouyiouklis, D., & Nave, K. A. (1998). Current concepts of PLP and its role in the nervous system. *Microscopy Research and Technique*, *41*(5), 344–358. [https://doi.org/10.1002/\(SICI\)1097-0029\(19980601\)41:5<344::AID-JEMT2>3.0.CO;2-Q](https://doi.org/10.1002/(SICI)1097-0029(19980601)41:5<344::AID-JEMT2>3.0.CO;2-Q)
- Gruenenfelder, F. I., Thomson, G., Penderis, J., & Edgar, J. M. (2011). Axon-glia interaction in the CNS: what we have learned from mouse models of Pelizaeus-Merzbacher disease. *Journal of Anatomy*, *219*(1), 33–43. <https://doi.org/10.1111/j.1469-7580.2011.01363.x>
- Halestrap, A. P. (2012). The monocarboxylate transporter family--Structure and functional characterization. *IUBMB Life*, *64*(1), 1–9. <https://doi.org/10.1002/iub.573>
- Haller, M., Mironov, S. L., & Richter, D. W. (2001). Intrinsic optical signals in respiratory brain stem regions of mice: neurotransmitters, neuromodulators, and metabolic stress. *Journal of Neurophysiology*, *86*(1), 412–21. <https://doi.org/10.1152/jn.2001.86.1.412>
- Harris, J. J., & Attwell, D. (2012). The energetics of CNS white matter. *The Journal of Neuroscience*, *32*(1), 356–71. <https://doi.org/10.1523/JNEUROSCI.3430-11.2012>
- Hartline, D. K., & Colman, D. R. (2007). Rapid Conduction and the Evolution of Giant Axons and Myelinated Fibers. *Current Biology*, *17*(1), 29–35. <https://doi.org/10.1016/j.cub.2006.11.042>
- Hirrlinger, J., & Nave, K.-A. (2014). Adapting brain metabolism to myelination and long-range signal transduction. *Glia*, *62*(11), 1749–1761. <https://doi.org/10.1002/glia.22737>

- Hirrlinger, P. G., Scheller, A., Braun, C., Quintela-Schneider, M., Fuss, B., Hirrlinger, J., & Kirchhoff, F. (2005). Expression of reef coral fluorescent proteins in the central nervous system of transgenic mice. *Molecular and Cellular Neuroscience*, *30*(3), 291–303. <https://doi.org/10.1016/j.mcn.2005.08.011>
- Hornig, D. (1975). DISTRIBUTION OF ASCORBIC ACID, METABOLITES AND ANALOGUES IN MAN AND ANIMALS. *Annals of the New York Academy of Sciences*, *258*(1), 103–118. <https://doi.org/10.1111/j.1749-6632.1975.tb29271.x>
- Hung, Y. P., Albeck, J. G., Tantama, M., & Yellen, G. (2011). Imaging cytosolic NADH-NAD(+) redox state with a genetically encoded fluorescent biosensor. *Cell Metabolism*, *14*(4), 545–554. <https://doi.org/10.1016/j.cmet.2011.08.012>
- Imamura, H., Huynh, K. P., Togawa, H., Saito, K., Iino, R., Kato-Yamada, Y., ... Noji, H. (2009). Visualization of ATP levels inside single living cells with fluorescence resonance energy transfer-based genetically encoded indicators. *Proceedings of the National Academy of Sciences of the United States of America*, *106*(37), 15651–15656. <https://doi.org/10.1073/pnas.0904764106>
- Johar, K., Priya, A., & Wong-Riley, M. T. T. (2014). Regulation of Na<sup>+</sup>/K<sup>+</sup>-ATPase by neuron-specific transcription factor Sp4: implication in the tight coupling of energy production, neuronal activity and energy consumption in neurons. *European Journal of Neuroscience*, *39*(4), 566–578. <https://doi.org/10.1111/ejn.12415>
- Keith Chenault, H., & Whitesides, G. M. (1989). Lactate dehydrogenase-catalyzed regeneration of NAD from NADH for use in enzyme-catalyzed synthesis. *Bioorganic Chemistry*, *17*(4), 400–409. [https://doi.org/10.1016/0045-2068\(89\)90041-2](https://doi.org/10.1016/0045-2068(89)90041-2)
- Klugmann, M., Schwab, M. H., Pühlhofer, A., Schneider, A., Zimmermann, F., Griffiths, I. R., & Nave, K.-A. A. (1997). Assembly of CNS myelin in the absence of proteolipid protein. *Neuron*, *18*(1), 59–70. [https://doi.org/10.1016/S0896-6273\(01\)80046-5](https://doi.org/10.1016/S0896-6273(01)80046-5)
- Koch, K., McLean, J., Segev, R., Freed, M. A., Berry, M. J., Balasubramanian, V., & Sterling, P. (2006). How much the eye tells the brain. *Current Biology*, *16*(14), 1428–34. <https://doi.org/10.1016/j.cub.2006.05.056>
- Kriegler, S., & Chiu, S. Y. (1993). Calcium signaling of glial cells along mammalian axons. *The Journal of Neuroscience*, *13*(10), 4229–45. Retrieved from <http://www.jneurosci.org/content/13/10/4229.abstract>
- Lange, S. C., Winkler, U., Andresen, L., Byhrø, M., Waagepetersen, H. S., Hirrlinger, J., & Bak, L. K. (2015). Dynamic Changes in Cytosolic ATP Levels in Cultured Glutamatergic Neurons During NMDA-Induced Synaptic Activity Supported by Glucose or Lactate. *Neurochemical Research*, *40*(12), 2517–26. <https://doi.org/10.1007/s11064-015-1651-9>

- Laughlin, S. B., de Ruyter van Steveninck, R. R., & Anderson, J. C. (1998). The metabolic cost of neural information. *Nature Neuroscience*, *1*(1), 36–41. <https://doi.org/10.1038/236>
- Lee, Y., Morrison, B. M., Li, Y., Lengacher, S., Farah, M. H., Hoffman, P. N., ... Rothstein, J. D. (2012). Oligodendroglia metabolically support axons and contribute to neurodegeneration. *Nature*, *487*(7408), 443–448. <https://doi.org/10.1038/nature11314>
- Lev-Ram, V., & Grinvald, A. (1987). Activity-dependent calcium transients in central nervous system myelinated axons revealed by the calcium indicator Fura-2. *Biophysical Journal*, *52*(4), 571–6. [https://doi.org/10.1016/S0006-3495\(87\)83246-0](https://doi.org/10.1016/S0006-3495(87)83246-0)
- Liberti, M. V., & Locasale, J. W. (2016). The Warburg Effect: How Does it Benefit Cancer Cells? *Trends in Biochemical Sciences*, *41*(3), 211–218. <https://doi.org/10.1016/j.tibs.2015.12.001>
- Lin, A.-L., Gao, J.-H., Duong, T. Q., & Fox, P. T. (2010). Functional neuroimaging: a physiological perspective. *Frontiers in Neuroenergetics*, *2*. <https://doi.org/10.3389/fnene.2010.00017>
- Lu, S. C. (2009). Regulation of glutathione synthesis. *Molecular Aspects of Medicine*, *30*(1–2), 42–59. <https://doi.org/10.1016/j.mam.2008.05.005>
- Maalouf, M., Rho, J. M., & Mattson, M. P. (2009). The neuroprotective properties of calorie restriction, the ketogenic diet, and ketone bodies. *Brain Research Reviews*, *59*(2), 293–315. <https://doi.org/10.1016/j.brainresrev.2008.09.002>
- Mächler, P., Wyss, M. T. T., Elsayed, M., Stobart, J., Gutierrez, R., von Faber-Castell, A., ... Weber, B. (2016). In Vivo Evidence for a Lactate Gradient from Astrocytes to Neurons. *Cell Metabolism*, *23*(1), 94–102. <https://doi.org/10.1016/j.cmet.2015.10.010>
- Magistretti, P. J. (2006). Neuron-glia metabolic coupling and plasticity. *Journal of Experimental Biology*, *209*(12), 2304–2311. <https://doi.org/10.1242/jeb.02208>
- Marvin, J. S., Borghuis, B. G., Tian, L., Cichon, J., Harnett, M. T., Akerboom, J., ... Looger, L. L. (2013). An optimized fluorescent probe for visualizing glutamate neurotransmission. *Nature Methods*, *10*(2), 162–70. <https://doi.org/10.1038/nmeth.2333>
- Marx, V. (2017). Probes: FRET sensor design and optimization. *Nature Methods*, *14*(10), 949–953. <https://doi.org/10.1038/nmeth.4434>
- Mauleon, G., Fall, C. P., & Eddington, D. T. (2012). Precise Spatial and Temporal Control of Oxygen within In Vitro Brain Slices via Microfluidic Gas Channels. *PLoS ONE*, *7*(8), e43309. <https://doi.org/10.1371/journal.pone.0043309>

- McAllister, M. S., Krizanac-Bengez, L., Macchia, F., Naftalin, R. J., Pedley, K. C., Mayberg, M. R., ... Janigro, D. (2001). Mechanisms of glucose transport at the blood-brain barrier: An in vitro study. *Brain Research*, *904*(1), 20–30. [https://doi.org/10.1016/S0006-8993\(01\)02418-0](https://doi.org/10.1016/S0006-8993(01)02418-0)
- Meister, A., & Anderson, M. E. (1983). Glutathione. *Annual Review of Biochemistry*, *52*(1), 711–760. <https://doi.org/10.1146/annurev.bi.52.070183.003431>
- Mensch, S., Baraban, M., Almeida, R., Czopka, T., Ausborn, J., El Manira, A., & Lyons, D. A. (2015). Synaptic vesicle release regulates myelin sheath number of individual oligodendrocytes in vivo. *Nature Neuroscience*, *18*(5), 628–630. <https://doi.org/10.1038/nn.3991>
- Micu, I., Plemel, J. R., Caprariello, A. V., Nave, K.-A., & Stys, P. K. (2018). Axo-myelinic neurotransmission: a novel mode of cell signalling in the central nervous system. *Nature Reviews. Neuroscience*, *19*(1), 49–58. <https://doi.org/10.1038/nrn.2017.128>
- Micu, I., Plemel, J. R., Lachance, C., Proft, J., Jansen, A. J., Cummins, K., ... Stys, P. K. (2016). The molecular physiology of the axo-myelinic synapse. *Experimental Neurology*, *276*, 41–50. <https://doi.org/10.1016/j.expneurol.2015.10.006>
- Micu, I., Ridsdale, A., Zhang, L., Woulfe, J., McClintock, J., Brantner, C. A., ... Stys, P. K. (2007). Real-time measurement of free Ca<sup>2+</sup> changes in CNS myelin by two-photon microscopy. *Nature Medicine*, *13*(7), 874–879. <https://doi.org/10.1038/nm1568>
- Mieskes, G., Kuduz, J., & Soling, H. D. (1987). Are calcium-dependent protein kinases involved in the regulation of glycolytic/gluconeogenic enzymes? Studies with Ca<sup>2+</sup>/calmodulin-dependent protein kinase and protein kinase C. *European Journal of Biochemistry*, *167*(2), 383–389.
- Millecamps, S., & Julien, J.-P. P. (2013). Axonal transport deficits and neurodegenerative diseases. *Nature Reviews Neuroscience*, *14*(3), 161–176. <https://doi.org/10.1038/nrn3380>
- Morris, M. E., & Felmler, M. A. (2008). Overview of the Proton-coupled MCT (SLC16A) Family of Transporters: Characterization, Function and Role in the Transport of the Drug of Abuse  $\gamma$ -Hydroxybutyric Acid. *The AAPS Journal*, *10*(2), 311–321. <https://doi.org/10.1208/s12248-008-9035-6>
- Mulkey, D. K., Henderson, R. A., Olson, J. E., Putnam, R. W., & Dean, J. B. (2001). Oxygen measurements in brain stem slices exposed to normobaric hyperoxia and hyperbaric oxygen. *Journal of Applied Physiology*, *90*(5), 1887–99. <https://doi.org/10.1152/jappl.2001.90.5.1887>
- Mulligan, S. J., & MacVicar, B. A. (2004). Calcium transients in astrocyte endfeet cause cerebrovascular constrictions. *Nature*, *431*(7005), 195–199. <https://doi.org/10.1038/nature02827>

- Mullis, K., Faloona, F., Scharf, S., Saiki, R., Horn, G., & Erlich, H. (1986). Specific enzymatic amplification of DNA in vitro: the polymerase chain reaction. *Cold Spring Harbor Symposia on Quantitative Biology*, *51*(1), 263–273. <https://doi.org/10.1101/SQB.1986.051.01.032>
- Nagai, T., Yamada, S., Tominaga, T., Ichikawa, M., & Miyawaki, A. (2004). Expanded dynamic range of fluorescent indicators for Ca<sup>2+</sup> by circularly permuted yellow fluorescent proteins. *Proceedings of the National Academy of Sciences of the United States of America*, *101*(29), 10554–10559. <https://doi.org/10.1073/pnas.0400417101>
- Nakano, M., Imamura, H., Nagai, T., & Noji, H. (2011). Ca<sup>2+</sup> regulation of mitochondrial ATP synthesis visualized at the single cell level. *ACS Chemical Biology*, *6*(7), 709–15. <https://doi.org/10.1021/cb100313n>
- Nave, K. (2010). Myelination and the trophic support of long axons. *Nature Reviews Neuroscience*, *11*(4), 275–283. <https://doi.org/10.1038/nrn2797>
- Nave, K.-A. (2010). Myelination and support of axonal integrity by glia. *Nature*, *468*(7321), 244–52. <https://doi.org/10.1038/nature09614>
- Newman, J. C., & Verdin, E. (2014). β-hydroxybutyrate: Much more than a metabolite. *Diabetes Research and Clinical Practice*, *106*(2), 173–181. <https://doi.org/10.1016/j.diabres.2014.08.009>
- Newman, J. C., & Verdin, E. (2017). β-Hydroxybutyrate: A Signaling Metabolite. *Annual Review of Nutrition*, *37*(1), 51–76. <https://doi.org/10.1146/annurev-nutr-071816-064916>
- Okumoto, S., Looger, L. L., Micheva, K. D., Reimer, R. J., Smith, S. J., & Frommer, W. B. (2005). Detection of glutamate release from neurons by genetically encoded surface-displayed FRET nanosensors. *Proceedings of the National Academy of Sciences of the United States of America*, *102*(24), 8740–5. <https://doi.org/10.1073/pnas.0503274102>
- Orkand, R. K., Nicholls, J. G., & Kuffler, S. W. (1966). Effect of nerve impulses on the membrane potential of glial cells in the central nervous system of amphibia. *Journal of Neurophysiology*, *29*(4), 788–806. <https://doi.org/10.1152/jn.1966.29.4.788>
- Ovens, M. J., Davies, A. J., Wilson, M. C., Murray, C. M., & Halestrap, A. P. (2010). AR-C155858 is a potent inhibitor of monocarboxylate transporters MCT1 and MCT2 that binds to an intracellular site involving transmembrane helices 7–10. *The Biochemical Journal*, *425*(3), 523–30. <https://doi.org/10.1042/BJ20091515>
- Pathak, D., Shields, L. Y., Mendelsohn, B. A., Haddad, D., Lin, W., Gerencser, A. A., ... Nakamura, K. (2015). The role of mitochondrially derived ATP in synaptic vesicle recycling. *The Journal of Biological Chemistry*, *290*(37), 22325–22336. <https://doi.org/10.1074/jbc.M115.656405>



- Pawley, J. B. (2006). *Handbook Of Biological Confocal Microscopy*. (J. B. Pawley, Ed.), Springer.  
<https://doi.org/10.1007/978-0-387-45524-2>
- Pellerin, L. (2003). Lactate as a pivotal element in neuron – glia metabolic cooperation, *43*, 331–338.  
[https://doi.org/10.1016/S0197-0186\(03\)00020-2](https://doi.org/10.1016/S0197-0186(03)00020-2)
- Pellerin, L., & Magistretti, P. J. (1994). Glutamate uptake into astrocytes stimulates aerobic glycolysis: a mechanism coupling neuronal activity to glucose utilization. *Proceedings of the National Academy of Sciences of the United States of America*, *91*(22), 10625–9. <https://doi.org/10.1073/pnas.91.22.10625>
- Pellerin, L., & Magistretti, P. J. (2012). Sweet sixteen for ANLS. *Journal of Cerebral Blood Flow and Metabolism*, *32*(7), 1152–1166. <https://doi.org/10.1038/jcbfm.2011.149>
- Pérez-Escuredo, J., Van Hée, V. F., Sboarina, M., Falces, J., Payen, V. L., Pellerin, L., & Sonveaux, P. (2016). Monocarboxylate transporters in the brain and in cancer. *Biochimica et Biophysica Acta - Molecular Cell Research*, *1863*(10), 2481–2497. <https://doi.org/10.1016/j.bbamcr.2016.03.013>
- Perge, J. A., Koch, K., Miller, R., Sterling, P., & Balasubramanian, V. (2009). How the Optic Nerve Allocates Space, Energy Capacity, and Information. *Journal of Neuroscience*, *29*(24), 7917–7928.  
<https://doi.org/10.1523/JNEUROSCI.5200-08.2009>
- Pierre, K., & Pellerin, L. (2005). Monocarboxylate transporters in the central nervous system: distribution, regulation and function. *Journal of Neurochemistry*, *94*(1), 1–14. <https://doi.org/10.1111/j.1471-4159.2005.03168.x>
- Preibisch, S., Saalfeld, S., & Tomancak, P. (2009). Globally optimal stitching of tiled 3D microscopic image acquisitions. *Bioinformatics*, *25*(11), 1463–1465. <https://doi.org/10.1093/bioinformatics/btp184>
- Prins, M. L. (2008). Cerebral metabolic adaptation and ketone metabolism after brain injury. *Journal of Cerebral Blood Flow and Metabolism*, *28*(1), 1–16. <https://doi.org/10.1038/sj.jcbfm.9600543>
- Rahman, M., Muhammad, S., Khan, M. A., Chen, H., Ridder, D. A., Müller-Fielitz, H., ... Schwaninger, M. (2014). The  $\beta$ -hydroxybutyrate receptor HCA2 activates a neuroprotective subset of macrophages. *Nature Communications*, *5*, 3944. <https://doi.org/10.1038/ncomms4944>
- Rangaraju, V., Calloway, N., & Ryan, T. A. (2014). Activity-Driven Local ATP Synthesis Is Required for Synaptic Function. *Cell*, *156*(4), 825–835. <https://doi.org/10.1016/j.cell.2013.12.042>
- Rasband, M. N., Trimmer, J. S., Peles, E., Levinson, S. R., & Shrager, P. (1999). K<sup>+</sup> channel distribution and clustering in developing and hypomyelinated axons of the optic nerve. *Journal of Neurocytology*, *28*(4–5), 319–31. <https://doi.org/10.1023/A:1007057512576>

- Reivich, M., Kuhl, D., Wolf, A., Greenberg, J., Phelps, M., Ido, T., ... Sokoloff, L. (1979). The [18F]fluorodeoxyglucose method for the measurement of local cerebral glucose utilization in man. *Circulation Research*, *44*(1), 127–137. <https://doi.org/10.1161/01.RES.44.1.127>
- Rich, P. R. (2003). The molecular machinery of Keilin's respiratory chain. *Biochemical Society Transactions*, *31*(Pt 6), 1095–1105. <https://doi.org/10.1042/BST0311095>
- Rinholm, J. E., Hamilton, N. B., Kessaris, N., Richardson, W. D., Bergersen, L. H., & Attwell, D. (2011). Regulation of oligodendrocyte development and myelination by glucose and lactate. *The Journal of Neuroscience*, *31*(2), 538–48. <https://doi.org/10.1523/JNEUROSCI.3516-10.2011>
- Rueda, C. B., Llorente-Folch, I., Amigo, I., Contreras, L., González-Sánchez, P., Martínez-Valero, P., ... Satrustegui, J. (2014). Ca(2+) regulation of mitochondrial function in neurons. *Biochimica et Biophysica Acta*, *1837*(10), 1617–24. <https://doi.org/10.1016/j.bbabi.2014.04.010>
- Saab, A. S., Tzvetanova, I. D., Trevisiol, A., Baltan, S., Dibaj, P., Kusch, K., ... Nave, K.-A. (2016). Oligodendroglial NMDA Receptors Regulate Glucose Import and Axonal Energy Metabolism. *Neuron*, *91*(1), 119–132. <https://doi.org/10.1016/j.neuron.2016.05.016>
- San Martín, A., Ceballo, S., Baeza-Lehnert, F., Lerchundi, R., Valdebenito, R., Contreras-Baeza, Y., ... Barros, L. F. (2014). Imaging Mitochondrial Flux in Single Cells with a FRET Sensor for Pyruvate. *PLoS ONE*, *9*(1), e85780. <https://doi.org/10.1371/journal.pone.0085780>
- Schirmeier, S., Matzat, T., & Klambt, C. (2016). Axon ensheathment and metabolic supply by glial cells in *Drosophila*. *Brain Research*, *1641*(Pt A), 122–129. <https://doi.org/10.1016/j.brainres.2015.09.003>
- Schmidt, M. M., & Dringen, R. (2009). Differential effects of iodoacetamide and iodoacetate on glycolysis and glutathione metabolism of cultured astrocytes. *Frontiers in Neuroenergetics*, *1*(March), 1. <https://doi.org/10.3389/neuro.14.001.2009>
- Sinha, K., Karimi-Abdolrezaee, S., Velumian, A. A., & Fehlings, M. G. (2006). Functional changes in genetically dysmyelinated spinal cord axons of shiverer mice: role of juxtaparanodal Kv1 family K<sup>+</sup> channels. *Journal of Neurophysiology*, *95*(3), 1683–1695. <https://doi.org/10.1152/jn.00899.2005>
- Sokoloff, L., Reivich, M., Kennedy, C., Rosiers, M. H. Des, Patlak, C. S., Pettigrew, K. D., ... Shinohara, M. (1977). The [14 C]Deoxyglucose Method for the Measurement of Local Cerebral Glucose Utilization: Theory, Procedure, and Normal Values in the Conscious and Anesthetized Albino Rat. *Journal of Neurochemistry*, *28*(5), 897–916. <https://doi.org/10.1111/j.1471-4159.1977.tb10649.x>
- Stevens, B., & Fields, R. D. (2000). Response of Schwann cells to action potentials in development. *Science*, *287*(5461), 2267–71. <https://doi.org/10.1126/science.287.5461.2267>

- Stiefel, K. M., Torben-Nielsen, B., & Coggan, J. S. (2013). Proposed evolutionary changes in the role of myelin. *Frontiers in Neuroscience*, 7, 202. <https://doi.org/10.3389/fnins.2013.00202>
- Stobart, J. L., & Anderson, C. M. (2013). Multifunctional role of astrocytes as gatekeepers of neuronal energy supply. *Frontiers in Cellular Neuroscience*, 7. <https://doi.org/10.3389/fncel.2013.00038>
- Stryer, L. (1995). *Stryer Biochemistry. Biochemistry textbook*. Retrieved from <http://books.google.com/books?id=jQKGAAAACAAJ>
- Stys, P. K. (2011). The axo-myelinic synapse. *Trends in Neurosciences*, 34(8), 393–400. <https://doi.org/10.1016/j.tins.2011.06.004>
- Stys, P. K., Ransom, B. R., & Waxman, S. G. (1991). Compound action potential of nerve recorded by suction electrode: a theoretical and experimental analysis. *Brain Research*, 546(1), 18–32. [https://doi.org/10.1016/0006-8993\(91\)91154-S](https://doi.org/10.1016/0006-8993(91)91154-S)
- Surin, A. M., Gorbacheva, L. R., Savinkova, I. G., Sharipov, R. R., Khodorov, B. I., & Pinelis, V. G. (2014). Study on ATP concentration changes in cytosol of individual cultured neurons during glutamate-induced deregulation of calcium homeostasis. *Biochemistry. Biokhimiia*, 79(2), 146–57. <https://doi.org/10.1134/S0006297914020084>
- Swanson, R. A. (2004). Astrocyte Neurotransmitter Uptake. In *Neuroglia* (2nd ed., pp. 346–354). New York: Oxford University Press. <https://doi.org/10.1093/acprof:oso/9780195152227.003.0027>
- Tanda, N., Hinokio, Y., Washio, J., Takahashi, N., & Koseki, T. (2014). Analysis of ketone bodies in exhaled breath and blood of ten healthy Japanese at OGTT using a portable gas chromatograph. *Journal of Breath Research*, 8(4), 46008. <https://doi.org/10.1088/1752-7155/8/4/046008>
- Tantama, M., Martínez-François, J. R., Mongeon, R., Yellen, G., Tantama, M., Ramo, J., ... Yellen, G. (2013). Imaging energy status in live cells with a fluorescent biosensor of the intracellular ATP-to-ADP ratio. *Nature Communications*, 4(May), 2550. <https://doi.org/10.1038/ncomms3550>
- Tarrade, A., Fassier, C., Courageot, S., Charvin, D., Vitte, J., Peris, L., ... Melki, J. (2006). A mutation of spastin is responsible for swellings and impairment of transport in a region of axon characterized by changes in microtubule composition. *Human Molecular Genetics*, 15(24), 3544–3558. <https://doi.org/10.1093/hmg/ddl431>
- Tekkök, S. B., Brown, A. M., Westenbroek, R., Pellerin, L., & Ransom, B. R. (2005). Transfer of glycogen-derived lactate from astrocytes to axons via specific monocarboxylate transporters supports mouse optic nerve activity. *Journal of Neuroscience Research*, 81(5), 644–652. <https://doi.org/10.1002/jnr.20573>

- Thomson, C. E., Hunter, A. M., Griffiths, I. R., Edgar, J. M., & McCulloch, M. C. (2006). Murine spinal cord explants: a model for evaluating axonal growth and myelination in vitro. *Journal of Neuroscience Research*, *84*(8), 1703–15. <https://doi.org/10.1002/jnr.21084>
- Thomson, C. E., McCulloch, M., Sorenson, A., Barnett, S. C., Seed, B. V., Griffiths, I. R., & McLaughlin, M. (2008). Myelinated, synapsing cultures of murine spinal cord - validation as an in vitro model of the central nervous system. *European Journal of Neuroscience*, *28*(8), 1518–1535. <https://doi.org/10.1111/j.1460-9568.2008.06415.x>
- Toloe, J., Mollajew, R., Kügler, S., & Mironov, S. L. (2014). Metabolic differences in hippocampal “Rett” neurons revealed by ATP imaging. *Molecular and Cellular Neuroscience*, *59*, 47–56. <https://doi.org/10.1016/j.mcn.2013.12.008>
- Trevisiol, A., Saab, A. S., Winkler, U., Marx, G., Imamura, H., Möbius, W., ... Hirrlinger, J. (2017). Monitoring ATP dynamics in electrically active white matter tracts. *eLife*, *6*. <https://doi.org/10.7554/eLife.24241>
- Turko, I. V., Marcondes, S., & Murad, F. (2001). Diabetes-associated nitration of tyrosine and inactivation of succinyl-CoA:3-oxoacid CoA-transferase. *American Journal of Physiology-Heart and Circulatory Physiology*, *281*(6), H2289–H2294. <https://doi.org/10.1152/ajpheart.2001.281.6.H2289>
- Volkenhoff, A., Weiler, A., Letzel, M., Stehling, M., Klambt, C., & Schirmeier, S. (2015). Glial Glycolysis Is Essential for Neuronal Survival in *Drosophila*. *Cell Metabolism*, *22*(3), 437–447. <https://doi.org/10.1016/j.cmet.2015.07.006>
- Warburg, O. (1925). The Metabolism of Carcinoma Cells. *The Journal of Cancer Research*, *9*(1), 148–163. <https://doi.org/10.1158/jcr.1925.148>
- Waxman, S. G. (1977). Conduction in Myelinated, Unmyelinated, and Demyelinated Fibers. *Archives of Neurology*, *34*(10), 585–589. <https://doi.org/10.1001/archneur.1977.00500220019003>
- Werner, H. B., Kuhlmann, K., Shen, S., Uecker, M., Schardt, A., Dimova, K., ... Nave, K.-A. (2007). Proteolipid Protein Is Required for Transport of Sirtuin 2 into CNS Myelin. *Journal of Neuroscience*, *27*(29), 7717–7730. <https://doi.org/10.1523/JNEUROSCI.1254-07.2007>
- Zhang, C.-L., Wilson, J. A., Williams, J., & Chiu, S. Y. (2006). Action Potentials Induce Uniform Calcium Influx in Mammalian Myelinated Optic Nerves. *Journal of Neurophysiology*, *96*(2), 695–709. <https://doi.org/10.1152/jn.00083.2006>
- Zhang, Y., & Barres, B. A. (2010). Astrocyte heterogeneity: an underappreciated topic in neurobiology. *Current Opinion in Neurobiology*, *20*(5), 588–594. <https://doi.org/10.1016/j.conb.2010.06.005>

Zhao, Y., Jin, J., Hu, Q., Zhou, H.-M., Yi, J., Yu, Z., ... Loscalzo, J. (2011). Genetically Encoded Fluorescent Sensors for Intracellular NADH Detection. *Cell Metabolism*, *14*(4), 555–566. <https://doi.org/10.1016/j.cmet.2011.09.004>



## Appendices

### 7.1 Appendix §1 – MATLAB script for CAP processing and analysis

The script processes .mat files generated in Patchmatster as exported waveforms-timeseries (from .dat raw data)

```

clear all; clc
[FileName,PathName] = uigetfile('*.mat','Select the MATLAB code file');
S = load(fullfile(PathName,FileName));
prompt={'Enter value for signal amplification used: '};
name = 'Amplification';
defaultans = {'200'};
amplif = inputdlg(prompt,name,[1 40],defaultans);
Mag = sprintf('%s*', amplif{:});
Mag = sscanf(Mag, '%f*');
fig1=figure('Name','CAP waveforms',...
'Color', [0.99 0.99 0.99],...
'Position', [380 180 1280 720],...
'Units', 'pixels');
for f = fieldnames(S)
i = S.(f{1});
u = horzcat((i(:,1)-i(1,1))*1.00e+3,i(:,2).*(1000/Mag));
plot(u(:,1),u(:,2));
hold on;
end
title('CAP');
xlabel('time [ms]');
ylabel('\muV');
datacursormode on;
dcm_obj = datacursormode(gcf);
set(dcm_obj,'Enable','on');
disp('select range for offset with TWO datatips on the waveform, then press ENTER')
pause;
c_info = getCursorInfo(dcm_obj);
if length(c_info) == 2
offset =
sort(vercat(c_info(1).Position(1,1),c_info(2).Position(1,1)),'ascend');
off1 = offset(1,1);
off2 = offset(1,2);
else disp('WARNING!! not enough/too many datatips inserted: will assign default
values 0.1 and 0.9 for offset');
off1 = 0.1;
off2 = 0.9;
pause
end
datacursormode off;
hold off
for f = fieldnames(S)
i = S.(f{1});
u = horzcat((i(:,1)-i(1,1))*1.00e+3,i(:,2).*(1000/Mag));
r = horzcat(u(:,1),u(:,2)-mean(u(min(find(u(:,1)>
off1&u(:,1)<off2)):max(find(u(:,1)>off1&u(:,1)<off2)),2)));
r(:,2) = sgolayfilt(r(:,2),4,23);
plot(r(:,1),r(:,2));
hold on;
end
datacursormode on;
dcm_obj = datacursormode(gcf);
set(dcm_obj,'Enable','on');
disp('select range for CAP Area Analysis, then press ENTER')
pause;
c_info2 = getCursorInfo(dcm_obj);

```

```

range = sort(vertcat(c_info2(1).Position(1,1),c_info2(2).Position(1,1)), 'ascend');
left = range(1,1);
right = range(1,2);
if c_info2(1).Position(1,1)>c_info2(2).Position(1,1);
    xcap = c_info2(1).Target.XData;
    ycap = c_info2(1).Target.YData;
else
    xcap = c_info2(2).Target.XData;
    ycap = c_info2(2).Target.YData;
end
hold on
xauc = [xcap(xcap>=left&xcap<right); xcap(xcap>=left&xcap<right);
xcap(xcap>left&xcap<=right); xcap(xcap>left&xcap<=right)];
yauc = [zeros(1,length(xauc)); ycap(xcap>=left&xcap<right); ycap(xcap>left&xcap<=right);
zeros(1,length(xauc))];
p = patch(xauc,yauc,[.99 .2 .7], 'FaceAlpha', '.2', 'EdgeColor', 'none');
title('CAP');
xlabel('time [ms]');
ylabel('\muV');
f = fieldnames(S)';
t0 = S.(char(f(1,1)))(1,1);
h = 1;
for f = fieldnames(S) '
    i = S.(f{1});
    x1=(i(:,1)-i(1,1)).*1000;
    cap_time(h)=(i(1,1)-t0)/60;
    y1=i(:,2).*(1000/Mag);
    R.(f{1}) = horzcat(x1,y1);
    cap_range=x1(x1>=left&x1<=right);
    cap_area(h)=trapezoid(cap_range,y1(x1>=left&x1<=right));
    h = h+1;
end
dcm_obj = datacursormode(gcf);
set(dcm_obj, 'Enable', 'on');
disp('select range for CAP amplitude-latency Analysis, then press ENTER')
pause;
c_info3 = getCursorInfo(dcm_obj);
range0 = sort(vertcat(c_info3(1).Position(1,1),c_info3(2).Position(1,1)), 'ascend');
left0 = range0(1,1);
right0 = range0(1,2);
if c_info3(1).Position(1,1)>c_info3(2).Position(1,1);
    xcap0 = c_info3(1).Target.XData;
    ycap0 = c_info3(1).Target.YData;
else
    xcap0 = c_info3(2).Target.XData;
    ycap0 = c_info3(2).Target.YData;
end
h = 1;
for f = fieldnames(R) '
    i = R.(f{1});
    x2=i(:,1);
    y2=i(:,2);
    cap_range=x2(x2>=left0&x2<=right0);
    cap_amplitude(h)=max(y2(x2>=left0&x2<=right0));
    cap_latency(h)=mean(x2(y2==max(y2(x2>=left0&x2<=right0))));
    h = h+1;
end
xauc0 = [xcap0(xcap0>=left0&xcap0<right0); xcap0(xcap0>=left0&xcap0<right0);
xcap0(xcap0>left0&xcap0<=right0); xcap0(xcap0>left0&xcap0<=right0)];
yauc0 = [zeros(1,length(xauc0)); ycap0(xcap0>=left0&xcap0<right0);
ycap0(xcap0>left0&xcap0<=right0); zeros(1,length(xauc0))];
p0 = patch(xauc0,yauc0,[.1 1 .3], 'FaceAlpha', '.2', 'EdgeColor', 'none');
cap_time = cap_time';
cap_area = cap_area';
cap_amplitude = cap_amplitude';
cap_latency = cap_latency';

fig2=figure('Name', 'CAP Area', ...
'Color', [0.99 0.99 0.99], ...
'Position', [100 100 1280 720], ...

```



```

    'Units', 'pixels');
hold on
sz =100;
scatter(cap_time,cap_area,sz,'filled','p',...
    'LineWidth',.1,...
    'MarkerEdgeColor',[1 0 0],...
    'MarkerFaceColor',[.9 .3 .3]);
sz =50;
scatter(cap_time,cap_amplitude,sz,'filled','o',...
    'LineWidth',.05,...
    'MarkerEdgeColor',[0 1 1],...
    'MarkerFaceColor',[.3 .9 .9]);
sz =50;
scatter(cap_time,cap_latency,sz,'filled','s',...
    'LineWidth',.05,...
    'MarkerEdgeColor',[1 0 1],...
    'MarkerFaceColor',[.9 .3 .9]);
dot_operator = char(8901);
legend('CAP Area','CAP Amplitude','CAP Latency','Location','best')
title('CAP Analysis');
xlabel('time [min]');
ylabel(strcat('\muV',dot_operator,'ms ',' - ',' \muV ',' - ',' ms'));
file = strcat(PathName, strtok(FileName, '.'), '.xlsx');
strange = strcat(num2str(range(1,1)), '_ms_', num2str(range(1,2)), '_ms');
strange0 = strcat(num2str(range0(1,1)), '_ms_', num2str(range0(1,2)), '_ms');
head =
{'time_zero',strcat('cap_area_',strange),strcat('cap_amplitude_',strange0),strcat('cap_la
tency_',strange0)};
T = table(cap_time,cap_area,cap_amplitude,cap_latency);
writetable(T,file,'Sheet',1);
xlswrite(file,head,1,'A1:D1');

```

## 7.2 Appendix §2 – ImageJ Macro for FRET ATP analysis on ROI basis

The script processes FRET data as .lsm hyperstacks (three channels, timeseries). ROIs are generated around large structures (large axons for ThyAT) and small structures (complementary-ROIs, small axons for ThyAT)

```

function convert2NaN(filename) {
    h = getHeight();
    w = getWidth();
    for (n=1; n<=nSlices; n++) {
        setSlice(n);
        for (y = 0; y < h; y++){
            for ( x = 0; x < w; x++){
                p = getPixel(x,y);
                if (p == 0.0){ setPixel(x,y,NaN); }
            }
        }
    }
};
run("Set Measurements...", "mean redirect=None decimal=3");
path = File.openDialog("Select a File");
open(path);
setLocation(1110, 10);
dir = File.getParent(path)+"//";
fileName = File.getName(path);
title = File.nameWithoutExtension;
run("Split Channels");
Dialog.create("Substack range");
setLocation(900,10);
Dialog.addNumber("start:", 1);

```

```

Dialog.addNumber("end:", 650);
Dialog.show();
img_start = Dialog.getNumber();
img_end = Dialog.getNumber();
substack = "slices="+img_start+"-"+img_end;

selectWindow("C1-"+fileName);
run("Make Substack...", substack);
rename("FRET_"+"("+substack+)");
subdir1= dir + "/" + title + "_FRET//";
File.makeDirectory(subdir1);
run("Image Sequence... ", "format=TIFF save=["+subdir1+]");
close("C1-"+fileName);
run("Remove Outliers...", "radius=2 threshold=0 which=Bright stack");
run("Remove Outliers...", "radius=2 threshold=0 which=Dark stack");
selectWindow("C2-"+fileName);
run("Make Substack...", substack);
rename("CFP_"+"("+substack+)");
subdir2= dir + "/" + title + "_CFP//";
File.makeDirectory(subdir2);
run("Image Sequence... ", "format=TIFF save=["+subdir2+]");
close("C2-"+fileName);
run("Remove Outliers...", "radius=2 threshold=0 which=Bright stack");
run("Remove Outliers...", "radius=2 threshold=0 which=Dark stack");
selectWindow("C3-"+fileName);
run("Make Substack...", substack);
rename("YFP_"+"("+substack+)");
subdir3= dir + "/" + title + "_YFP//";
File.makeDirectory(subdir3);
run("Image Sequence... ", "format=TIFF save=["+subdir3+]");
close("C3-"+fileName);
run("Remove Outliers...", "radius=2 threshold=0 which=Bright stack");
run("Remove Outliers...", "radius=2 threshold=0 which=Dark stack");
imageCalculator("Multiply create 32-bit stack",
"FRET_"+"("+substack+)", "CFP_"+"("+substack+)");
imageCalculator("Multiply create 32-bit stack", "Result of
FRET_"+"("+substack+)", "YFP_"+"("+substack+)");
close("Result of FRET_"+"("+substack+)");
close("FRET_"+"("+substack+)");
close("YFP_"+"("+substack+)");
close("CFP_"+"("+substack+)");
rename("stack4align_"+"("+substack+)");
run("16-bit");
run("Enhance Contrast", "saturated=1.90");
run("Remove Outliers...", "radius=2 threshold=100 which=Bright stack");
run("Remove Outliers...", "radius=2 threshold=1 which=Dark stack");
run("Smooth", "stack");
run("Despeckle", "stack");
run("Gaussian Blur...", "sigma=2 stack");
run("Remove Outliers...", "radius=5 threshold=1 which=Bright stack");
run("Remove Outliers...", "radius=5 threshold=1 which=Bright stack");
setMinAndMax(0, 1200);
subdir4= dir + "/" + title + "_stack4align//";
File.makeDirectory(subdir4);
run("Image Sequence... ", "format=TIFF save=["+subdir4+]");
close("stack4align_"+"("+substack+)");
subdir5= dir + "/" + title + "_stackAligned//";
File.makeDirectory(subdir5);
subdir6= dir + "/" + title + "_Align_transform//";
File.makeDirectory(subdir6);
run("Register Virtual Stack Slices", "source=["+subdir4+]
output=["+subdir5+"] feature=Rigid registration=[Translation -- no deformation
] advanced shrinkage save initial_gaussian_blur=1.60 steps_per_scale_octave=4
minimum_image_size=32 maximum_image_size=256 feature_descriptor_size=8
feature_descriptor_orientation_bins=8 closest/next_closest_ratio=0.92
maximal_alignment_error=16 inlier_ratio=0.05 feature_extraction_model=Rigid
registration model=[Translation -- no deformation
]
interpolate");
close(getTitle());
run("Image Sequence...", "open=["+subdir5+] sort");

```

```

run("Convert to Mask", "method=IsoData background=Dark calculate black");
rename("8bit_large_fibers");
run("Z Project...", "projection=[Max Intensity]");
    rename("Particles_ROIs");
        run("Analyze Particles...", "size=10-Infinity add");
        roiManager("Select All");
        roiManager("Combine");
        run("Make Inverse");
        roiManager("Add");
        selectWindow("Particles_ROIs");
        run("Select All");
        roiManager("Add");
    close();
selectWindow("8bit_large_fibers");
run("Divide...", "value=255 stack");
    rename("MASK_large_fibers");
    MASK_large_fibers = getTitle()
run("Duplicate...", "duplicate");
run("Multiply...", "value=255 stack");
run("Convert to Mask", "method=Default background=Light calculate black");
run("Divide...", "value=255 stack");
    rename("MASK_small_fibers");
    MASK_small_fibers = getTitle()
subdir7= dir + "/" + title + "_FRET_aligned//";
File.makeDirectory(subdir7);
subdir8= dir + "/" + title + "_CFP_aligned//";
File.makeDirectory(subdir8);
subdir9= dir + "/" + title + "_YFP_aligned//";
File.makeDirectory(subdir9);
run("Transform Virtual Stack Slices", "source=["+subdir1+"] output=["+subdir7+"]
transforms=["+subdir6+"]");
    close(getTitle());
    run("Image Sequence...", "open=["+subdir7+"] sort");
        FRET_align_stack = getTitle();
        imageCalculator("Multiply create 32-bit stack",
FRET_align_stack, MASK_large_fibers);
            convert2NaN(getTitle);
            rename("FRET_large_fibers");
            nROIs = roiManager("count");
            for (n=0;n<nROIs;n++){
                roiManager("Select", n);
                roiManager("Rename",
"FRET_ROI_" + (n+1));
            }
            roiManager("Select", nROIs-2);
            roiManager("Rename", "FRET_remain_ROIs");
            roiManager("Select", nROIs-1);
            roiManager("Rename",
"FRET_All_large_fibers");
            roiManager("Select All");
            roiManager("Multi Measure");
            filename0 = subdir7 + "FRET_large_fibers";
            saveAs("Tiff", filename0);
            roiManager("Show All with labels");
            roiManager("Select All");
            roiManager("Associate", "false");
            roiManager("Centered", "false");
            roiManager("UseNames", "true");
            run("Flatten", "slice");
            filename0ROI = subdir7 + "FRET_ROIs";
            saveAs("Tiff", filename0ROI);
            close();
            close("FRET_large_fibers.tif");
            roiManager("Select All");
            roiManager("Save", filename0ROI+".zip");
            imageCalculator("Multiply create 32-bit stack",
FRET_align_stack, MASK_small_fibers);
                convert2NaN(getTitle);
                rename("FRET_small_fibers");
                roiManager("Select", nROIs-1);

```

```

roiManager("Rename", "FRET_All_small_fibers");
roiManager("multi-measure      measure_all      one
append");

filename1 = subdir7 + "FRET_small_fibers"
saveAs("Tiff", filename1);
close();
close(FRET_align_stack);
run("Transform Virtual Stack Slices", "source=["+subdir2+"] output=["+subdir8+"]
transforms=["+subdir6+"]");
close(getTitle());
run("Image Sequence...", "open=["+subdir8+"] sort");
CFP_align_stack = getTitle()
imageCalculator("Multiply      create      32-bit      stack",
CFP_align_stack, MASK_large_fibers);
convert2NaN(getTitle);
rename("CFP_large_fibers");
for (n=0;n<nROIs;n++){
roiManager("Select", n);
roiManager("Rename",
"CFP_ROI_"+(n+1));
}
roiManager("Select", nROIs-2);
roiManager("Rename", "CFP_remain_ROIs");
roiManager("Select", nROIs-1);
roiManager("Rename",
"CFP_All_large_fibers");
roiManager("Select All");
roiManager("multi-measure measure_all one
append");

filename2 = subdir8 + "CFP_large_fibers";
saveAs("Tiff", filename2);
roiManager("Show All with labels");
roiManager("Select All");
roiManager("Associate", "false");
roiManager("Centered", "false");
roiManager("UseNames", "true");
run("Flatten", "slice");
filename2ROI = subdir8 + "CFP_ROIs";
saveAs("Tiff", filename2ROI);
close();
close("CFP_large_fibers.tif");
roiManager("Select All");
roiManager("Save", filename2ROI+".zip");
imageCalculator("Multiply      create      32-bit      stack",
CFP_align_stack, MASK_small_fibers);
convert2NaN(getTitle);
rename("CFP_small_fibers");
roiManager("Select", nROIs-1);
roiManager("Rename", "CFP_All_small_fibers");
roiManager("multi-measure      measure_all      one
append");

filename3 = subdir8 + "CFP_small_fibers"
saveAs("Tiff", filename3);
close();
close(CFP_align_stack);
run("Transform Virtual Stack Slices", "source=["+subdir3+"] output=["+subdir9+"]
transforms=["+subdir6+"]");
close(getTitle());
run("Image Sequence...", "open=["+subdir9+"] sort");
YFP_align_stack = getTitle()
imageCalculator("Multiply      create      32-bit      stack",
YFP_align_stack, MASK_large_fibers);
convert2NaN(getTitle);
rename("YFP_large_fibers");
for (n=0;n<nROIs;n++){
roiManager("Select", n);
roiManager("Rename",
"YFP_ROI_"+(n+1));
}
roiManager("Select", nROIs-2);

```

```

roiManager("Rename", "YFP_remain_ROIs");
roiManager("Select", nROIs-1);
roiManager("Rename",
"YFP_All_large_fibers");
roiManager("Select All");
roiManager("multi-measure measure_all one
append");
filename4 = subdir9 + "YFP_large_fibers";
saveAs("Tiff", filename4);
roiManager("Show All with labels");
roiManager("Select All");
roiManager("Associate", "false");
roiManager("Centered", "false");
roiManager("UseNames", "true");
run("Flatten", "slice");
filename4ROI = subdir9 + "YFP_ROIs";
saveAs("Tiff", filename4ROI);
close();
close("YFP_large_fibers.tif");
roiManager("Select All");
roiManager("Save", filename4ROI+".zip");
imageCalculator("Multiply create 32-bit stack",
YFP_align_stack, MASK_small_fibers);
convert2NaN(getTitle);
rename("YFP_small_fibers");
roiManager("Select", nROIs-1);
roiManager("Rename", "YFP_All_small_fibers");
roiManager("multi-measure measure_all one
append");
filename5 = subdir9 + "YFP_small_fibers"
saveAs("Tiff", filename5);
close();
close(YFP_align_stack);
results = dir + title + "_FRET-CFP-YFP_Mean_Intensities.txt//";
saveAs("Results", "["+results+"]");
close(MASK_large_fibers);
close(MASK_small_fibers);
selectWindow("ROI Manager");
run("Close");
selectWindow("Results");
run("Close");

```

### 7.3 Appendix §3 – ImageJ macro for initial processing of FLIM data

The script processes FLIM data as .tif stacks separated by timepoint.

```

function mask_FLIM(input, output1, output2, filename) {
run("Bio-Formats Windowless Importer", "open=["+input+"//"+filename+"]");
run("Duplicate...", "duplicate");
duplicateImg = getTitle();
run("Convert to Mask", "method=Otsu background=Dark calculate black");
run("Z Project...", "projection=[Max Intensity]");
run("Despeckle");
run("Remove Outliers...", "radius=1 threshold=0 which=Bright");
run("Remove Outliers...", "radius=2 threshold=0 which=Dark");
//....!
run("Divide...", "value=255");
run("Save", "save=["+output1+filename+"]");
mask = getTitle();
imageCalculator("Multiply create 32-bit stack", duplicateImg, mask);
run("Save", "save=["+output2+filename+"]");
run("Close All");
};
function convert2NaN(input, output, filename) {

```

```

run("Bio-Formats Windowless Importer", "open=["+input+"//"+filename+""]);
h = getHeight();
w = getWidth();
for (n=1; n<=nSlices; n++) {
    setSlice(n);
    for (y = 0; y < h; y++){
        for ( x = 0; x < w; x++){
            p = getPixel(x,y);
            if (p == 0.0){ setPixel(x,y,NaN); }
        }
    }
}
run("Save", "save=["+output+filename+""]);
run("Close");
};
path = File.openDialog("Select a File");
setLocation(1110, 10)
dir = File.getParent(path);
fileName = File.getName(path);
title = File.nameWithoutExtension;
list = getFileList(dir);
    subdir1= dir + "/" + title + "_Mask//";
    subdir2= dir + "/" + title + "_Results//";
    File.makeDirectory(subdir1);
    File.makeDirectory(subdir2);
for (k = 0; k < list.length; k++) {
    mask_FLIM(dir, subdir1, subdir2, list[k]);
}

```

#### 7.4 Appendix §4 – MATLAB script for FLIM analysis on ROI basis

The script requires 1) system IRF, 2) a .csv file generated in ImageJ, containing the x-y coordinates of the ROI, 3) FLIM data as .tif stacks separated by timepoint.

```

clear all; close all
workdir = pwd;
[name1,PathData] = uigetfile({'*.tif','tif-image'},'select reference FLIM stack and
folder...');
[name2,PathIRF] = uigetfile({'*.tif','tif-image'},'Select IRF stack and folder...');
[name3,PathROI] = uigetfile({'*.csv','ROI'},'select ROI csv file generated in FIJI');
filename = strsplit(name1, '.');
t_res = 0.25;
h = waitbar(0,'starting analysis...','Name','FLIM Analysis progress','Position',[20 30
270 50],'Unit','pixels','Color','c');
filePattern = fullfile(PathData, '\*.');
ImageFiles = dir(filePattern);
ListOfImageNames = {};
    for Index = 1:length(ImageFiles)
        baseFileName = ImageFiles(Index).name;
        [folder, name, extension] = fileparts(baseFileName);
        extension = upper(extension);
        switch lower(extension)
            case {'*.tif'}
                ListOfImageNames = [ListOfImageNames baseFileName];
        end
    end
im_info = imfinfo([PathData name1]);
im_w = im_info(1).Width;
im_h = im_info(1).Height;
im_num = numel(im_info);
filePattern2 = fullfile(PathROI, '\*.');
AllFiles = dir(filePattern2);
ListOfROINames = {};

```

```

ROI_names = {};
for Index = 1:length(AllFiles).
    baseFileName = AllFiles(Index).name;
    [folder, name, extension] = fileparts(baseFileName);
    extension = upper(extension);
    switch lower(extension)
        case {''.csv'}
            ListOfROINames = [ListOfROINames baseFileName];
            ROI_names = [ROI_names name];
    end
end

cd(PathROI);
Mask_3D = zeros(im_w,im_h,length(ListOfROINames),'uint16');
for iii = 1:length(ListOfROINames)
    nameROI=char(ListOfROINames(iii));
    ROIxy = csvread(nameROI,1,1);
    ROIx = ROIxy(:,2)+1;
    ROIy = ROIxy(:,1)+1;
    Mask = zeros(im_w, im_h, 1,'uint16');
    indexes = sub2ind([im_w, im_h], ROIx, ROIy);
    Mask(indexes) = 1;
    Mask_3D(:,:,iii) = Mask;
    figure('Name',ROI_names{iii},'NumberTitle','off');
    imagesc(Mask_3D(:,:,iii))
end

for i = 1:length(ROI_names)
    Amplitude_ext.(ROI_names{i}) = [];
    Tau_ext.(ROI_names{i}) = [];
    Tau_weight.(ROI_names{i}) = [];
    Tau_mean_weight.(ROI_names{i}) = [];
end

im_info = imfinfo([PathIRF name2]);
im_w = im_info(1).Width;
im_h = im_info(1).Height;
im_num = numel(im_info);

IRF = zeros(im_w, im_h, im_num,'uint16');
for l = 1:im_num
    IRF(:,:,l)=imread([PathIRF name2],'Index',l);
end
IRF = squeeze(sum(sum(IRF)));
nbin = numel(IRF);
IRF = reshape(IRF,nbin,numel(IRF)/nbin);
IRF = mean(IRF,2);
T = 1e9/84e6;
dt = T/nbin;
tau = ((1:nbin)-0.5).*dt;
figure_2 = figure;
counts_residuals = figure;
semilogy(tau,IRF,':b')

for ii=1:length(ListOfImageNames)
    name1=char(ListOfImageNames(ii));
    perc = round(ii/size(ListOfImageNames,2),2)*100;
    waitbar(perc/100,h,sprintf('%d%% completed...',perc))
    if strcmp(name2,name1)==0

        FLIMData = zeros(im_w, im_h, im_num,'uint16');
        for l = 1:im_num
            FLIMData(:,:,l)=imread([PathData name1],'Index',l);
        end

        for ri = 1:size(Mask_3D,3)
            Mask_roi = Mask_3D(:,:,ri);
            for mi = 1:size(FLIMData,3)
                Data{ri}(:,:,mi) = FLIMData(:,:,mi).*Mask_roi;
            end
        end
    end
end

```

```

Data = squeeze(sum(sum(Data{ri})));
nbin = numel(Data);
T = 1e9/84e6;
dt = T/nbin;
tau = ((1:nbin)-0.5).*dt;

figure(figure_2);
hold on
semilogy(tau,Data,'x')

tau = [0.1 1];
tau = tau(:)'/dt;
m = numel(tau);
lim = [zeros(1,m) 10.*ones(1,m)];
lim_min = lim(1:m)./dt;
lim_max = lim(m+1:end)./dt;
p = nbin;
tp = (1:p)';
y = Data(:);
t = 1:numel(y);
c = 0;
x = exp(-(tp-1)*(1./tau))*diag(1./(1-exp(-p./tau)));
irs = IRF(rem(rem(t-floor(c)-1, p)+p,p)+1);
z = Convol(irs, x);
z = [ones(size(z,1),1) z];
A = lsqnonneg(z,y);
% close all
param = [c; tau'];
paramin = [-1/dt lim_min];
paramax = [ 1/dt lim_max];

tmp = param;
err = 0;
for casc=1:10
    [ts, s] = min(err);
    r0 = tmp(:, s);
    for sub=1:10
        rf = r0.*[(2.^(1.2*(rand(3,1)-0.5)./casc))];
        tmp(:,sub) = Simplex('lsfit', param, paramin, paramax, [], [], IRF(:),
y(:, p);
        c = tmp(1,sub);
        tau = tmp(2:m,sub)';
        x = exp(-(tp-1)*(1./tau))*diag(1./(1-exp(-p./tau)));
        irs = (1-c+floor(c))*IRF(rem(rem(t-floor(c)-1, p)+p,p)+1) + (c-
floor(c))*IRF(rem(rem(t-ceil(c)-1, p)+p,p)+1);
        z = Convol(irs, x);
        z = [ones(size(z,1),1) z];
        z = z./(ones(nbin,1)*sum(z));
        A = lsqnonneg(z,y);
        z = z*A;
        err(sub) = sum((y-z).^2./abs(z))/(nbin-m);
    end
end

param = mean(tmp(:,err==min(err)),2);

[param, dparam] = Simplex('lsfit', param, paramin, paramax, [], [], IRF(:), y(:),
p);

c = param(1);
dc = dparam(1);
tau = param(2:length(param))';
dtau = dparam(2:length(param));

x = exp(-(tp-1)*(1./tau))*diag(1./(1-exp(-p./tau)));
irs = (1-c+floor(c))*IRF(rem(rem(t-floor(c)-1, p)+p,p)+1) + (c-
floor(c))*IRF(rem(rem(t-ceil(c)-1, p)+p,p)+1);
z = Convol(irs, x);
z = [ones(size(z,1),1) z];

```



```

z = z./(ones(nbin,1)*sum(z));
A = lsqnonneg(z,y);
zz = z.*(ones(size(z,1),1)*A');
z = z*A;
dc = dt*dc;

chi = sum((y-z).^2./abs(z))/(nbin-m);

t = dt*t;
tau = dt*tau';
c = dt*c;
offset = zz(1,1);
A(1) = [];

figure(counts_residuals);
hold on
subplot('position',[0.1 0.35 0.8 0.55])
plot(t,log10(y),'+k')
plot(t,log10(irs),':b');
plot(t,log10(z));
v = axis;
v(1) = min(t);
v(2) = max(t);
axis(v);
xlabel('Time / ns');
ylabel('Log Count');
s = sprintf('COF = %3.3f %3.3f', c, offset);
text(max(t)/2,v(4)-0.05*(v(4)-v(3)),s);
s = ['Amp = '];
for i=1:length(A)
    s = [s sprintf('%1.3f',A(i)/sum(A)) ' '];
end
text(max(t)/2,v(4)-0.12*(v(4)-v(3)),s);
s = ['tau = '];
for i=1:length(tau)
    s = [s sprintf('%3.3f ns',tau(i)) ' '];
end
text(max(t)/2,v(4)-0.19*(v(4)-v(3)),s);
subplot('position',[0.1 0.1 0.8 0.15])
plot(t,(y-z));
v = axis;
v(1) = min(t);
v(2) = max(t);

axis(v);
xlabel('time / ns');
ylabel('residuals');
s = sprintf('%3.3f', chi);
text(max(t)/2,v(4)-0.1*(v(4)-v(3)),['\chi^2 = ' s]);
set(gcf,'units','normalized','position',[0.01 0.05 0.98 0.83])
clear Data;

Amplitude = A./sum(A);

Amplitude_ext.(ROI_names{ri}) = [Amplitude_ext.(ROI_names{ri}) Amplitude];
Tau_ext.(ROI_names{ri}) = [Tau_ext.(ROI_names{ri}) tau];

end
else
    disp('IRF image not taken')
end
end

time = [0:t_res:(length(ListOfImageNames)-1)*t_res]';

for ji = 1:length(ROI_names)
    Tau_weight.(ROI_names{ji}) = [Tau_weight.(ROI_names{ji})
Amplitude_ext.(ROI_names{ji})*Tau_ext.(ROI_names{ji})];
    Tau_mean_weight.(ROI_names{ji}) = [Tau_mean_weight.(ROI_names{ji})
sum((Tau_weight.(ROI_names{ji}).^2))./sum((Tau_weight.(ROI_names{ji})))];

```

```

end

Tau_AWLT = [];
for ji = 1:length(ROI_names);
    Tau_AWLT = [Tau_AWLT (Tau_mean_weight.(ROI_names{ji}))'];
end

figure_2 = figure('Name','Lifetime','NumberTitle','off','Color',[0.99 0.99 0.99],...
    'Position',[100 100 1280 720],...
    'Units','pixels');
plot(time,Tau_AWLT)
title(strrep(filename{1},'_','\_'))
xlabel('time min'); ylabel('Lifetime nsec')
legend(ROI_names); legend('Location','best'); legend('boxoff');
set(gca,'fontsize',12)

Tau_AWLT = vertcat(ROI_names,num2cell(Tau_AWLT));
filenameTau_AW = strcat(workdir,'\',filename{1},'_Tau_AW.xlsx');
xlswrite(filenameTau_AW,Tau_AWLT,1,'B1');
xlswrite(filenameTau_AW,time,1,'A2');
cd(workdir);

{ Function lsfit

function err = lsfit(param, irf, y, p)

n = length(irf);
t = 1:n;
tp = (1:p)';
c = param(1);
tau = param(2:length(param)); tau = tau(:)';
x = exp(-(tp-1)*(1./tau))*diag(1./(1-exp(-p./tau)));
irs = (1-c+floor(c))*irf(rem(rem(t-floor(c)-1, n)+n,n)+1) + (c-floor(c))*irf(rem(rem(t-
ceil(c)-1, n)+n,n)+1);
z = Convolve(irs, x);
z = [ones(size(z,1),1) z];
A = lsqnonneg(z,y);
z = z*A;

err = sum((z-y).^2./z)./(n-length(tau));
}

{ Function Simplex

function [x, dx, steps] = Simplex(fname, x, xmin, xmax, tol, steps, varargin)
x = x(:);
if nargin<5
    tol = 1e-10;
if nargin<4
    xmax = Inf*ones(length(x),1);
    if nargin<3
        xmin = -Inf*ones(length(x),1);
    end
end
elseif isempty(tol)
    tol = 1e-5;
end
if nargin<6
    steps = [];
end
if isempty(xmin)
    xmin = -Inf*ones(size(x));
end
if isempty(xmax)
    xmax = Inf*ones(size(x));
end
xmin = xmin(:);
xmax = xmax(:);
xmax(xmax<xmin) = xmin(xmax<xmin);

```

```

x(x<xmin) = xmin(x<xmin);
x(x>xmax) = xmax(x>xmax);
xfix = zeros(size(x));
tmp = xmin==xmax;
xfix(tmp) = xmin(tmp);
mask = diag(~tmp);
mask(:, tmp) = [];
x(tmp) = [];
xmin(tmp) = [];
xmax(tmp) = [];

if isa(fname, 'function_handle')
    fun = fname;
    evalstr = 'fun';
else
    evalstr = fname;
end
evalstr = [evalstr, '(mask*x+xfix)'];
if nargin>6
    evalstr = [evalstr, ', varargin{:}'];
end
evalstr = [evalstr, ')'];

n = length(x);
if n==0
    x = xfix;
    dx = zeros(size(xfix));
    steps = 0;
    return
end
if isempty(steps)
    steps = 200*n;
end

xin = x(:);
%v = 0.9*xin;
v = xin;
v(v<xmin) = xmin(v<xmin);
v(v>xmax) = xmax(v>xmax);
x(:) = v; fv = eval(evalstr);
for j = 1:n
    y = xin;
    if y(j) ~= 0
        y(j) = (1 +.2*rand)*y(j);
    else
        y(j) = 0.2;
    end
    if y(j)>=xmax(j)
        y(j) = xmax(j);
    end
    if y(j)<=xmin(j)
        y(j) = xmin(j);
    end
    v = [v y];
    x(:) = y; f = eval(evalstr);
    fv = [fv f];
end
[fv, j] = sort(fv);
v = v(:,j);
count = n+1;

% Parameter settings for Nelder-Meade
alpha = 1; beta = 1/2; gamma = 2;

% Begin of Nelder-Meade simplex algorithm
while count < steps
    if 2*abs(fv(n+1)-fv(1))/(abs(fv(1))+abs(fv(n+1))) <= tol
        break
    end
end

```

```

% Reflection:
vmean = mean(v(:, 1:n),2);
vr = (1 + alpha)*vmean - alpha*v(:, n+1);
x(:) = vr;
fr = eval(evalstr);
count = count + 1;
vk = vr; fk = fr;

if fr < fv(1) && all(xmin<=vr) && all(vr<=xmax)
    % Expansion:
    ve = gamma*vr + (1-gamma)*vmean;
    x(:) = ve;
    fe = eval(evalstr);
    count = count + 1;
    if fe < fv(1) && all(xmin<=ve) && all(ve<=xmax)
        vk = ve; fk = fe;
    end
else
    vtmp = v(:,n+1); ftmp = fv(n+1);
    if fr < ftmp && all(xmin<=vr) && all(vr<=xmax)
        vtmp = vr; ftmp = fr;
    end
    % Contraction:
    vc = beta*vtmp + (1-beta)*vmean;
    x(:) = vc;
    fc = eval(evalstr);
    count = count + 1;
    if fc < fv(n) && all(xmin<=vc) && all(vc<=xmax)
        vk = vc; fk = fc;
    else
        % Shrinkage:
        for j = 2:n
            v(:, j) = (v(:, 1) + v(:, j))/2;
            x(:) = v(:, j);
            fv(j) = eval(evalstr);
        end
        count = count + n-1;
        vk = (v(:, 1) + v(:, n+1))/2;
        x(:) = vk;
        fk = eval(evalstr);
        count = count + 1;
    end
end
v(:, n+1) = vk;
fv(n+1) = fk;
[fv, j] = sort(fv);
v = v(:,j);
end

x = v(:,1);
dx = abs(v(:,n+1)-v(:,1));
x = mask*x + xfix;
dx = mask*dx;
if count>=steps
    disp(['Warning: Maximum number of iterations (' , int2str(steps), ') has been
exceeded']);
else
    steps = count;
end
}

```

# Curriculum Vitae

## Personal profile

First name, Last name:	Andrea, Trevisiol
Date of birth:	27 October 1985
Place of birth:	Treviso, Italy
Nationality:	Italian
Email:	Trevisiol@em.mpg.de

## Education

January 2014 – Present	Ph.D. Student in Molecular Physiology of the Brain (GGNB program) at Max-Planck-Institute for Experimental Medicine in Göttingen, Germany. Project: " <i>Metabolism of oligodendrocytes and its involvement in axo-glia interaction</i> ".
January 2013 – December 2013	Internship at the Neurogenetics department of the Max-Planck-Institute for Experimental Medicine in Göttingen, Germany. Project: " <i>Establishing genetically encoded metabolic sensors and FRET imaging</i> ".
December 2010 – December 2012	International Master Degree in Neuroscience at University of Trieste, Italy. Grade 108/110, experimental thesis developed at Max-Planck-Institute for Experimental Medicine in Göttingen, Germany. Project: " <i>Genetic sensors for metabolites: new approaches toward studying glial cell metabolism</i> ".
October 2006 – December 2010	Bachelor Degree in Evolutionary Biology at University of Padova, Italy. Grade 90/110, Project: " <i>Glucocorticoid receptor knockdown and craniofacial cartilage development in Zebrafish: preliminary analysis by in situ hybridization</i> ".

## Awards and funding

May 2016 Young Glia - YG Platinum Award - 2FY full support collaboration grant

January - October 2012 European Erasmus Scholarship for International Student Exchange Program

## Conferences

1 December 2017 4<sup>th</sup> biennial Encephalon Symposium "The Art of Generation and Degeneration".  
Poster.

26-28 October 2017 Zons, Germany: SPP 1757, Annual meeting of the Priority Programme on Glial heterogeneity. Poster & scientific talk.

12-16 November 2016 Society for Neuroscience meeting, San Diego. Poster.

9-11 October 2016 Berlin, Germany: SPP 1757, Annual meeting of the Priority Programme on Glial heterogeneity. Poster.

25-28 May 2016 12<sup>th</sup> ICBEM, Hong Kong. Poster & "Student blitz" presentation.

8-10 October 2015 Homburg, Germany: SPP 1757, Annual meeting of the Priority Programme on Glial heterogeneity. Poster.

## Workshops and international activities

3-9 September 2017 EMBO course "Two-photon imaging of brain dynamics: Illuminating neuronal and glial function" in Zurich (Switzerland), hosted by Fritjof Helmchen and Bruno Weber.

28 February 2017 Personalized training with Dr. Hidetoshi Tozaki-Saitoh on "in vivo spinal cord  
- imaging" at Kyushu University, Fukuoka (Japan). Workshop funded by the Young  
3 March 2017 Glia award.

3-12 December 2013 IBRO College "Dynamic Imaging in Neuroscience" at CECs in Valdivia (Chile) hosted by Felipe Barros

## Publications

**Trevisiol A.**, Saab A. S., Winkler U., Marx G., Imamura H., Möbius W., Kusch K., Nave K. A., Hirrlinger J. (2017) *Monitoring ATP dynamics in electrically active white matter tracts*. *Elife*. 6. pii: e24241. doi: 10.7554/eLife.24241.

Saab A. S., Tzvetanova I., **Trevisiol A.**, Baltan S., Dibaj P., Kusch K., Möbius W., Goetze B., Jahn H. M., Huang W., Steffens H., Schomburg E. D., Pérez-Samartín A., Pérez-Cerdá F., Bakhtiari D., Matute C., Löwel S., Griesinger C., Hirrlinger J., Kirchhoff F., Nave K. A. (2016) *Oligodendroglial NMDA Receptors Regulate Glucose Import and Axonal Energy Metabolism*. *Neuron*. 6;91(1):119-32. doi: 10.1016/j.neuron.2016.05.016.

**Trevisiol A.**, Nave K. A. (2015) *Brain Energy Metabolism: Conserved Functions of Glycolytic Glial Cells*. *Cell Metab*. 1;22(3):361-3. doi: 10.1016/j.cmet.2015.08.010.